Spring 1988

Integral Equation Solution of the Full Potential Equation for Three-Dimensional, Steady, Transonic Wing Flows

Li-Chuan Chu
Old Dominion University

INTEGRAL EQUATION SOLUTION OF THE FULL POTENTIAL EQUATION FOR THREE-DIMENSIONAL, STEADY, TRANSONIC WING FLOWS

by

Li-Chuan Chu

M. E. in Mechanical Engineering, December 1980
Old Dominion University
Norfolk, Virginia

A Dissertation Submitted to the Faculty of
Old Dominion University in Partial Fulfillment of
the Requirement for the Degree of

DOCTOR OF PHILOSOPHY
MECHANICAL ENGINEERING
OLD DOMINION UNIVERSITY

May 1988

Approved by:

_____

E. C. Yates. Jr.

R. L. Ash

O. Baysal

J. H. Heinbockel

ABSTRACT

Integral Equation Solution of the Full Potential Equation for Three-Dimensional, Steady, Transonic Wing Flows

Li-Chuan Chu
Old Dominion University, 1988
Director: Dr. Osama A. Kandil

An integral equation method for solving the full potential equation has been developed for three-dimensional transonic vortex-wing flows. This method is capable of capturing shocks using the Murman-Cole type of finite difference scheme and is capable of predicting accurate and force-free wake shape as well.

Reading the full potential equation as Poisson's equation, the solution for the velocity field has been expressed in terms of an integral equation using Green's theorem. The solution consists of a surface integral of vorticity distribution on the wing and its free-vortex sheets and a volume integral of source distribution within a computational region around the flow domain under consideration. The solution is obtained through two iteration loops: the outer loop iterates the vorticity distribution and wake shape, while the inner loop iterates the field compressibility.

A computer program has been constructed for implementation of this methodology and has been used to solve a flow around a rectangular flat wing with a trailing wake. The program can be modified without difficulties to solve flow problems with complex configurations. The wing and its free-vortex sheets are modeled using a bilinear vortex panel distribution, while the field compressibility of the flow domain

under consideration is modeled using a constant, distributed, source strength over each of the discretized rectangular-parallelopiped volume cells.

The technique of pre-calculated and stored induced velocity for field compressibility calculations has greatly reduced the computational time. The successive grid refinement has also effectively and reliably reduced the computational domain and greatly improved the accuracy as well.

The numerical results show that this method is computationally stable and efficient and also show its great potential in solving unsteady transonic flow problems.

The study conducted in this dissertation also sheds some light in the vectorization of an integral equation method which is crucial in achieving better computational efficiency when running on a modern vector computer.

ACKNOWLEDGEMENTS

The author wishes to express his appreciation to his advisor Professor Osama A. Kandil for his guidance, advice and continuous encouragement during the development of this work.

The author wishes also to express his gratitude to Dr. E. Carson Yates, Jr., of NASA Langley Research Center, for his invaluable advice and constant encouragement while conducting this research.

Thanks are due to Professor R. L. Ash, Chairman of the Mechanical Engineering and Mechanics Department, for his encouragement, and to Drs. O. Baysal and J. H. Heinbockel for reviewing the thesis.

The author is also indebted to Charles V. Spain of PRC Kentron Corp. for his administrative assistance.

The work is supported by NASA Langley Research Center under Grant No. NAG-1-591 and Contract No. NAS1-18000, Dr. E. Carson Yates, Jr. is the technical monitor.

TABLE OF CONTENTS

LIST OF TABLES

LIST OF FIGURES

LIST OF SYMBOLS

A	panel area
$\vec{A}$	vector potential, Eq. (3.1)
AR	Wing Aspect Ratio
a	speed of sound
a_i, b_i, c_i	coefficients of the shape function N_i
C_p	pressure coefficient
ΔC_p	net pressure coefficient
DPM	Doublet Panel Method
$d\xi x, d\xi y, d\xi z$	direction cosines of the local ξ axis
$d\eta x, d\eta y, d\eta z$	direction cosines of the local η axis
$d\varsigma x, d\varsigma y, d\varsigma z$	direction cosines of the local ς axis
$\vec{e}_\infty$	unit vector parallel to the free stream
$\vec{e}_\xi, \vec{e}_\eta, \vec{e}_\varsigma$	unit vectors of the local coordinate system
G	compressibility volume, Eq. (4.4)
HVM	Hybrid Vortex Method
$\vec{I}, \vec{J}, \vec{K}$	unit vectors of the global coordinate system
i, j	indices of a global node
$\vec{i}, \vec{j}, \vec{k}$	same as $\vec{e}_\xi, \vec{e}_\eta, \vec{e}_\varsigma$
ℓ	length of side $1-3$ of free vortex panel
LE	Leading Edge
N_i	shape functions
NDV	Non-linear Discrete Vortex Method

$NVLM$	Non-linear Vortex Lattice Methods
$\vec{n}$	unit normal vector
P_i	influence coefficient of the ξ component of velocity
Q_i	symbol used in Eq. (3.28)
q	source strength, Eq. (4.8)
R_i	influence coefficient of the η component of velocity
S_i	influence coefficient of the η component of velocity
S	function describing the wing surface
SE	Side Edge
TE	Trailing Edge
$V(ni, nj)$	velocity induced by the njth vortex panel at the nith control point
VLM	Vortex Lattice Methods
VPM	Vortex Panel Methods
W	function describing the wake surface
$\bar{x}, \bar{y}, \bar{z}$	local coordinates of the centroid of vortex panel
x, y, z	global coordinates of a field point

Greek letter

α	angle of attack
β	angle of the velocity vector with the z-axis in the plane of the wing
ξ, ς, η	local coordinates of a vortex point
ρ	density
μ	doublet strength, Eq. (4.8)
Ω	vorticity volume, Eq. (3.17)

Φ	total velocity potential
ϕ	perturbation velocity potential
$\nabla\phi$	perturbation velocity
$\omega_x(i,j), \omega_y(i,j),$ $\omega_z(i,j)$	global components of vorticity at global node (i,j)
$\omega_\xi(k), \omega_\zeta(k)$	local components of vorticity at local node k
$\omega_x(k), \omega_y(k),$ $\omega_z(k)$	global components of vorticity at local node k

Subscripts

ind	induced
ℓ	lower surface
r	field point
rot	rotational field
s	wing surface
u	upper surface
w	wake
∞	free stream

Superscripts

$*$	dimensional quantity, Eqs. (4.1)-(4.3)

Chapter 1

INTRODUCTION

1.1. Why CFD?

In the designs of aircraft, missiles and helicopters, the wind tunnel along with limited theoretical methods have long been used as a basic design tool for simulating the aerodynamic environment. The limitations to the wind tunnel which are known to many aerodynamists, e.g. Bradley and Bhateley [1], include expensive costs, overcrowded facilities, long lead time for iterations, questions of full-scale extrapolations, limited flow field data and tunnel blockage and interference, etc. The aerodynamic designers have long called for efficient and effective design tools to supplement the wind tunnel tests due to these limitations especially the expensive costs and the long turn-around time.

The fast development of the high-speed digital computer has had a great impact on the way in which principles from the engineering science are applied to problems of design in modern engineering practice. Problems can now be solved at very little cost in a few seconds of computer time which would have taken years to work out with the computational methods and computers available twenty years ago. The ready availability of previously unimaginable computing power has stimulated many changes. One of the important changes which we have been witnessing is the development of a new methodology for attacking the complex problems in

fluid mechanics and heat transfer. This new methodology has become known as computational fluid dynamics; the CFD.

In recent years, CFD has been providing a great deal of help in the aerodynamic designs due to its abilities in solving certain complex aerodynamic problems at a reasonable cost and in a comparably short turn-around time and hence has become an important and necessary design tool in supplement to the expensive and time-consuming wind tunnel tests.

1.2. CFD for Fighter Aircraft Design

Despite its fast development in the past decade, CFD still currently faces some limitations and difficulties in the aerodynamic designs of fighter aircraft. Bradley and Bhateley [1] listed such limitations and difficulties as computer codes to model complex real-fluid flows, hardware capability to model real geometries, computational speed for use in real design, mesh generation for complex configurations, and low management confidence in computed results. They also reviewed the status of existing computational methods with emphasis on fighter design applications and their ratings ranged from poor to fair. This is why management confidence in computed results, which probably is the most influential to the acceptance of CFD in fighter aircraft designs, is still low.

Moreover, during the maneuvering, many combat aircraft experienced the critical situations at which the real aerodynamic loads are much higher than the design loads. All these caused a status which urgently calls for improvements and development of CFD for fighter aircraft applications.

1.3. Problems in Aerodynamic Designs

The development of computational techniques for three-dimensional flows past wings at high angles of attack have become extremely important to aerodynamicists dealing with modern designs of fighter aircraft, missiles, and helicopters. Modern fighter aircraft fly at high angles of attack during takeoff, offensive and defensive maneuvering, approach, and landing. In this range of angle of attack, vortex flows develop around the aircraft that have dominant effects on its aerodynamic characteristics and controllability. Modern designs of missiles require high launch angles of attack and high maneuverability within which a very complex vortex flow develops. For helicopters, the interaction of a blade with the vortex wake of another blade affects its operating performance, vibration, and noise characteristics. In forward speeds, blade slap, a predominant source of external noise, occurs due to the rapid time rates of change of the pressure on the blade developing from the blade passage through a tip vortex of a preceding blade.

For all these applications, one has to deal with strong nonlinear aerodynamics. Compressibility and edge separation of the flow are the main sources of the strong nonlinear effects. Prediction of the aerodynamic characteristics under the coupled effects of nonlinearities is obviously a challenging problem because of the complexities involved in the flow.

An extensive literature review reveals that all of the existing techniques do not simultaneously and completely account for these two sources of nonlinearities. Some of the existing techniques can treat the problem of flow separation at sharp edges without accounting for the full nonlinear compressibility effects (limited to low Mach numbers), while the others can treat the problem of full nonlinear compressibility

without accounting for the roll-up of the separated flow (limited to small angles of attack).

Mathematically, a problem is called a nonlinear problem if the governing equation is nonlinear and/or if the boundary conditions are nonlinear. For inviscid, incompressible, or low-subsonic flows at high angles of attack, the problem is nonlinear, although the governing equation is linear (the Laplace or Prandtl-Glauert equation). The nonlinearity is due to the boundary conditions on the separated flow surfaces. On the other hand, for inviscid compressible flows at low angles of attack, the problem is nonlinear because the governing equation is nonlinear (full potential equation) even with linearized boundary conditions. For compressible flows at high angles of attack, the problem is obviously nonlinear due to both the governing equation and the boundary conditions.

1.4. Motivation of This Work

In search for an appropriate numerical method of solution, one has to bear in mind the origin of the nonlinearity; a boundary oriented (separated flow roll-up), a region oriented (flow compressibility), or both. For the boundary-oriented nonlinearity, methods that are directly or indirectly derived from the Green's function solution (integral equation methods) have been developed, such as the nonlinear discrete vortex, doublet panel, vortex panel, and velocity potential panel, among others. To account for the flow compressibility in these methods, the Prandtl-Glauert transformation based on the freestream Mach number is used. The computed results have shown that this transformation is limited to cases with low subsonic Mach numbers and high angles of attack or moderate-to-high subsonic Mach numbers and

low angles of attack. For the region-oriented nonlinearity, finite difference methods have been extensively used.

Kandil and Yates [2] developed a computational scheme which is based on the integral solution of the full potential equation for a steady, three-dimensional, transonic flow. Their results appeared to be satisfactory when compared with other computational results and experimental data, Fig. 1.

The present research is using the same methodology with modifications in both vorticity field calculations (using first order vortex panel instead of zeroth order vortex lattice) and field compressibility calculations (using pre-calculated velocity coefficients instead of direct calculations). The former modification improves the accuracy and stability in the near-field calculations while the latter improves the computational efficiency greatly.

The purpose of this research is to develop a computational technique which is based on the integral equation solution to accurately and efficiently predict the aerodynamic characteristics in a three-dimensional transonic vortex flow. Those aerodynamic characteristics include the shock locations, pressure distributions, and force-free wake shapes. The motivation behind this work is to apply the developed technique to modern aircraft designs which include canard wing, wing-tail and wing-body configurations in the transonic regime.

An extensive review of the literature is presented in Chapter 2. Chapter 3 details the problem formulation including the global vortex panel method for incompressible flow. The formulation of the field compressibility along with its computational scheme is given in Chapter 4. Chapter 5 presents numerical results for both incompressible and compressible flow applications. The concluding remarks and recommendations for future work are presented in Chapter 6.

Chapter 2

HISTORICAL REVIEW AND LITERATURE STUDY

2.1. Description of the Flow Field

Experimental investigations [3-10] have shown that flow field around highly swept, sharp-edged wings over a wide-range of angles of attack is characterized by the thin wakes that separated from wing edges and behave like vortex sheets that roll up in the vicinity of the separation edges and form two helix-like cones of vortex cores above the upper surface of the wing. This type of flow separation is known as the "primary separation." It is mainly responsible for the well-known nonlinear aerodynamic characteristics exhibited over the angle-of-attack range due to the large strength of its vortex core and its proximity to the upper surface of the wing, Fig. 2a.

The primary vortex consists of three distinct regions [11]: an outer convection dominated region in which the distance between turns is large compared to the characteristic diffusion length; a middle region where the distance between turns is of the same order as the characteristic diffusion length; an inner diffusion dominated viscous core.

A "secondary separation" occurs because the adverse pressure gradient outboard of the suction peaks causes the boundary-layer flow on the upper surface to

separate. The secondary free-shear layers roll up spirally in an opposite sense to that of the primary separation, and form secondary vortex cores[3,7-9].

A "tertiary separation" may occur between the secondary and primary separations due to the adverse pressure gradient created by the secondary vortex core.

For highly swept wings and beyond the trailing edge, the free shear layer emanating from the trailing edge rolls up spirally in an opposite sense to that of the primary separated flow. Thus, the trailing edge vortex core has the same sense of vorticity strength and core rotation as those of the secondary vortex core, although they originate from different phenomena [9,12].

As it moves downstream, the vortex core is fed constantly with vorticity from the vortex sheet. This increasing core vorticity causes the increase of winding speed of the core and of the viscous dissipation as well. When the viscous dissipation is large enough, the cross-sectional area and the turbulence level of the core will increase abruptly. Such a phenomenon is called "vortex breakdown." The stall phenomenon of low-aspect-ratio highly swept wings is attributed to the breakdown of the primary vortex cores [13-16]. Location of the breakdown points depends upon the angle of attack and the wing aspect ratio, Fig. 2b. As the angle of attack increases, the breakdown point moves forward toward the wing trailing edge, and the slope of the lift curve decreases until a critical angle is reached at which the breakdown point crosses the trailing edge and the lift coefficient drops. The studies of the primary vortex indicate that its shape and strength are relatively independent of Reynolds number [3,17]. The relative lack of viscosity dependence suggests that the flow may be regarded as potential, with the free shear layer represented by a free-vortex sheet.

For thin slender wings at moderate incidences the influence of the Mach number on the characteristic features of the flow is small as long as $M_\infty cos\Lambda$, the Mach number normal to the leading edge, is less than 0.7 [21].

At high Mach numbers, high incidences or large thickness ratio, non-linear compressibility effects can become dominant. This results in a wealth of possible flow patterns involving primary and secondary vortex cores, (cross-flow and normal) shocks on the surface as well as in the flow field and associated regions with shock-induced distributed vorticity and entropy change, and all possible mutual interactions, sometimes resulting in an abrupt vortex breakdown. Some of these flow patterns, Fig. 2c, are discussed by Stanbrook & Squire [18], Szodruch & Ganzer [19], Vorropoulos & Wendt [20], Miller & Wood [21]. It is recognized that vortex flow with non-linear compressibility effects is of increasing importance at transonic maneuvering and supersonic speeds.

The vortex flow above strake-wing configurations is more complex. A detailed review and description of this type of flow can be found in Reference [22].

2.2. Inviscid Model Approximations

For most flows of importance in aerodynamics, the wakes are thin, in the sense that their thickness reduces as Reynolds number increases. The effects of viscosity can then be modelled by the theory of thin shear layers, provided there is an appropriate model for the interaction between the external flow and the thin shear layers. A thin shear layer affects the external flow in two ways: through a displacement effect caused by the thickness of the shear layer; and through an

induced effect caused by the difference in tangential velocity between its opposite surfaces. As the Reynolds number tends to infinity, the displacement effect dies away, but the vortex effect remains. The shear layers become vortex sheets in the limit. This leads to an inviscid model of the flow, which is governed by the Euler equations. This model is valid representation of the physical problem as long as shear layers are thin. However, in general, the formulation of the problem for the Euler equations must include a specification of the lines on the body from which the vortex sheets arise, the separation lines. It should be noted that though Euler equations do not assume isentropic flow and can capture vortical regions in addition to capturing shocks, they are computationally expensive and have implementation problem due to spurious spatial and numerical diffusion.

A symmetrical wing at zero incidence sheds no vortex wake, so it is not necessary to specify a separation line. When the wing is placed at incidence the assumption that separation takes place from the sharp trailing-edge is automatically made. In reality, as the angle of incidence increases, separation also takes place from the tip at a rate depending on the design of the tip. For a wing with a moderate- to highly-swept leading-edge of small radius, a similar separation takes place from the leading edge.

For shock-free flows past bodies immersed in a uniform stream, the inviscid flow can be represented by a potential function, and the same representation can be extended to model flows with weak shock waves. Outside the body and the vortex sheets the potential function can be used to describe the flow.

With the above description of the flow field approximations, we can summarize the following assumptions under which many potential flow models have been constructed to represent the main features of the real flow to a high degree of accuracy:

For an isolated wing, the far-field effect of deformation of the trailing-edge vortex sheet can often be neglected. However, this effect must be taken into account for the problems of aerodynamic interaction, e.g., for canard-wing, wing-tail or strake-wing configuration.

Relative to the primary vortex core, the effect of the secondary vortex cores is small in symmetric flows particularly when the boundary layer on the upper surface is turbulent (most of the real cases are). Hence, its effect on surface pressures and integrated forces can be neglected without appreciable error under the condition stated. The effect of tertiary vortex cores is even smaller and is also neglected.

In the absence of strong shocks the flow may be modelled as a potential flow with embedded free vortex sheets. Moreover, if the local Mach numbers are not close to one, the model can further be simplified to a linear potential flow, governed by the Prandtl-Glauert equation. The flow problem, including the position of the vortex sheets, can be solved by a panel method. This panel method is non-linear because the boundary conditions are nonlinear and the potential flow problem is thus nonlinear. The vortex sheets are "fitted" explicitly into the solution, rather than "captured" implicitly as part of the solution as in the Navier-Stokes and Euler methods. This requires that the presence of vortex sheets be specified a priori and that the topology of the flow be well-defined. In return the computer requirements of potential flow methods are relatively modest. In finite-difference or finite-volume methods for solving the full non-linear potential equation the treatment of free vortex sheets, floating in a fixed spatial grid, poses considerable problems.

In the potential flow formulation a vortex core consists of a tightly wound spiraling vortex sheet of semi-infinite extent. In order to simulate the flow field outside the core the sheet is necessarily cut at some angular extent, while the

cut-off part is modelled by an isolated line-vortex core which is connected to the remainder of the sheet by a so-called feeding sheet, Fig. 3. The latter transfers vorticity from the spiraling sheet into the vortex core allowing it to increase in strength as it travels downstream.

We also assume that vortex-breakdown points are far downstream so that the primary core size and its variation in the vicinity of the wing are neglected. In fact, this assumption limits the large angles of attack at which the inviscid model is applicable.

Finally, the shocks in the flow problem we try to solve must be weak, (generally, the local Mach number is less than 1.3) so that the accuracy of the solution is still acceptable under the isentropic flow assumption.

2.3. Existing Mathematical Inviscid Models

The literature contains several steady and unsteady inviscid-flow models with varying of limitations and drawbacks. These models can be divided into the following groups:

2.3.1. Leading-Edge Suction Analogy

The most widely used method for predicting the characteristics of configurations employing vortex flow is the so-called "leading-edge suction analogy," conceived by Polhamus [23-25]. In general classical lifting surface theory [26], the velocity goes to infinity at all edges except the trailing edges, resulting in a finite

suction force at leading and side-edges. This force acts normal to the edge and lies in the plane of the wing, partly counteracting the drag force. The magnitude of the suction force depends on the amplitude of the singularity in the loading at the edge. On a three-dimensional wing the normal force, found from integration of the net pressure distribution, combines with the suction force to yield the correct lift, side force and induced drag of the wing. When the flow separates at the edge, then the suction force in the chord plane is lost, but if the flow reattaches, then this potential flow leading-edge (LE) suction force becomes reoriented, now acting normal to the chord plane due to the local vortex action. A rigorous proof for this analogy does not exist, but prediction of overall forces and moments is excellent. With a vortex-lattice method as attached-flow solver, Lamar and his co-workers [27] have developed the method towards a very useful engineering tool, both for analysis and design of quite general configurations, including strake-wing configurations.

The major drawback of methods that use the suction analogy is that the pressure and velocity distribution cannot be predicted and that new situations, e.g. the encounter of a canard vortex with a wing, strake-wing vortex flow, vortex breakdown, etc. require the development of new empirical concepts.

2.3.2. Vortex-Fitting Methods

2.3.2.1. Slender-Body Theory and Conical Flow Assumption

When body dimensions normal to the free stream are much smaller than those in the free stream direction, three dimensional potential flow theory simplifies to slender body theory [26]. The disturbance potential is then a sum of two functions: one satisfying the two dimensional Laplace's equation in the plane normal to the

body centerline, the other a function of the coordinate along the body centerline. Since the latter part does not contribute to any lift forces acting on the body, the problem is one of seeking a disturbance potential satisfying the Laplace's equation in the cross flow planes.

A further simplification is the assumption of conical flow. The flow properties are assumed to be constant along straight lines passing from the nose of the body. With this assumption for the flow field scaling downstream and a solution of the vortex shape and strength at any longitudinal location, solutions at other locations are readily available.

Legendre [28] was one of the first investigators to model the separated flow over delta wings. In his model a pair of line vortices were placed above the wing and assuming conical flow, Laplace's equation was solved in the cross flow planes. However, as Adams [29] discussed, this solution concerning the lift and pressure distribution is not unique. Edwards [30] proved that for conical slender wings, a reasonable mathematical model must also consider the mechanism of the feeding vortex sheet emanating from the wing LE. Brown and Michael [31,32] rectified this deficiency by requiring the forces on the planar feeding sheet be balanced by equal, but opposite forces on the concentrated vortex, thus rendering the vortex system force free.

Later Mangler & Smith [33] and Smith [34] improved this model by including a vortex sheet of finite extent, discretized by piecewise continuous elements (panels). This greatly improved the treatment of the flow near the leading edge. For slender wings, the computed pressure distributions compare quite satisfactorily with experimental data at most of the cross flow planes with the exception of those near the trailing edge where the conical flow assumption breaks down.

Clark [35] has extended Smith's conical flow method to non-conical planforms. It was found that for non-planar wings complicated vortex sheet geometries may occur, possibly involving multiple centers of roll-up.

An excellent survey of slender-body theory and its combination with discrete vortices or vortex panel methods is given in Reference [22].

2.3.2.2. Non-linear Vortex Lattice Methods

Vortex lattice methods [36-50] are used to solve for the "aerodynamic loading of lifting planes by concentrating the equivalent vortex sheet, including the wake, into a number of elements of line vorticity arranged in a lattice," [36]. Generally the lifting surface is discretized into a number of panels arranged in the streamwise direction. For example, in Fig. 5, the bound vorticity in each quadrilateral vortex panel is lumped into a horse-shoe vortex with the bound part located at the 1/4 chord line of the quadrilateral panel. The wake or the free-vortex sheet is replaced by segmented free-vortex lines (in the case of steady flows) or by a growing free-vortex lattice (in the case of unsteady flows). With the position of the free line vortices specified a priori, the unknown circulations of the bound vortices are determined by using an iterative technique to enforce the flow tangency condition at the midpoint of the 3/4 chord line of each panel [39-41]. Excellent agreement was found between calculated and experimental total aerodynamic characteristics, and satisfactory agreement was found between calculated and experimental section characteristics for the wings with only side-edge separation.

When vortex-type separation from leading edges and/or tips occurs, the free-vortex system lies close to the lifting-surface bound vortices and results are found to be sensitive to variations in the shapes of the rectangular vortex elements and

the length of the vortex segments. Using the rectangular vortex array to model highly swept wing is not suitable, particularly in the vicinity of leading edge where the vorticity distribution is highly variant [175].

The best agreement was obtained by using the vortex arrangement developed in Reference [39]. Two conditions must be satisfied in this vortex arrangement: first, the quadrilateral elements should be uniform and second, slender vortex elements must be avoided. In addition, the vortex segments representing the free vortex sheets in the vicinity of the wing must be maintained smaller or at least of comparable lengths to the bound-vortex segments. These restrictions not only limit the generality of this model but also require substantial computational time to achieve the acceptable accuracy. The most apparent cause behind these less than satisfactory results is the approximation of continuous vortex sheets by discrete vortex lines in the near field [46].

In general, the drawbacks of the non-linear vortex lattice NDV-method are due to the approximation of a vortex sheet by a system of concentrated vortex lines, particularly in the near field. With this approximation, Biot-Savart's law becomes nearly singular when close interaction among the concentrated vortex lines is encountered. Such a close interaction develops during the iteration procedure used to satisfy the boundary conditions on the wing surface and on the unknown free-vortex surfaces. This is critical when treating wings with highly swept-back leading edges where the rolled-up primary vortex sheets cover a major portion of the wing surface. Moreover, it is also critical when slender quadrilateral vortex elements are used in the model or when elements become slender due to deformation in the free-vortex sheet [46]. Also, when continuous vortex sheet is modelled by discrete vortex filaments, the spurious phenomenon of leap-frogging can occur. The vortex filament

can penetrate what is supposed to be continuous and therefore impenetrable vortex sheet.

To suppress this singularity, a prescribed artificial viscosity coefficient or a prescribed size of rigid-body core rotation can be used, but the resulting aerodynamic loading is sensitive to those parameters. Furthermore, when a vortex sheet is approximated by concentrated vortex lines, Biot-Savart's law is incapable of calculating the self-induced velocity at a point on the vortex sheet and one has to introduce this velocity approximately wherever these field points are encountered during the calculations. Finally, modeling the continuously varying vorticity over a wing panel with a vortex segment of constant strength requires the use of a very large number of these vortex segments to obtain accurate resolution of the flow field.

Later Kandil modified the nonlinear discrete-vortex method and extended the method to predict the inviscid leading- and trailing- vortex cores beyond the trailing edge [12,51,52]. His model alleviates the problems previously encountered in predicting satisfactory pressure distributions. This is accomplished by lumping the free-vortex lines during the iteration procedure. The leading- and trailing-edge cores and their feeding sheets are obtained as parts of the solution. His numerical results show that the modified NDV-method is successful in confirming the formation of a trailing-edge core with opposite roll-up and opposite circulation to those of the leading-edge core. This work was considered by some to be a breakthrough in the NDV-methods since it was the first numerical calculation of this phenomenon.

An extensive review of this method can be found in Reference [53].

2.3.2.3. Doublet Panel Methods

Johnson et al. [54-59] developed a doublet panel method to model separated flows. The essential elements of the model are the configuration surfaces (wing, body, etc.), the trailing sheet (wake), the leading edge vortex sheet (free sheet), and the inner turns of the LE vortex sheet and inviscid core (fed sheet and core). The purpose of the fed sheet is to approximate the inner turns of the free sheet. The following conditions were imposed on these elements:

1. The flow must be tangential to the wing, wake, and free sheet.
2. The free sheet must be force free in cross flow planes.
3. A prescribed wake (a design wake) must be force free.
4. The fed sheet size and core orientation should be such that the total force on the fed sheet and core be parallel to the core.
5. Kutta conditions must apply along the edges of separation.

The initial code featured planar quadrilateral panels with a frozen near field wake. Subsequently the wake treatment was refined and quadrilateral panels with paraboloid curvature were adopted. Tests [60] indicated that for seemingly random cases, the shape and position of the free sheet became unstable, making parametric studies difficult. Changes in wing paneling caused well converged cases to diverge. This required a general upgrade of the numerics [57,58]. Continuous doublet splines and hyperboloid panels were used to ensure continuity of geometry and doublet singularity across panel edges, thus eliminating the ring vortices created by a discontinuity in the doublet strength between adjacent panels. The built-in instability due to kinks in the vortex sheet, while updating the vortex sheet, was damped out by a least square technique.

Comparisons with experiments indicate that the pressure peaks are underpredicted for a unit aspect ratio (AR) delta wing at twenty degrees angle of attack. The agreement of the lift and pressure coefficients for certain AR delta wings at twenty degrees angle of attack was good.

In addition to Boeing's LEV method, several research works [61-67] have been done by using doublet panel method. The work developed by Hoeijmakers et al. [62-64], namely $VORSEP$, is based on the same formulation as the LEV method. However, the numerical implementation differs in several points. The detailed description of $VORSEP$ and the comparisons among the results of $VORSEP$, LEV and experiments can be found in Reference [22].

Morino et al. also developed a surface panel method using doublet potential to solve aerodynamic problems about general configurations with prescribed wake [68-71] and with wake deformation [72].

2.3.2.4. Vortex Panel Methods

Considering the shortcomings of the NDV [52] in modeling the continuous bound and free vortex sheets, Kandil et al. [73] developed the Hybrid Vortex Method (HVM), where the vortex sheets are approximated by quadrilateral vortex panels for the near field calculations. In the far field calculations, the vortex panels are lumped into line vortices. On each vortex panel, a local linear vorticity distribution, which satisfies the solenoidal property of the vorticity vector is specified. Such a distribution which satisfies the solenoidal property contains five undetermined coefficients per panel, which constitute the basic unknowns of the problem, along with the free vortex sheets.

Closed form expressions were determined for the velocity induced by rectangular or triangular vortex panels. Initially this was computationally inefficient because a semi-analytical method was used whereby the integration was performed analytically in one direction, numerically in the other. Later, the closed form expressions, which were efficiently coded were used. The vorticity components of the free vortex panels were related to the bound vortex panels at the edges of separation by equating the outflow of vorticity from the bound vortex panels to the inflow of vorticity into the free vortex panels along the edges of separation. In this way, the unknowns were restricted to the coefficients of the bound vortex panels.

The unknown coefficients are determined by satisfying the flow tangency condition at the centroids of bound vortex panels, the Kutta condition along the edges of separation, compatibility conditions requiring the continuity of vorticity between adjacent panels, and a symmetry condition along the centerline. These conditions were satisfied iteratively, which alternately yields the vorticity distribution and the shape of the free vortex sheet.

To reduce the total number of unknowns of the problem, the unknown coefficients of the free vortex panels were related to the coefficients of the bound vortex panels at the edge of separation by enforcing five conditions [74]. The five conditions or equations for panel $ms1$ in Fig. 4 are given by:

1. Continuity of vorticity at node (i, j)

$$\omega(i,j) = \omega_\zeta(4, jmr) = \omega_\zeta(4, ms1) \tag{2.1}$$

2. Direction of the vorticity vector at node $(1, ms1)$ is along side $1-4$

$$\omega_\xi(1, ms1) = 0 \tag{2.2}$$

3. Direction of the vorticity vector at node $(2, ms1)$ is along side $2-3$

4. Conservation of circulation across the common side of vortex panels jmr and $ms1$ require that

$$\int_1^2 \vec{\omega} \cdot d\vec{\ell}\Big|_{ms1} = \int_4^3 \vec{\omega} \cdot d\vec{\ell}\Big|_{jmr} \tag{2.3}$$

where $d\vec{\ell} = \vec{n} d\ell$, $\vec{n}$ is the unit vector normal to $d\ell$ and in plane of element and $d\ell$ is an infinitesimal length of the common side.

5. Conservation of circulation over the panel $ms1$ requires that

$$\int_{ms1} \vec{\omega} \cdot d\vec{\ell} = 0 \tag{2.4}$$

The fifth condition, Eq. (2.4), is applied to the approximate mean plane which passes through the centroid of the original non-planar panel. This condition, although it might look redundant, ensures the continuity of the circulation on the approximate planar panel, since the actual panel is nonplanar.

The HVM was used to solve for the steady flow past a rectangular wing having side edge separation [74,75]. A converged shape of free vortex sheet from the lattice method of Kandil was used as an initial guess. This process drastically cut the computational time. The spanwise pressure distribution at two chord locations, and section normal force coefficients were shown to match well with experiments [74].

Later, the HVM was modified to use the global nodal vorticities instead of the local vorticity distribution coefficients as basic unknowns [53]. This modification is done by using a finite-element type approach which automatically ensures continuity of vorticities between adjacent panels and also reduces the number of unknowns tremendously. Yen et. al [76-78] developed a continuous vorticity panel method which is similar to the modified global vortex panel method. The conservation condition implemented by Yen in a way similar to that used in [73,74]. The way the Kutta condition implemented in [77] by forcing the vortex line othogonal to the edge of separation limits the applications to flows with low Mach numbers and at low to moderate angle of attack. In general, the numerical results of the vortex panel method are in good agreement with experimental results.

2.3.3. Vortex-Capturing Methods

Finite-difference and finite-volume methods have been widely used to solve the Euler equations. The application of these methods to the prediction of vortex flow about different configurations at angle of attack has been an area of active research. A controversy, however, concerning the origin of the separation in the numerical simulation of an inviscid flow was brought up and has been discussed by many researchers. Two hypotheses were suggested [79]: The first hypothesis suggests that the vorticity necessary for flow separation may be generated by the transient appearance of a shock as the flow expands. The second hypothesis suggests that separation occurs due to numerical dissipation in the algorithm.

Newsome & Kandil stated in their survey report [79] that in theory, there is only one mechanism, other than sharp edges, for vorticity generation in an inviscid flow, namely, the shock. In accord with Crocco's theorem for steady flow

$$\vec{V} \times \vec{\omega} = \nabla h_t - T\nabla S \tag{2.5}$$

where $\vec{V}$ is the velocity, $\vec{\omega}$ the vorticity, S the entropy and h_t the total enthalpy, the Euler equations allow for the generation of vorticity through non-constant shock strength (shock curvature, shock intersection, etc.) For an inviscid flow, entropy is constant along streamlines except in crossing a shock where the entropy jump is a function of the local strength. The gradient in entropy normal to streamlines results in the production of vorticity. The significance of vorticity generation is clear when it is realized that the presence of vorticity in the flow coupled with an adverse pressure gradient are necessary for flow separation.

From the discussion above, it is clear that theoretically valid solutions to the Euler equations with flow separation exist only in shock flow. This has also been demonstrated numerically by Salas [80] and Marconi [81,82]. Although such inviscid solutions are theoretically valid, they do not necessarily provide an accurate description of the separation that occurs in the actual viscous flow.

In the past several years, numerous solutions to the conservative Euler equations for the conical and three-dimensional flow about delta wings with both sharp and rounded subsonic leading edges have been reported. The computations invariably reveal the characteristic leading-edge separation vortex. The computed surface pressure coefficient frequently shows qualitative agreement with experimental measurements. Eriksson & Rizzi [83] used Euler equations with relatively coarse grids to predict the vortical flow around slender wings. In this time-marching method, a vortical flow was generated without explicitly satisfying a Kutta type of condition at the leading edge. Comparing the computed results with experimental data and

the results from a panel method, one finds that the magnitude of vorticity strength in the vortical flow region is small and the vorticity distribution is spread unrealistically. As a result the computed upper surface suction peaks are lower than those computed by a panel method and also lower than the experimental results. Later, Rizzi used different mesh densities to solve different wing flows [84-86]. In both the coarse and fine grid transonic and supersonic solutions, the flow separates at the leading edge forming the primary vortex. Both the fine and coarse grid solutions exhibit large total pressure losses of similar magnitude in the vortex core. An interesting comparison between the computed results from Euler equations and the panel method VORSEP for flow around a delta wing with a 70 degree of sweep angle and at a 20 degree of angle-of-attack is given by Hoijmakers & Rizzi [87].

Similar leading-edge separation vortices have been reported for both rounded and sharp leading edges using a variety of numerical schemes. A partial list includes the works of Raj & Sikora [88], Murman & Powell [89] with the finite-volume Runge-Kutta algorithm; Fujii & Obayashi [90] using an LU factored scheme; and Manie, et al. [91] and Newsome [92] using a MacCormack scheme. Two rather basic questions have risen out of these and similar solutions: in the absence of a clearly defined physical mechanism, such as shock curvature, how does separation occur in an inviscid flow and what is the mechanism leading to large total pressure losses? Two hypotheses have been suggested. The first hypothesis [93] suggests that the vorticity necessary for flow separation may be generated by the transient appearance of a shock as the flow expands around the leading edge. The second hypothesis suggests that separation occurs due to numerical dissipation in the scheme algorithm. The same two explanations have been given for the related question of why Euler equation solutions for lifting airfoils produce the correct pressure distribution without an explicitly imposed Kutta condition [84], as is necessary for the potential equation.

In the past several years, numerous papers have addressed the above-mentioned problems with different numerical schemes and proposed different points of view on the causes for the pressure loss and for the separation. Newsome [94] applied a central difference scheme to both the Navier-Stokes and the Euler equations to solve the supersonic conical flow about a thin elliptic cone. The solutions clearly showed that the leading-edge separation for the rounded leading edge is entirely a numerical phenomenon. Kandil & Chuang [95] used a finite-volume Runge-Kutta scheme to solve similar flow problems. Their solutions showed conclusively that numerical dissipation was responsible for inviscid separation about rounded edges. Powell, et al. [96] explained that the total pressure loss is due to the finite thickness of the vortex region and the finite thickness is created when applying the central difference scheme with added artificial viscosity to produce the weak solutions (shocks, contact discontinuities) to the conservative Euler equations. Later, Marconi [97], Powell & Murman [98], and Kandil et al. [99], used different schemes to produce solutions without pressure loss by enforcing the isentropic gas equation. These papers conclusively provide evidence that numerical dissipation is the major cause for the pressure loss and the separation about rounded edges.

Upwind-difference methods have recently been applied to the computation of flow about delta wings. The behavior of the upwind schemes is different from that of the prescribed central difference schemes. Since the upwind discretization is naturally dissipative, no added artificial viscosity is necessary. Surprisingly, the solutions for the flow about the previously described elliptic cone with upwind difference schemes showed no evidence of leading-edge separation.

An extensive review of various finite difference/finite volume methods to solve Euler equations for vortical flow is given by Newsome & Kandil [79].

In general, using Euler equations with finite difference schemes to solve the vortical flow problems seems to be promising particularly for sharp-edged wings. However, the topology of the vortex flow has to be known in some detail to enable the construction of a computational grid with sufficient resolution at the vortex layer and cores. Also the sometimes excessive spreading of vortical regions and the vorticity production process (Kutta condition) need further investigation. An important aspect of Euler methods which needs to be mentioned is that they also account for non-linear compressibility effects (shock waves) and for the mutual interaction of vortical flow regions and shock waves.

2.3.4. Transonic Flow Methods

As we mentioned before, shock waves and viscous effects are of interest to aerodynamicist because they influence the aerodynamic characteristics, e.g., lift and drag coefficients of the wing. In transonic flows, the most distinguishing feature is the mixed subsonic-supersonic flow character. The governing equation is nonlinear, an analytical solution is impossible to obtain for a general configuration. Fortunately, attempts to obtain numerical solutions have met with more success. A great deal of effort has been spent to find ways to calculate the transonic flows and a variety of analytical and numerical methods have been introduced. Excellent reviews of the work on transonic flow before the mid-seventies are given by Cole [100] and Spreiter [141].

2.3.4.1. Finite Difference Methods

Finite difference methods have played an important role in transonic flow calculations ever since Lax [101] introduced weak solutions to the partial differential

equations to make the calculation of flow discontinuity possible. The first major breakthrough was made by Magnus and Yoshihara [102], who demonstrated that solutions for two-dimensional, inviscid, transonic flow fields could be computed using finite difference methods. Steady-state solutions were obtained as large time-asymptotic solutions to a time accurate formulation of the problem.

Murman and Cole [103] later developed the well-known type-dependent finite difference relaxation method to solve the steady-state problem, which saved about an order of magnitude of computer time compared to the method of Magnus and Yoshihara. The type-dependent finite difference method is a method which accounts for the fundamentally different behavior of subsonic and supersonic flow, i.e., a central difference scheme is used in subsonic flow region (or elliptic region) and an upwind difference scheme is used in the supersonic flow region (or hyperbolic region). This type of difference scheme also reduces the possibility of solutions without physical meaning which could result from the central difference scheme in the shock region [121]. The computed results match well with the experimental results in both shock location and strength for weak shocks. These initial successes gave birth to a new field of study, computational transonic aerodynamics.

Since then, steady and unsteady transonic flows without strong vortex flow have been successfully solved using the transonic small perturbation (TSP) equation [103-107] and the full potential (FP) equation [108-113]. The TSP method substantially simplifies the governing equations and especially, the treatment of boundary conditions in both three-dimensional and unsteady computational transonic aerodynamics. They provide solutions that are useful in qualitatively predicting the behavior of these complex flows. Furthermore, quantitatively good predictions can often be obtained by properly "tuning" the small-disturbance procedures.

Two relaxation schemes have been developed for the TSP equation. The first one is called the non-conservative relaxation schemes (NCR) firstly developed by Murman and Cole [103], whose results do not satisfy the shock-jump conditions. Murman [115] later modified the schemes to satisfy the proper jump conditions. Such schemes are known as the fully conservative relaxation (FCR) schemes. For shock free flows, finite difference equations in the NCR form that are consistent with the differential equations are also consistent with the integral forms of the equations. However, internal fluxes between mesh cells do not cancel identically, but rather cancel within a truncation error. For flows with shock waves, the FCR form must be used to calculate the correct shock jumps. Artificial viscosity is not in the conservation form in the NCR scheme while is in the conservation form in FCR scheme. One interesting thing is that the results with the NCR scheme predict shock location better than those with the FCR scheme. One possible reason is that the error due to an improper shock jump condition in the NCR scheme is counterbalanced by the error from the inviscid assumption. Similar comments on and an extensive review of NCR and FCR schemes have been presented by Ballhaus [106] and by Spreiter [141].

Bailey and Ballhaus [104] used the simplified form of the transonic small disturbance equation to develop solutions for three-dimensional wings. Their work led to the development of a widely used three-dimensional code for transonic wing analysis. This code has been used extensively in designing improved wings for flight in the transonic speed regime. Jameson [105] also introduced his well-known rotated difference scheme, in which the direction of upwind differencing is independent of the coordinate system, and is instead rotated to conform with the local flow direction. This difference scheme is used to eliminate the stability problem in supersonic region which resulted from the negative artificial viscosity in Cartesian grid system.

In solving transonic problems using finite-difference methods, proper treatment of boundary conditions is often more difficult than the solution of the governing equations. Boundary conditions are usually treated by either coordinate transformations, approximations (as in the small perturbation approaches), or both. An alternative approach is provided by the finite volume method, introduced by MacCormack and Paullay [116-118], which they modified, and applied to blunt-body problems. The principal advantage of the method is that the governing equations are solved in a Cartesian coordinate system using a body-oriented and shock-oriented mesh network. One need only know the volume and surface normal directions of the volume elements. Later, Rizzi applied this method to the Euler equations [119], Caughey and Jameson applied it to the full potential equation [120].

Murman and Stremel [121]used an adaptation of Baker's "cloud in cell" algorithm to model a vortex wake behind a large aspect-ratio wing with a known spanwise lift distribution. Although the problem considered is simple compared to the complexity of transonic vortex flows around fighter aircraft, it demonstrated the feasibility of solving transonic vortex flow using the potential equation through a finite-difference method.

The potential flow equation can be used for flows with weak shocks since the entropy increase and vorticity production across these shocks are small (where the normal Mach numbers M_n are close to 1). The entropy production across a weak shock may be written as [122]

$$\frac{\Delta s}{R} \approx \frac{2\gamma}{\gamma+1}(M_n^2 - 1)^3$$

For shocks with moderate strength (where M_n is less than 1.3), one has to correct the potential equations in order to include the entropy jump across the shock wave.

Hafez et al. [123] applied the idea of artificial compressibility in transonic flows in order to provide artificial viscosity in supersonic regions. This concept was originally introduced by Harten [124] in attempting to devise better methods of shock capturing in supersonic flows. Fuslang and Williams [125] used an entropy correction term to predict shock location and strength. For flow with strong shocks, the potential equation will break down unless the entropy change and vorticity production due to the shock are carefully taken into account.

In order to simulate experimental results, it is important to add the viscous effects of the boundary layer, i.e., to add the displacement thickness of the boundary layer to the profile [126,127]. This improves in both the computed shock strength and its location when compares with experimental results. This procedure is effective in the regime where the shock waves are not strong enough to separate the flow. The solution by this method is obtained when both flow field and boundary layer converge.

Euler equations, in principle should admit accurate solutions for rotational flows with shock waves. Several recent methods that use the strong conservative form of the unsteady Euler equations have been developed to solve for steady and unsteady transonic flows [118,129,130]. For steady flows, the unsteady equations, which are hyperbolic, are solved in pseudo-time. In all these methods, different versions of the finite- volume method have been developed.

Steger and Warming [131] developed an implicit algorithm using a splitting of flux vectors in the Euler equations. While the precise splitting can be accomplished in several ways, the usual way is according to the signs of the eigenvalues of the system as is the case in the split coefficient matrix (SCM) method. The use of split flux

techniques for shock capturing applications produces somewhat better results than the standard central difference schemes but problems remain even in this formulation. Small oscillations occur near a sonic line because the flux splitting depends on the eigenvalues. These flux terms have a discontinuous first derivative when eigenvalues change sign. The SCM method is a relatively recent addition to the class of finite difference methods for solving hyperbolic PDE's. The SCM scheme introduced by Chakravarthy [132] and Chakravarthy et al. [133] is a nonconservation form of the split flux scheme proposed by Steger [134]. The SCM method utilizes information on signal propagation provided by the method and theory of characteristics. Thus, we might expect better results from the SCM method than those from other methods. This is true and SCM method is recommended for use when solving hyperbolic PDE's in nonconservative form. A detailed description of these schemes can be found by Anderson et al. [135].

The pseudo-time marching technique, developed by MacCormack & Rizzi [136], has been used to solve low supersonic flow in which a subsonic flows region is embedded. The advantage of this technique is that the governing equation is "converted" from originally a mixed type (elliptic and hyperbolic) to a pure hyperbolic type. Solutions to the mixed elliptic and hyperbolic steady flow equations are asymptotic in time.

In general, finite difference methods with Euler equations can usually predict transonic flows accurately even with strong shocks. In order to avoid the dispersion effect in the shock region, artificial viscosities are added in the numerical schemes with central differencing, which also dissipate the viscous effects of vortex flows. Consequently, as mentioned in the previous section, the total pressure generated by the vortex core in the transonic vortex flow will be reduced. This requires

more careful and in-depth study of the role and effect of artificial viscosity in the numerical scheme before it is applied to a real design. Another drawback for finite difference methods is the construction of a suitable curvilinear coordinate system, which requires a certain amount of ingenuity and becomes more difficult with each increase in geometric complexity of the configuration. The scheme of integrating the time dependent Euler equations until they reach a steady state has been widely used [137-141]. This is generally slow and requires a large computer memory. Hence, it seems promising to develop a more rapid convergent method to solve the steady-state Euler equations.

2.3.4.2. Integral Equation Methods

The integral equation methods (panel methods) have long been used for aerodynamic design in subsonic and supersonic speed ranges. The development of these methods for transonic flow probably started in the early fifties. An extensive historical review of these methods can be found in Spreiter [141]. Those works include Spreiter & Alksne [142], Oswatitsch [143], and Guderley [144]. In their methods, a transonic small perturbation equation and the associated boundary conditions were recast into the form of a nonlinear integral equation by application of Green's theorem to appropriate regions surrounding the airfoil, its wake, and any shock waves that may be present. Their results obtained from hand calculations match with experimental results qualitatively. More importantly, they showed the capability of capturing shocks with integral equation methods.

Crown [145] modified the integral form and also provided a more rigorous analysis with error estimates of the various assumptions and approximations. The test cases were in the low transonic range for which the flow is subsonic with embedded supersonic regions terminated by a shock wave normal to the surface (at the

surface). Entropy gradients behind the shock are allowed but specific heats are assumed constant. Solutions were obtained by iteration. This also started the use of the digital computer for the integral equation method in transonic flow research. Spreiter & Stahara [146] applied their technique with local linearization methods for axisymmetric flow and the transonic equivalence rule for a number of slender, pointed, axisymmetric and non-axisymmetric bodies, including simple wing-body combination, for both lifting and nonlifting conditions.

Nixon [147] improved the method of Spreiter & Alksne [142] by introducing a simple correction factor depending on the transonic similarity parameter. His results match favorably with those by Murman & Cole [103] and by Steger & Lomax [109]. Later, he pointed out that the number of iterative steps to a converged solution for the integral equation method is small compared with that required by the finite difference method and in two-dimensional calculations, the over-all computing time is at least comparable with that of the finite difference methods [148].

Morino et al [149], showed in a general formulation that the integral equation is of the shock-capturing type and that the contribution of the shock, as a surface of source distribution, is embedded in the volume integral term representing nonlinear compressibility. All that is needed to capture the shock is to compute accurately the derivatives of the volume integral term. They also showed numerical results with transonic small perturbations for three-dimensional steady and unsteady flows with prescribed wake [150,151]. Although shock capturing was demonstrated, it apparently was not carried out using a fine computational grid, due to the limited memory storage of their computer.

Piers & Slooff [152] applied integral equation method to a two-dimensional small perturbation equation to solve shock flows around airfoils. In order to obtain

a unique and physically meaningful solution, they modified the TSP equation by adding a term whose role is similar to that of artificial viscosity. The velocity field is divided into a subsonic flow element governed by the linear part of TSP equaton, i.e., the Prandtl-Glauert equation, and a perturbation velocity obtained from the integral form of the nonlinear part of equation. The solution procedure starts from the solution of the Prandtl-Glauert equation. The field perturbation velocity is then calculated by using finite difference methods to minimize a residual function which is constructed in terms of the Prandtl-Glauert solution. The linear solution is fixed throughout the calculation of the perturbation velocity. In this method, the panel method solution is used for two purposes. First, as a good initial guess to solve for the field velocity and; Second, to confine the computational domain for finite difference calculations.

Johnson et al [153] embedded a transonic rectangular grid in the panel method developed by the Boeing Company. The artificial density was introduced into the variational error function which was minimized during the solution process. The problem was reduced tc a sequence of Poisson equations through the least square and optimal control methods developed by Bristeau et al [154]. The Poisson equations were then solved using fast Fourier transforms and panel methods. Erickson et al [155] combined this approach with PANAIR, a linear source, quadratic doublet panel method, to solve two-dimensional transonic flow problems.

Kandil [156] and Kandil & Yates [2] applied shock-capturing and shock-fitting (SCSF) techniques to the integral equation method to solve the three-dimensional full potential equation: In the shock-capturing technique, the compressible full potential equation is solved iteratively to satisfy the flow tangency condition on the wing, the Kutta condition along the separation edges, and the flow tangency and no

pressure jump conditions on the free vortex sheets. The nonlinear compressibility term containing density gradients are calculated using a backward/central difference scheme of the Murman-Cole type. The shock is captured as the solution converges.

It should be noted here that the difference between this method and the other methods is that the present formulation is based on the velocity field while the others used velocity potential. Two advantages were found for the present method over other panel methods [147-153]; First, only first order derivatives need to be calculated by finite differencing, and second, one does not need to calculate the derivative of the velocity potential in order to detect the shock formation since the velocity is calculated directly in the present formulation. These advantages are particularly significant since numerical instability, if any, usually comes from numerical operators (e.g., finite difference schemes). In order to obtain high accuracy in the numerical calculation of velocity from the velocity potential, a fine grid must be used and consequently the computational time is increased; if a coarse grid is used instead, numerical instability might occur and the solution may not converge. Therefore, this method seems more stable and faster than those using velocity potentials. The current problem for this method is that it requires a larger memory when solving problems with complicated configurations, this should be overcome by using large computers with massive parallel processing capabilities.

In order to locate accurately the shock position, a fine grid should be used, consequently the computational time is increased. To remedy this, a shock-fitting technique is introduced after the shock is captured approximately. In the shock-fitting technique, the contribution of the shock to the velocity field is represented by an explicit surface-integral based source distribution. The strength, location and shape of the shock surface are calculated through the Rankine-Hugoniot relations.

The converged solution, including strength, location and shape of the shock surface are solved iteratively by satisfying all boundary conditions. Such a technique sharpens the shock without requiring local grid refinement. Although, like others, Kandil and Yates showed only the numerical results of the shock-capturing technique, the SCSF techniques seem very promising for integral equation method to solve transonic vortex flows. Later, Kandil and Hu [157] applied SCSF to solve two-dimensional transonic flow problems where they demonstrated the numerical advantages of SCSF techniques. A similar shock-capturing method with velocity potential was used by Sinclair [158] to solve various two-dimensional problems.

Samant et al. [159] developed a computer technique TRANAIR using the full potential equation to solve three-dimensional transonic flows about arbitrary configurations. In this technique, they combined several algorithms including finite elements, the Bateman variational principle [160], Green's function theory (integral equation method), James convolution algorithm [161], and a generalized conjugate gradient technique GMRES [162]. They showed very impressive numerical results for a complete airplane.

In general, the integral equation methods seem to be stable and less dissipative than current finite difference methods when solving low transonic flow problems. The reason is that the calculation of the velocity at a field point depends mainly on the calculations from panel methods which have been proved to be very stable in solving subsonic dominated flow problems. The only source of numerical instability is from the differencing of velocities (or density) at field points, which can be easily controlled by a numerically efficient local grid refinement.

2.3.4.3. Miscellaneous Methods

Some methods other than those mentioned above have either long been used or just been developed for transonic flow calculations and are worth being mentioned here, e.g., finite element methods, mixed-type methods, etc.

The finite element method has been extended to treat equations of the mixed type which also provides a way to circumvent the difficulties of treating complex configurations by finite difference methods [163]. Some recently developed methods [154,164] have been used widely in transonic flow calculations. Several ideas introduced by those methods have stimulated many researchers to combine different techniques to solve complicated problems. The TRANAIR [159], program developed by researchers at the Boeing Company and at NASA Ames Research Center, has been successful.

Chen et al. [165], used an integral equation solution to confine the far-field boundary for the finite difference calculations, which reduced the size of computational domain tremendously and consequently reduced the computational time. Later, Lee et al. [166] introduced a "middle field" of large finite elements between the panel method far-field and the finite difference inner field. Lee's approach enabled further reduction in the size of the finite difference region and thus the cost, while avoiding linear flow solutions in the highly nonlinear region.

Since transonic flow is characterized by a mixed-type equation, i.e., the flow field is characterized by both an elliptic operator (in the subsonic speed region) and a hyperbolic operator (in the supersonic speed region). In high transonic speed region (low supersonic speed region), the flow field is dominated by supersonic flow with some small local subsonic regions in the field. This can be solved with

supersonic flow approaches (hyperbolic equation) with embedded subsonic regions. On the other hand, in the low transonic speed range (high subsonic speed range), the flow can be solved with subsonic flow approaches (elliptic equation) with embedded supersonic regions. These types of methods have been proved numerically efficient and accurate. Kandil & Hu [167,168] used integral equation methods with embedded Euler domains to solve various two-dimensional transonic flow problems. Their results, when compared with those from SCSF methods and from finite difference methods, showed the power of this method. That is, this method, like solution of Euler equations with finite difference methods, can analyze flows with stronger shocks while still maintaining the geometric flexibility, computational efficiency, and numerical stability of panel methods.

Some excellent reference books [169-172] have been added to the reference list. Many valuable theoretical derivations and historical reviews mentioned in most papers reviewed here can be found in those books.

Chapter 3

FORMULATION AND METHOD OF SOLUTION — INCOMPRESSIBLE FLOW

3.1. Formulation of the Problem

The velocity field of a flow can be expressed through the Helmholtz decomposition as a combination of an irrotational or a potential flow field and a rotational or a solenoidal flow field [26], i.e.

$$\begin{aligned} \vec{V} &= \vec{V}_{pot} + \vec{V}_{rot} \\ &= \nabla\Phi + \nabla \times \vec{A} \end{aligned} \tag{3.1}$$

where the Φ is the total velocity potential and $\vec{A}$ is the vector potential of the rotational field, from which the solenoidal velocity is generated. By taking the curl of Eq. (3.1), one finds that $\vec{A}$ is related to the vorticity field $\vec{\omega}$ by $\nabla^2\vec{A} = -\vec{\omega}$.

For an incompressible and irrotational flow in the region R outside a wing and its free-vortex sheets, Figure 2a, the governing equation can be expressed as a total velocity potential Φ satisfying Laplace's equation.

$$\nabla^2\Phi = 0 \tag{3.2}$$

The total velocity potential at field point $P(x, y, z)$ can also be expressed as

$$\begin{aligned}\Phi &= \Phi_\infty + \phi \\ &= |\vec{V}_\infty| x + \phi\end{aligned} \tag{3.3}$$

where Φ_∞ is the velocity potential of free stream, $\vec{V}_\infty$ the free stream velocity, and ϕ the perturbation velocity potential which also satisfies Laplace's equation.

$$\nabla^2 \phi = 0 \tag{3.4}$$

On the boundary ∂R, the following conditions are to be satisfied:

(a) a flow tangency condition on the wing

$$(\nabla \phi + \vec{e}_\infty) \cdot \vec{n}_s = 0 \quad \text{on} \quad S(\vec{r}) = 0 \tag{3.5}$$

(b) a flow tangency condition on the free-vortex sheets

$$(\nabla \phi + \vec{e}_\infty) \cdot \vec{n}_w = 0 \quad \text{on} \quad W(\vec{r}) = 0 \tag{3.6}$$

(c) a zero pressure jump condition across the free-vortex sheets

$$\begin{aligned}\triangle C_p = C_{p_u} - C_{p_l} &= -4\vec{V}_{ju} \cdot (\vec{e}_\infty + \vec{V}_{ind}) \\ &= -4\omega \vec{e}_t \cdot (\vec{e}_\infty + \vec{V}_{ind}) = 0 \quad \text{on} \quad W(\vec{r}) = 0\end{aligned} \tag{3.7}$$

where $\vec{e}_t = \vec{e}_\omega \times \vec{n}_w$ and $\vec{e}_\omega$ is the unit vector of $\vec{\omega}$, and $\vec{V}_{ju}$ is the velocity jump between upper and lower surfaces.

It should be noticed here that Eqs. (3.6) and (3.7) can be satisfied simultaneously by requiring that $\vec{e}_\infty + \vec{V}_{ind}$ be parallel to $\vec{\omega}$.

(d) a Kutta condition along the edges of separation

$$\triangle C_p \Big|_{TE,SE,LE} = 0 \tag{3.8}$$

(e) an infinity condition away from the wing and its free-vortex sheet

$$\nabla\phi \to 0 \quad \text{away from} \quad S = 0 \quad \text{and} \quad W = 0 \tag{3.9}$$

Since the Laplacian is a linear operator, the superposition of solutions can be used. Therefore, the solutions to Eq. (3.2) with Boundary Conditions (3.5) – (3.9) are given by a sum of source and doublet surface integrals as well as the free stream velocity potential

$$\Phi_p(x,y,z) = \Phi_\infty + \frac{1}{4\pi}\int\int_s \frac{q}{r}ds + \frac{1}{4\pi}\int\int_{s,w} \mu\frac{\partial}{\partial n}(\frac{1}{r})ds \tag{3.10}$$

where q is the strength of a source distribution on the solid boundary, μ the strength of a doublet distribution on the boundary, and r the distance between the field point (x,y,z) and the source or doublet point (ξ,η,ς), given by

$$r = [(x-\xi)^2 + (y-\eta)^2 + (z-\varsigma)^2]^{\frac{1}{2}}$$

Taking the gradient of Eq. (3.10) and replacing the surface doublet term by an equivalent surface vorticity term, we obtain the expression for velocity field

$$\vec{V}_p(x,y,z) = \vec{V}_\infty - \frac{1}{4\pi}\int\int_s \frac{q(\xi,\eta,\varsigma)}{r^2}\vec{e}_r ds + \frac{1}{4\pi}\int\int_{s,w} \frac{\vec{\omega}(\xi,\eta,\varsigma)\times\vec{e}_r}{r^2}ds \tag{3.11}$$

For a wing without thickness, the second term on the RHS of Eq. (3.11) will vanish and the third term can be integrated to closed-form expressions for some forms of vorticity distributions. Since we are interested in the study of vortex dynamics, the current work is limited to the case of a zero-thickness, flat, rectangular wing with free-vortex sheets but the method can be extended to any kind of configuration.

3.2. Discretization of the Bound and Free Vortex Sheets

Once the wing and its free-shear layers are represented by vortex sheets, Eqs. (3.4) and (3.9) are automatically satisfied. To determine the vorticity distribution of the vortex sheets and the shape of the free-vortex sheets, one has to satisfy Eqs. (3.5) – (3.8). This is accomplished by using a surface-panel discretization in which the bound and free-vortex sheets are divided into triangular panels. On each vortex panel, a linearly varying vorticity distribution is defined in a local coordinate system in terms of global nodal vorticities. Such a formulation automatically ensures continuity of vorticity between adjacent panels and also reduces the number of unknowns as compared to the Hybrid-Vortex panel method [73-75]. In the present investigation, the basis is that triangular panels can model geometrically the deformed free-vortex sheets more accurately than the planar quadrilateral panels used in the Hybrid-Vortex panel method.

The flow tangency condition on the wing, Eq. (3.5), is satisfied at a set of control points on the bound-vortex panels, while the flow-tangency condition and the no-pressure-jump condition on the free-vortex sheet, Eqs. (3.6) and (3.7), are satisfied simultaneously at control points on the free-vortex panels, Figure 5. Kutta condition, Eq. (3.8), is satisfied at the nodes of the bound-vortex panels along

the edges of separation. Some additional requirements, such as the symmetry condition, vorticity conservation condition which enforces the solenoidal property of vortex field, and the requirement that there be no outflow of vorticity along edges where flow is attached, are enforced. The symmetry condition which states that no flow can cross the centerline is satisfied at the nodes on the centerline. The vorticity conservation condition is satisfied on each bound quadrilateral vortex panel composed of two adjacent triangular panels. Conservation of vorticity is also satisfied on all free vortex panels through the Helmholtz second theory of vorticity. The zero vorticity outflow condition along edges where flow separation does not occur is enforced at all nodes on these edges.

Equations (3.5) – (3.8) are satisfied by using an interative technique which yields, alternatively, the global nodal vorticity and the shape of the free-vortex sheets. Once the iterative technique converges, distributed- and total-aerodynamic characteristics are calculated. To expedite the convergence and to avoid excessive distortions of the free-vortex panels, a good initial guess of the shape of the free-vortex sheets is provided from a solution using a coarse array of panels.

3.2.1. Panel Vorticity Distribution

For each triangular element, a local cartesian coordinate system is introduced, such that the ξ axis and ς axis lie in the plane of the panel, (Fig. 6). The corners or local nodes are labeled 1, 2, and 3 going in the clockwise direction, with the local node 1 coinciding with the origin, and side $1-3$ lying on the ς axis. Since the panel is planar, the vorticity at any point on a panel has components in the ξ and ς directions only. Assuming a linear vorticity distribution, the vorticity at any point on the panel can be expressed in terms of the vorticity at the nodes as

$$\vec{\omega}(\xi,\varsigma) = N_1\vec{\omega}(\xi_1,\varsigma_1) + N_2\vec{\omega}(\xi_2,\varsigma_2) + N_3\vec{\omega}(\xi_3,\varsigma_3) \tag{3.12}$$

where N_i are the linear shape functions given by

$$N_i = a_i + b_i\xi + c_i\varsigma \qquad i = 1,2,3 \tag{3.13}$$

$$a_1 = \frac{[\xi_2\varsigma_3 - \xi_3\varsigma_2]}{2\triangle} \quad b_1 = \frac{[\varsigma_2 - \varsigma_3]}{2\triangle} \quad c_1 = \frac{[\xi_3 - \xi_2]}{2\triangle} \tag{3.14a}$$

$$a_2 = \frac{[\xi_3\varsigma_1 - \xi_1\varsigma_3]}{2\triangle} \quad b_2 = \frac{[\varsigma_3 - \varsigma_1]}{2\triangle} \quad c_2 = \frac{[\xi_1 - \xi_3]}{2\triangle} \tag{3.14b}$$

$$a_3 = \frac{[\xi_1\varsigma_2 - \xi_2\varsigma_1]}{2\triangle} \quad b_3 = \frac{[\varsigma_1 - \varsigma_2]}{2\triangle} \quad c_3 = \frac{[\xi_2 - \xi_1]}{2\triangle} \tag{3.14c}$$

$$2\triangle = (\xi_2 - \xi_1)\varsigma_3 + (\xi_1 - \xi_3)\varsigma_2 + (\xi_3 - \xi_2)\varsigma_1 \tag{3.14d}$$

Thus the shape function N_i is unity at node i and zero at the other two nodes.

The local vorticity components at any point on the panel can be expressed as components in the global coordinate system, or vice versa, provided the direction cosines relating the two coordinate systems are known. For example, if the local nodes 1, 2 and 3 correspond to global nodes (i,j), $(i,j+1)$ and $(i+1,j)$, respectively, then the global components of the vorticity vector at the nodes will be given by

$$\begin{pmatrix} \omega_x(i,j) & \omega_y(i,j) & \omega_z(i,j) \\ \omega_x(i,j+1) & \omega_y(i,j+1) & \omega_z(i,j+1) \\ \omega_x(i+1,j) & \omega_y(i+1,j) & \omega_z(i+1,j) \end{pmatrix} \tag{3.15}$$

$$= \begin{pmatrix} \omega_\xi(1) & \omega_\varsigma(1) \\ \omega_\xi(2) & \omega_\varsigma(2) \\ \omega_\xi(3) & \omega_\varsigma(3) \end{pmatrix} \qquad \begin{pmatrix} d_{\xi x} & d_{\xi y} & d_{\xi z} \\ d_{\varsigma x} & d_{\varsigma y} & d_{\varsigma z} \end{pmatrix}$$

The condition $\vec{\omega} \cdot \vec{n} = 0$ can be further applied at each node which reduces Eq. (3.15) to a simpler form

$$\begin{pmatrix} \omega_\xi(1) & \omega_\varsigma(1) \\ \omega_\xi(2) & \omega_\varsigma(2) \\ \omega_\xi(3) & \omega_\varsigma(3) \end{pmatrix} \tag{3.16a}$$

$$= \begin{pmatrix} \omega_x(i,j) & \omega_z(i,j) \\ \omega_x(i,j+1) & \omega_z(i,j+1) \\ \omega_x(i+1,j) & \omega_z(i+1,j) \end{pmatrix} \begin{pmatrix} d_{\xi x} - d_{\xi y}\frac{d_{nx}}{d_{ny}} & d_{\varsigma x} - d_{\varsigma y}\frac{d_{nx}}{d_{ny}} \\ d_{\xi z} - d_{\xi y}\frac{d_{nz}}{d_{ny}} & d_{\varsigma z} - d_{\varsigma y}\frac{d_{nz}}{d_{ny}} \end{pmatrix}$$

For a flat wing, the Eq. (3.16a) can be further reduced to

$$\begin{pmatrix} \omega_\xi(1) & \omega_\varsigma(1) \\ \omega_\xi(2) & \omega_\varsigma(2) \\ \omega_\xi(3) & \omega_\varsigma(3) \end{pmatrix} \tag{3.16b}$$

$$= \begin{pmatrix} \omega_x(i,j) & \omega_z(i,j) \\ \omega_x(i,j+1) & \omega_z(i,j+1) \\ \omega_x(i+1,j) & \omega_z(i+1,j) \end{pmatrix} \qquad \begin{pmatrix} d_{\xi x} & d_{\varsigma x} \\ d_{\xi z} & d_{\varsigma z} \end{pmatrix}$$

The global vorticity components at the nodes of the elements, which are constants, are the basic unknowns in this problem.

3.2.2. Velocity Field Induced by a Triangular Vortex Panel

3.2.2.1. Near-Field Expressions

The velocity induced at any point in the flow field by a finite volume of vorticity $\vec{\Omega}$ is given by [169]

$$\vec{V}(\vec{r}) = \frac{1}{4\pi} Curl_r \int\int_R \int \frac{\vec{\Omega}(\vec{s})d\forall}{|\vec{r}-\vec{s}|} \tag{3.17}$$

where $\vec{r} = x\vec{e}_\xi + y\vec{e}_\eta + z\vec{e}_\zeta$, $\vec{s} = \xi\vec{e}_\xi + \eta\vec{e}_\eta + \zeta\vec{e}_\zeta$ and $d\forall = d\xi d\eta d\zeta$; $\vec{r}$ locates the field (receiving) point, $\vec{s}$ locates the vortex (sending) point and $d\forall$ is the differential volume.

By reducing the volume distribution of vorticity to a vortex sheet of finite strength $\vec{\omega}(\vec{s}) = \omega_\xi\vec{e}_\xi + \omega_\zeta\vec{e}_\zeta$, the velocity field induced by a triangular vortex panel is given by

$$\vec{V}(\vec{r}) = \frac{-1}{4\pi}\int_{\xi_{1n}}^{\xi_{fn}}\int_{\zeta_{1n}}^{\zeta_{fn}} \frac{y\omega_\zeta\vec{e}_\xi + [(z-\zeta)\omega_\xi - (x-\xi)\omega_\zeta]\vec{e}_\eta - y\omega_\xi\vec{e}_\zeta}{[(x-\xi)^2 + y^2 + (z-\zeta)^2]^{3/2}} d\zeta d\xi \tag{3.18}$$

where ω_ξ and ω_ζ are given by Eq. (3.12). Equation (3.18) is another form of the third term of Eq. (3.11).

Expressing the local components of vorticity in terms of global components of vorticity, i.e.,

$$\omega_\xi(\xi,\zeta) = \sum_{i=1}^{3}(a_i + b_i\xi + c_i\zeta)[d_{\xi x}\omega_x(i) + d_{\xi z}\omega_z(i)] \tag{3.19a}$$

$$\omega_\varsigma(\xi,\varsigma) = \sum_{i=1}^{3}(a_i + b_i\xi + c_i\varsigma)[d_{\varsigma x}\omega_x(i) + d_{\varsigma z}\omega_z(i)] \qquad (3.19b)$$

and substituting Eq. (3.19) into Eq. (3.18) permits integrating to get closed form expressions as follows:

$$V_\xi(\vec{r}) = \sum_{i=1}^{3} P_i[d_{\varsigma x}\omega_x(i) + d_{\varsigma z}\omega_z(i)] \qquad (3.20)$$

$$V_\eta(\vec{r}) = \sum_{i=1}^{3}\{R_i[d_{\xi x}\omega_x(i) + d_{\xi z}\omega_z(i)] + S_i[d_{\varsigma x}\omega_x(i) + d_{\varsigma z}\omega_z(i)]\} \qquad (3.21)$$

$$V_\varsigma(\vec{r}) = \sum_{i=1}^{3} - P_i[d_{\xi x}\omega_x(i) + d_{\xi z}\omega_z(i)] \qquad (3.22)$$

where

$$P_i = \frac{-1}{4\pi}\Big[\frac{-y}{|y|}A_1 a_i + \Big(\frac{-yA_3}{2} - \frac{xyA_1}{|y|} + \frac{ymA_2}{M_1^{1/2}}\Big)b_i + \Big(\frac{-zyA_1}{|y|} - \frac{yA_2}{M_1^{1/2}}\Big)c_i\Big]_{\varsigma_{in},\xi_{in}}^{\varsigma_{fn},\xi_{fn}} \qquad (3.23a)$$

$$\begin{aligned} R_i = \frac{1}{4\pi}\Big\{ & \frac{-A_2}{M_1^{1/2}}a_i - \Big(\frac{r}{M_1} + \frac{(x + m(z-I))A_2}{M_1^{3/2}}\Big)b_i \\ & - \Big[\frac{x}{2}A_3 - |y|A_1 - \xi - \frac{x}{2}\ell n|(x-\xi)^2 + y^2| + y\tan^{-1}\frac{(\xi - x)}{y} + \frac{mr}{M_1} \\ & + \Big[z + \frac{m^2(2z - I - xm)}{M_1^{3/2}}\Big]A_2 + \xi\ell n|2(z - I - m\xi) + 2r|\Big]c_i\Big\}_{\varsigma_{in},\xi_{in}}^{\varsigma_{fn},\xi_{fn}} \end{aligned} \qquad (3.23b)$$

$$S_i = \frac{1}{4\pi}\{(\frac{A_3}{2} - \frac{mA_2}{M_1^{1/2}})a_i + [\frac{x}{2}A_3 - (\frac{xm(1+M^2)+(I-z+xm)}{M_1^{3/2}})A_2 - |y|A_1 - \frac{mr}{M_1}]b_i + [\frac{r}{M_1} - m\frac{(I+xm+zm^2)}{M_1^{3/2}}A_2 + \frac{z}{2}A_3]c_i\}_{\zeta_{in},\xi_{in}}^{\zeta_{fn},\xi_{fn}} \tag{3.23c}$$

$$A_1 = tan^{-1}\frac{(z-I-xm)(\xi-x)+y^2m}{|y|r} \tag{3.23d}$$

$$A_2 = \ell n[2M_1^{1/2}r + 2M_1\xi + 2m(I-z) - 2x] \tag{3.23e}$$

$$A_3 = \ell n[\frac{z-I-m\xi-r}{z-I-m\xi+r}] \tag{3.23f}$$

$$M_1 = 1 + m^2 \tag{3.23g}$$

$$r = [(x-\xi)^2 + y^2 + (z-\varsigma)^2]^{1/2} \tag{3.23h}$$

$$m_{fn} = \frac{\varsigma_3 - \varsigma_2}{\xi_3 - \xi_2} \qquad m_{in} = \frac{\varsigma_2 - \varsigma_1}{\xi_2 - \xi_1} \tag{3.23i}$$

$$I_{fn} = \frac{\varsigma_2\xi_1 - \xi_2\varsigma_1}{(\xi_3 - \xi_2)} \qquad I_{in} = \frac{\varsigma_1\xi_2 - \varsigma_2\xi_1}{(\xi_2 - \xi_1)} \tag{3.23j}$$

The analytically integrated expressions for the velocity field induced by a triangular vortex panel are also available in [75].

3.2.2.2. Far-Field Expressions

Because of the computational cost involved in calculating the induced velocity as given above, we use the distributed-vorticity expressions for the near-field calculations only. The velocities induced at some distance from the vortex panel (far field) can be calculated with good accurancy by treating the vorticity distribution as constant over the panel. With this approximation, Eq. (3.18) can be simplified as

$$\vec{V}(\vec{r}) = \frac{-S}{4\pi d^3}\{y\bar{\omega}_\varsigma \vec{e}_\xi + [(z-\bar{\varsigma})\bar{\omega}_\xi - (x-\bar{\xi})\bar{\omega}_\varsigma]\vec{e}_\eta - y\bar{\omega}_\xi \vec{e}_\varsigma\} \tag{3.24}$$

where $\bar{\xi}$ and $\bar{\varsigma}$ are local coordinates of the centroid of the vortex panel, S the area of the vortex panel, d the distance between the field point and the centroid, and $\bar{\omega}_\xi$ and $\bar{\omega}_\varsigma$ are mean average vorticities over the panel defined as

$$\bar{\omega}_\xi = \frac{1}{S}\int\int \omega_\xi dS \tag{3.25a}$$

$$\bar{\omega}_\varsigma = \frac{1}{S}\int\int \omega_\varsigma dS \tag{3.25b}$$

Substituting Eq. (3.19) into Eq. (3.25) and carrying out the integrations, we obtain the following expressions.

$$\begin{pmatrix} \bar{\omega}_\xi \\ \bar{\omega}_\varsigma \end{pmatrix}^T$$

$$= \begin{pmatrix} 2/3 \\ 1/6 \\ 1/6 \end{pmatrix}^T \begin{pmatrix} \omega_x(i,j) & \omega_z(i,j) \\ \omega_x(i+1,j+1) & \omega_z(i+1,j+1) \\ \omega_x(i+1,j) & \omega_z(i+1,j) \end{pmatrix} \begin{pmatrix} d_{\xi x} & d_{\varsigma x} \\ d_{\xi z} & d_{\varsigma z} \end{pmatrix} \tag{3.26}$$

Equations (3.23a)-(3.23c) can then be modified as

$$P_i = yQ_i \tag{3.27a}$$

$$R_i = -(x - \bar{\xi})Q_i \tag{3.27b}$$

$$S_i = (z - \bar{\zeta})Q_i \tag{3.27c}$$

where

$$Q_i = \frac{-S}{4\pi d^3}\left(\frac{2}{3} \quad \frac{1}{6} \quad \frac{1}{6}\right) \tag{3.28}$$

3.3. Flow Tangency Condition on Bound Vortex Panels

We consider a control point numbered as ni on a bound-vortex panel and write the flow-tangency condition of Eq. (3.5) in the form

$$\vec{V}_{induced}(ni) \cdot \vec{n}_s(ni) = -\vec{e}_\infty \cdot \vec{n}_s(ni) \tag{3.29}$$

where $\vec{V}_{induced}(ni)$ is the sum of the velocities induced by all the vortex panels.

$$\vec{V}_{induced}(ni) = \sum_{nj=1}^{NTOT} \vec{V}_p(ni, nj) \tag{3.30}$$

$$\vec{V}_p(ni,nj) = V_x(ni,nj)\vec{I} + V_y(ni,nj)\vec{J} + V_z(ni,nj)\vec{K} \tag{3.31}$$

$$\vec{n}_s(ni) = [d_{\eta x}\vec{I} + d_{\eta y}\vec{J} + d_{\eta z}\vec{K}]_{ni} \tag{3.32}$$

$$\begin{pmatrix} V_x \\ V_y \\ V_z \end{pmatrix}_{ni,nj} = \begin{pmatrix} d_{\xi x} & d_{\eta x} & d_{\varsigma x} \\ d_{\xi y} & d_{\eta y} & d_{\varsigma y} \\ d_{\xi z} & d_{\eta z} & d_{\varsigma z} \end{pmatrix}_{nj} \begin{pmatrix} V_\xi \\ V_\eta \\ V_\varsigma \end{pmatrix}_{ni,nj} \tag{3.33}$$

In Eq. (3.30). $\vec{V}_p(ni,nj)$ is the velocity induced at the nith control point by the njth vortex panel and NTOT represents the total number of bound and free vortex panels.

Use of Eqs. (3.30)-(3.33) and (3.20)-(3.22). reduces the LHS of Eq. (3.29) to

$$\sum_{nj=1}^{NTOT} \vec{V}_p(ni,nj)\cdot\vec{n}_s(ni)$$

$$= \sum_{nj=1}^{NTOT}\sum_{i=1}^{3} \begin{pmatrix} d_{\eta x} \\ d_{\eta y} \\ d_{\eta z} \end{pmatrix}_{ni}^{T} \begin{pmatrix} d_{\xi x} & d_{\eta x} & d_{\varsigma x} \\ d_{\xi y} & d_{\eta y} & d_{\varsigma y} \\ d_{\xi z} & d_{\eta z} & d_{\varsigma z} \end{pmatrix} \tag{3.34}$$

$$\begin{pmatrix} P_i d_{\varsigma x} & P_i d_{\varsigma z} \\ R_i d_{\xi x} + S_i d_{\varsigma x} & P_i d_{\xi z} + S_i d_{\varsigma z} \\ -P_i d_{\xi x} & -P_i d_{\xi z} \end{pmatrix} \begin{pmatrix} \omega_x(i) \\ \omega_y(i) \\ \omega_z(i) \end{pmatrix}_{nj}$$

and the RHS is given by

$$-\vec{e}_\infty\cdot\vec{n}_s(ni) = -\begin{pmatrix} cosx & -sinx & 0 \end{pmatrix}\begin{pmatrix} d_{\eta x} & d_{\eta y} & d_{\eta z} \end{pmatrix}_{ni}^{T} \tag{3.35}$$

3.4. Solenoidal Property of Vorticity

Since vorticity is the curl of the velocity vector field, it must be a solenoidal field. This condition, requiring that vorticity be conserved everywhere, is a computational condition which must be satisfied on all the vortex panels. On the bound vortex panels, this condition is enforced on each quadrilateral panel composed of two adjacent triangular panels by requiring that

$$\int\int \nabla \cdot \vec{\omega} ds = \oint \vec{\omega} \cdot \vec{n} d\ell = 0 \tag{3.36}$$

Substituting Eq. (3.19) into Eq. (3.36) and referring to Fig. 6, one can obtain the numerical expressions in terms of global nodal vorticities as follows

$$\sum_{k=1}^{4} [\triangle x(k)\omega_z(k) - \triangle z(k)\omega_x(k)] = 0 \tag{3.37}$$

where

$$\triangle x(1) = x(i, j+1) - x(i, j) \tag{3.38a}$$

$$\triangle z(1) = z(i, j+1) - z(i, j) \tag{3.38a}$$

$$\omega_x(1) = \frac{1}{2}[\omega_x(i, j) + \omega_x(i, j+1)] \tag{3.38c}$$

$$\omega_z(1) = \frac{1}{2}[\omega_z(i, j) + \omega_z(i, j+1)] \tag{3.38d}$$

3.5. Kutta Condition

The Kutta Condition, Eq. (3.5) requires that wing loading be zero at the edges of separation. This is satisfied when the velocity and vorticity vectors are parallel at the edges of separation. At a global node (i,j) this is given by [75]

$$\omega_x(i,j)V_z(i,j) - \omega_z(i,j)V_x(i,j) = 0 \tag{3.39}$$

since V_x and V_z are functions of the unknown global components of vorticity, Eq. (3.39) is a non-linear equation. To enforce this condition a linearized approach is adopted. Equation (3.39) is divided by $V(i,j)$ and letting

$$\frac{V_x(i,j)}{V(i,j)} = sin\beta(i,j) \tag{3.40a}$$

$$\frac{V_z(i,j)}{V(i,j)} = cos\beta(i,j) \tag{3.40b}$$

Equation (3.39) may be expressed as

$$\omega_x(i,j)cos\beta(i,j) - \omega_z(i,j)sin\beta(i,j) = 0 \tag{3.41}$$

The above equation becomes a linear equation if $\beta(i,j)$ is known. Starting with an initial guess, the angle $\beta(i,j)$ for any subsequent iteration step is calculated by Eq. (3.40) from the solution of the preceding iteration step.

3.6. Symmetry Condition

For symmetric flows, the component of vorticity parallel to the centerline must vanish at all points on the centerline. This condition is enforced by requiring the x-component of vorticity be zero at all nodes on the centerline.

3.7. Condition at the Wing Edges

Along the edges where the flow is attached, vortex shedding does not occur. Hence, it is required that there be no outflow of vorticity along such edges. This condition is enforced at all the nodes on these edges.

3.8. Conditions on the Free-Vortex Panels

The advantage with the present vortex panel method is that the nodal vorticity components of the free-vortex panels are no longer unknowns of the problem. Since we have assumed that all the vorticity shed from the edges is convected by the local velocity, the velocity components at the nodes of free vortex panels are determined by equating the outflow of vorticity from the bound vortex panels to its inflow into the free vortex panels along the edges of separation. A further simplification is achieved by aligning the local ς axis of the free vortex panel with the vorticity vector. This enables us to obtain the global nodal vorticity components of the bound vortex panels at the edges of separation. This is discussed in Appendix A.

The flow-tangency and force-free conditions, Eqs. (3.6) and (3.7), are enforced by aligning the local vorticity vector with the local velocity vector. Approximately,

the side 1-3 of each free vortex panel is aligned with the direction of the local velocity vector at the panel centroid. Typically, equations of the following type are used

$$x(i+1,j) = x(i,j) + \ell V_x/V \tag{3.42a}$$

$$y(i+1,j) = y(i,j) + \ell V_y/V \tag{3.42b}$$

$$z(i+1,j) = z(i,j) + \ell V_z/V \tag{3.42c}$$

where V is the magnitude of the velocity at the centroid of the panel and ℓ is the length of side $1-3$. The spiraling vortex sheet will be cut when it rolls up at least one full turn. The cut-off part will then be modelled by an isolated line vortex core which is connected to the remainder of the sheet by a feeding sheet.

3.9. Pressure and Force Calculations

The steady Bernoulli equation is used to calculate the pressure coefficient. For incompressible flow, the non-dimensional pressure coefficient is given by

$$C_p = \frac{p - p_\infty}{1/2\rho U_\infty^2} = 1 - \vec{V} \cdot \vec{V} \tag{3.43}$$

where $\vec{V}$ is the local velocity normalized with respect to the free stream speed. At a control point (i,j), on the upper surface of the wing, the pressure coefficient is defined by

$$C_{p_u}(i,j) = 1 - \vec{V}_u(i,j) \cdot \vec{V}_u(i,j) \tag{3.44}$$

where $\vec{V}_u(i,j)$ is the normalized velocity at the control point on the upper surface. At a corresponding point on the lower surface, the pressure coefficient is given by

$$C_{p_\ell}(i,j) = 1 - \vec{V}_\ell(i,j) \cdot \vec{V}_\ell(i,j) \tag{3.45}$$

where $\vec{V}_\ell(i,j)$ is the velocity at the control point on the lower surface. Since the lifting surface is approximated by a bound vortex sheet, we may write

$$\vec{V}_\ell(i,j) = \vec{V}(i,j) - \triangle\vec{V}(i,j) \tag{3.46a}$$

$$\vec{V}_u(i,j) = \vec{V}(i,j) + \triangle\vec{V}(i,j) \tag{3.46b}$$

where

$$\vec{V}(i,j) = \frac{\vec{V}_u(i,j) + \vec{V}_\ell(i,j)}{2} \tag{3.47a}$$

$$\triangle\vec{V}(i,j) = \frac{\vec{V}_u(i,j) - \vec{V}_\ell(i,j)}{2} \tag{3.47b}$$

Hence, the net pressure coefficient at the control point (i,j) is given by

$$\begin{aligned} \triangle C_p(i,j) &= C_{p_\ell}(i,j) - C_{p_u}(i,j) \\ &= 4\triangle\vec{V}(i,j) \cdot \vec{V} \\ &= 2(\vec{\omega}(i,j) \times \vec{n}) \cdot \vec{V}(i,j) \end{aligned} \tag{3.48}$$

where $\vec{n}$ is the unit normal at the control point on the upper surface. The normal force coefficient is also defined as

$$C_n = \frac{1}{A} \sum_{k=1} \triangle c_{p_k} \triangle A_k \tag{3.49}$$

where $\triangle A_k$ is the area of the kth panel, $\triangle C_{p_k}$ is the net pressure coefficient at its control point, and A is the area of the lifting surface.

Chapter 4

FORMULATION AND METHOD OF SOLUTION — COMPRESSIBLE FLOW

The formulation and the method of solution described here are based mainly on those used by Kandil [156] and by Kandil and Yates [2]. Since the purpose of this work is to demonstrate the shock-capturing capability of integral equation method, we will therefore concentrate our discussions on the shock-capturing technique. The shock-capturing approach used by Kandil and Yates [2] is modified by adding the technique of successive grid refinement (described in Section 5.4.) in order to reduce the computational time spent in the field compressibility calculations.

4.1. Formulation of the Problem

The governing equations for three-dimensional, steady, compressible, potential flow around a wing are given by

Conservation of mass

$$(\rho^{\cdot}\Phi^{\cdot}_{x^{\cdot}})_{x^{\cdot}} + (\rho^{\cdot}\Phi^{\cdot}_{y^{\cdot}})_{y^{\cdot}} + (\rho^{\cdot}\Phi^{\cdot}_{z^{\cdot}})_{z^{\cdot}} = 0 \tag{4.1}$$

Conservation of energy

$$a_\infty^{*2} + \frac{\gamma - 1}{2} V_\infty^{*2} = a^{*2} + \frac{\gamma - 1}{2}(u^{*2} + v^{*2} + w^{*2}) \tag{4.2}$$

Isentropic gas equation

$$\rho^* / \rho_\infty = (a^{*2} / a_\infty^{*2})^{1/(\gamma - 1)} \tag{4.3}$$

where Φ^* is the total velocity potential, a^* the speed of sound, ρ^* the density, γ the ratio of specific heats, and the subscript ∞ refers to the freestream condition. Combining Eqs. (4.2) and (4.3) and using $V_\infty^*, \rho_\infty^*$, and a length ℓ as the reference parameters, we obtain the following dimensionless equations:

$$\Phi_{xx} + \Phi_{yy} + \Phi_{zz} = G \tag{4.4}$$

$$\rho = \{1 + [(\gamma - 1)/2] M_\infty^2 (1 - u^2 - v^2 - w^2)\}^{\frac{1}{\gamma - 1}} \tag{4.5}$$

$$\begin{aligned} G &= -\frac{1}{\rho} \quad \vec{V} \cdot \nabla \rho \\ &= \frac{M_\infty^2}{2[1 + \frac{\gamma - 1}{2} M_\infty^2 (1 - V^2)]} \quad \vec{V} \cdot \nabla V^2 \end{aligned} \tag{4.6}$$

where M_∞ is the freestream Mach number; u, v and w are the velocity components of the total velocity $\vec{V}$, which is given by the Helmholtz decomposition

$$\vec{V} = \nabla \Phi + \vec{V}_{rot} \tag{4.7}$$

where $\vec{V}_{rot}$ is the solenoidal velocity due to the rotational flow. Note that Eq. (4.4) is obtained from the continuity equation using the solenoidal property of $\vec{V}_{rot}, \nabla \cdot \vec{V}_{rot} = 0$.

Treating Eq. (4.4) as a Poisson's equation and using Green's theorem, the solution to the equation is given by the sum of surface and volume integral terms, as well as the freestream velocity potential

$$\Phi_p(x,y,z) = \Phi_\infty + \frac{1}{4\pi}\int\int_s \frac{q}{r}ds + \frac{1}{4\pi}\int\int_{s,w} \mu\frac{\partial}{\partial n}(\frac{1}{r})ds + \frac{1}{4\pi}\int\int_\forall\int \frac{G}{r}d\forall \quad (4.8)$$

where $p(x,y,z)$ is a field point, Φ_∞ the velocity potential of freestream, q the strength of a source distribution on the boundary, μ the strength of a doublet distribution on the boundary, G a source distribution throughout the flowfield representing the compressibility of the flow, and r the distance between a field point $p(x,y,z)$ and a source or a doublet point(ξ,η,ς), given by

$$r = [(x-\xi)^2 + (y-\eta)^2 + (z-\varsigma)^2]^{\frac{1}{2}} \quad (4.9)$$

Taking the gradient of Eq. (4.8) and replacing the surface doublet term on the right-hand side by a surface vorticity term, we obtain the expression for the velocity field,

$$\begin{aligned}\vec{V}_p(x,y,z) =& \vec{e}_\infty - \frac{1}{4\pi}\int\int_s \frac{q}{r^2}\vec{e}_r ds + \frac{1}{4\pi}\int\int_s \frac{\vec{\omega}(\xi,\eta,\varsigma)\times\vec{r}}{r^3}ds \\ &+ \frac{1}{4\pi}\int\int_w \frac{\vec{\omega}(\xi,\eta,\varsigma)\times\vec{r}}{r^3}ds - \frac{1}{4\pi}\int\int_\forall\int \frac{G(\xi,\eta,\varsigma)}{r^2}\vec{e}_r d\forall\end{aligned} \quad (4.10)$$

where $\vec{e}_\infty$ is a unit vector in the freestream direction, and $\vec{\omega}$ the vorticity vector; the subscripts s and w refer to the wing and free-vortex sheet surfaces, respectively. For a zero-thickness wing, the second term on the right-hand side of Eq. (4.10) drops out. Note that the third term does not have to be a surface integral of vorticity since a surface integral of doublets can be used instead. The fourth term represents the contribution to the velocity field due to the free-vortex sheets emanating from the wing edges of separation. This term can also be read as $\vec{V}_{rot}$ since the vorticity in the field has been lumped into surface vorticity distributed on the free-vortex sheets. The last term is a volume integral term representing the linear and nonlinear compressibility in the flow.

Note that the integrand of the volume integral of Eq. (4.10) decreases rapidly with increasing distance from the wing/vortex system, not only because of the factor$(1/r^2)$ but also because G diminishes rapidly with increasing distance r. Consequently, for computational purposes, the volume integral needs to be addressed only within the immediate vicinity of the wing/vortex system. Boundary Conditions Eqs. (3.5)-(3.9) for the incompressible flow problem also apply to compressible flow problem. It should be noted that Eqs. (4.8) and (4.10) automatically satisfies the boundary condition at infinity which requires $\Phi_p \rightarrow \Phi_\infty$ at infinity. This is a substantial computational advantage over the finite difference technique, since one does not need to enforce this condition explicitly.

4.2. Discretization of Flow Field

The computational domain, due to compressibility effects, depends on M_∞ and the geometrical configuration of the wing flow and hence it is determined herein from a series of numerical experiments.

Once the computational domain is determined, we also need to discretize the flow field into small volume cells, in addition to the discretization of vortex sheets, in order to calculate the velocity induced by the flow compressibility. A rectangular-parallelopiped type of cell is chosen to be used throughout the flow field due to its simplicity in carrying out the volume integrals.

4.3. Velocity Field Induced by Flow Compressibility

Once the flow field is discretized into small volume cells, the velocity at any field point induced by the compressibility of any cell can be calculated.

4.3.1. Near-Field Expressions

The velocity $\vec{V}_p(x,y,z)$ at field point $p(x,y,z)$ induced by the flow compressibility of field volume $\forall$ is given by

$$\vec{V}_p(x,y,z) = -\frac{1}{4\pi}\int\int\int_{\forall}\frac{G(\xi,\eta,\varsigma)}{r^2}\vec{e}_r d\forall \tag{4.11}$$

Where $G(\xi,\eta,\varsigma)$, a source distribution over $\forall$, represents the flow compressibility.

For a rectangular-parallelopiped cell, Fig. 7, Eq. (4.11) can be rewritten as

$$\vec{V}_p(x,y,z) = -\frac{1}{4\pi}\int_{\varsigma_1}^{\varsigma_2}\int_{\eta_1}^{\eta_2}\int_{\xi_1}^{\xi_2}\frac{G(\xi,\eta,\varsigma)(A\vec{I}+B\vec{J}+C\vec{K})}{(A^2+B^2+C^2)^{3/2}}d\xi d\eta d\varsigma \tag{4.12}$$

where $A = x-\xi$, $B = y-\eta$, and $C = z-\varsigma$

For a constant G, the closed-form expression for the induced velocity is found to be

$$V_\xi = \vec{V}_p \cdot \vec{e}_\xi = \vec{V}_p \cdot \vec{I}$$
$$= \frac{G}{4\pi}\left\{\frac{-B}{2}\ell n\frac{H+C}{H-C} - \frac{C}{2}\ell n\frac{H+B}{H-B} + |A|sign(B)tan^{-1}\frac{|B|C}{|A|H}\right\}_{\xi_1,\eta_1,\varsigma_1}^{\xi_2,\eta_2,\varsigma_2} \quad (4.13a)$$

$$V_\eta = \vec{V}_p \cdot \vec{e}_\eta = \vec{V}_p \cdot \vec{J}$$
$$= \frac{G}{4\pi}\left\{\frac{-C}{2}\ell n\frac{H+A}{H-A} - \frac{A}{2}\ell n\frac{H+C}{H-C} + |B|sign(C)tan^{-1}\frac{|C|A}{|B|H}\right\}_{\xi_1,\eta_1,\varsigma_1}^{\xi_2,\eta_2,\varsigma_2} \quad (4.13b)$$

$$V_\varsigma = \vec{V}_p \cdot \vec{e}_\varsigma = \vec{V}_p \cdot \vec{K}$$
$$= \frac{G}{4\pi}\left\{\frac{-A}{2}\ell n\frac{H+B}{H-B} - \frac{B}{2}\ell n\frac{H+A}{H-A} + |C|sign(A)tan^{-1}\frac{|A|B}{|C|H}\right\}_{\xi_1,\eta_1,\varsigma_1}^{\xi_2,\eta_2,\varsigma_2} \quad (4.13c)$$

where $H = (A^2 + B^2 + C^2)^{1/2}$

4.3.2. Far-Field Expressions

As stated before, the integrand of Eq. (4.11) decrease rapidly with increasing distance r because of the factor $(1/r^2)$. As a matter of fact, when r is large, the volume cell can be treated as a point source located at the center of the volume cell with a strength of $G\forall$. Therefore, Eq. (4.11) reduces to

$$\vec{V}_p(x,y,z) = \frac{-G\forall}{4\pi}\left[\frac{(x-\bar{\xi})\vec{I} + (y-\bar{\eta})\vec{J} + (z-\bar{\varsigma})\vec{K}}{\bar{r}^3}\right] \quad (4.14)$$

where $(\bar{\xi},\bar{\eta},\bar{\varsigma})$ are the coordinates of center of volume $\forall$ and

$$\bar{r} = [(x-\bar{\xi})^2 + (y-\bar{\eta})^2 + (z-\bar{\zeta})^2]^{1/2}$$

4.4. Solution Procedure

Two loops are required to solve the nonlinear full potential equation iteratively. The inner loop is used to calculate and check the convergence of the nonlinear compressibility term, G, while the outer loop updates and checks the convergence of wake shape and vorticity distribution. The solution procedure steps are as follows:

Step 1. Solve the incompressible flow for the vorticities of bounded and free vortex panels.

Step 2. Calculate the velocities at the centers of all volume cells through Eq. (4.10). Initially, the effect of field compressibility is neglected, i.e. the value of G in Eq. (4.10) is initialized as zero.

Step 3. Iteratively calculate G at the center of each cell from Eq. (4.6) with $\nabla\rho$ obtained with the Murman - Cole type - dependent finite difference schemes until G converges (this usually takes 2 or 3 iterations).

Step 4. Update the boundary conditions through the velocity calculations from Eq. (4.10) with influence from both the vorticity term and the nonlinear compressibility term.

Step 5. Solve for new vorticities and iteratively update the wake shape by satisfying free vortex panel boundary conditions until the wake shape converges.

Step 6. Calculate and check the convergence of the pressure coefficient and local Mach number on each control point.

Repeat steps 2 through 6 until the wake shape and G values are converged. The under-relaxation factor (usually 0.4 to 0.6) was used when updating the wake shape, no relaxation was used for calculating G. The pressure coefficient is then calculated through

$$C_p = \frac{2}{\gamma M_\infty^2}\{[1 + \frac{\gamma - 1}{2} M_\infty^2 (1 - V^2)]^{\frac{\gamma}{(\gamma-1)}} - 1\} \tag{4.15}$$

Chapter 5

COMPUTER CODES AND NUMERICAL EXAMPLES

5.1. Development of computer codes

Two computer codes have been developed to implement the methods of solution described in Chapters 3 and 4. The first program solves the incompressible vortical flow using the panel technique. It is also used to study on how to convert the integral equation method code to a high degree of vectorized code in order to compete with the computational efficiency of the finite difference method codes when run on modern vector computers. The study is detailed in Appendix B. The second program is mainly an extension of the first program to compressible flows by adding the flow-compressibility along with the type difference schemes for shock capturing.

The main purpose of this research was to demonstrate that the integral equation method is capable of capturing shocks in three-dimensional transonic-vortex flows. In order to save execution time, we limit the test cases, without losing the generality of applications of this method, to rectangular flat wing flows which possess all fundamental characteristics of transonic vortex flow.

The first program has several improved features over that used in References 73-75 and 53. Two of those features are important to the successful implementation of the methodology described in Chapter 3. First, the resulting equation set

is carefully selected to be an exact set which ensures that some important boundary conditions are satisfied "exactly" rather than "in a least square sense" as in an overdetermined equation set. This is crucial to the successful convergence for solving the vortical flow problem. The results of the numerical experiments have shown that a minor change in some of those boundary conditions, e.g., the Kutta condition along the edges of separation, could cause an appreciable change in the solution. They have also shown that the exact equation set has better numerical stability and convergence rate than the overdetermined equation set. Second, the solenoidal property of vorticity is implemented in an integral form rather than in a finite difference form, i.e., using the conservation of vorticity outflow for each quadrilateral panel instead of finite differencing the global nodal vorticities at each node. Numerical experiments showed that the integral form is easier to implement for complex configurations and requires a small number of panels to maintain a high degree of accuracy.

The second program has also an improved feature over that used in Reference 2. In this program, the velocity coefficients induced by field compressibility among volume cells are pre-calculated (in a separate computer program – a preprocessor), stored and retrieved from memory when needed rather than calculated inside the program. This reduces tremendously the computational time with a reasonable memory requirement. Moreover, it provides an easy approach for vectorization of field compressibility calculations which take a major portion of computational time (in general, about 90 percent in a two dimensional case, 50 percent/80 percent in a three dimensional case with/without pre-calculated velocity coefficients). Both computational efficiency and accuracy can be improved further if combined with a successive grid refinement technique which will be discussed in Section 5.4.

In the following two sections, we will show various numerical experiments and examples to support the previously described methodology. The first section will show some preliminary systematic numerical experiments to analyze the accuracy, stability and convergence of the computer program due to changes of some parameters, such as the paneling distribution, switching distance for far-field approximation, relaxation factor for wake adjustments, and the number of wake adjustments between two iterations. The second section shows the numerical results of several test cases for transonic flow problems to demonstrate the capabilities of this method.

5.2. Preliminary Systematic Numerical Experiments

One of the characteristics of this method for solving vortex flow problems is the efficient way it treats the time consuming near-field calculations and the computationally efficient far-field calculations. The distance at which the near-field calculation is switched to the far-field calculation is determined from numerical experiments. In the far-field approximation used here, we assume the distributed vortex panel is a uniformly distributed one rather than two concentrated vortex lines as used in References 73-75. The strength of this uniformly distributed vortex panel is obtained by averaging the original distributed strength as expressed in Eq. (3.25). The former approximation, as shown in Eq. (3.24), is free of numerical singularities while the latter needs to be handled carefully due to its high degree of geometric dependence in the calculations. Tables 1 and 2 compare these two approximations with the closed form calculations. The results show that the uniformly distributed vortex panel approximation is less sensitive to the panel shape and to the location of the field point, which is crucial to the stability and accuracy of solution to the problems with complex configurations.

The distance at which the near-field calculations is switched to far-field approximation for compressibility calculations is also determined numerically. Table 3 compares the far-field approximation with the closed form calculations. When switching distance is selected as three times the panel length, the agreement for both calculations is up to three significant figures and is always up to at least the third decimal point. The values for G, Eq. (4.14), are close to unit when near the shock and are much less than one when away from the shock. The difference in induced velocity is limited consequently to the third decimal point which is usually within less than one percent. Numerical results showed that the difference in pressure coefficients is less than three percent when the switching distance is 3 for a rectangular wing with a root chord length of 10.

Several test runs for incompressible vortical flow have been performed for two purposes: first, to check if the program functions normally in solving vortex flow problems, and second, as mentioned earlier, to analyze the data dependence for each module in order to perform the vectorization of the program.

Figures 8 and 9 show the comparisons of the chordwise variation of lifting pressures for a rectangular wing with aspect ratio of 3, at 50 percent and 70 percent span stations, respectively, with those of Reference [53] and with the experimental data of Lessing et al. [173]. The computational results match well with the experimental results at the low subsonic speed range varifying that this program functions normally.

A long existing argument for the integral equation method is that the solution obtained from many existing computer programs is not consistent when the wing paneling changes. We have performed a series of numerical experiments to examine the consistency of solutions vs wing paneling. Figures 10 and 11 show both the

chordwise and the spanwise distributions of section circulation for rectangular wing with different aspect ratio and paneling. The two figures and the numerical results show that the distribution of x-direction circulation does not appear to be affected by the wing paneling and the distribution of z-direction circulation is slightly affected only in the region near wing tip. However, the wing paneling does affect both the x- and z-directional vorticity distributions (which determine the solution of the problem) in the regions near wing edges. In general, for a wing with a reasonable number of panels, as long as the paneling and locations of control points in highly variant regions, e.g. the regions near wing edges, are the same, the solutions will be consistent. Further investigations of the consistency of solutions vs wing paneling for more complicated flow problems are also underway.

Figures 12-14 show the wake shapes at different iteration stages. One can see from the results that the wake convergence of the vortical flow region is very sensitive to the panel geometry, e.g., panel shape and panel length. For example, the ratio of panel width to panel length of Figure 12 is 0.75 and that of Figure 14 is 0.4: the solution of the former case converged in about 5 outer iterations (Figure 13) while the solution of the latter case blew up after 4 outer iterations (Stage 3 of Figure 14).

The wake panels near the vortex core deform substantially in the downstream direction, as can be seen in the figures. This will introduce instability in the flow, which might cause the blow-up of the solution (Figure 14). Two methods may be used to remedy this problem. First, one can divide the wake into several segments (Figure 13) to allow more flexibility when adjusted, and each segment may have different panel widths. Thus, the wake adjustment can be performed for each segment separately and successively as far downstream as needed. The second method

which is more efficient computationally, is used when the wake adjustment reaches a certain stage, e.g., at stage 1 of Figure 14, one can subdivide each of those wake panels, whose widths have become large, into two or more smaller panels and iterations continue. This process can be repeated if necessary until the required accuracy is reached. In both methods, the panel width is determined in a way that the conservation of circulation is not violated.

In all the test cases, the wake shape downstream of the last row panels was modeled as a semi-infinity cylindrical surface with cross section same as that of the last row panels. It should be noted here that the models of the vortex core and the feeding sheet (described in Section 2.2) used by many researchers [22,51,58] can be incorporated into the present method, although it was not done for the current test cases.

5.3. Numerical Examples of Subcritical and Supercritical Flows

After all modules of the program were tested and all programming parameters checked, the program was used for running complete cases. The results of test cases shown here are for rectangular wings with aspect ratios of 2, at angles of attack of 5 and 10 degrees respectively, and free stream Mach number ranges from 0.3 to 0.8. Referring to Figure 7, the half span of the wing and wake is divided into 10 by 6 and 10 by 10 quadrilateral panels respectively, and each quadrilateral panel consists of two triangular panels. One half of the computational volume for symmetrical flows is defined as 50 percent of the root chord ahead of the leading edge and 80 percent of the root chord after the trailing edge in the x-direction; 50 percent of the root chord above the wing and 25 percent of the root chord under the wing in the y-direction;

50 percent of the half span outboard of the side edge in the z direction; and is divided into 23 by 9 by 9 volume cells respectively for the coarse grid calculations. The grid sizes are 1/10 of the root chord in the x-direction, 1/12 of the root chord in y-direction and 1/6 of the half span in the z-direction.

The problem is solved using two iteration loops; vorticity distribution and wake shape are iterated through an outer loop while the field compressibility is iterated through an inner loop. The solution is obtained when both results converge.

A separate program is used to calculate the compressibility induced velocity between any two volume cells. The calculations are done with the method of images of a field point. therefore, the calculated velocity components can be stored in a array of dimension of (23,9,9,8) instead of a dimension of (23,9,9) by (23,9,9). Those induced velocity coefficients will then be retrieved from memory rather than calculated inside the program. This process saves about thirty percent of the total computational time.

Figures 15-21 show the computational results for a wing with an aspect ratio of 2, at a 10 degree angle of attack and with $M_\infty = 0.7$. Figures 15 and 19 show the chordwise and spanwise distributions of compressibility G and local Mach number, M_ℓ, respectively. From the figures, we can see that the magnitude of G drops rapidly to near zero with increasing distance from shock despite the smearing of G value in the shock region. The local Mach number also approaches to free stream Mach number when away from shock region. These results provide us the information that, due to the fast decay of the effect of compressibility with increasing distance from shock, we can narrow down the original computational domain for compressibility calculations to the extent where the effect of compressibility is negligible.

For example, in Figure 15, the G value drops down to near zero at 15 percent of root chord ahead of the leading edge (marked as point A) and at 50 percent of the root chord after the leading edge (point B). Similarly, the G value drops down to near zero at 15 percent of the half span outboard of the side edge (point C of Figure 19), and at about 40 percent of the root chord above and 20 percent of the chord under the wing planform, respectively. With this information, a small but effective computational domain is defined and a fine grid is used within this domain.

The grid refinement produces improved resolution of the flow properties, e.g., G value, local Mach number, pressure coefficient, etc., in the shock region. The grid refinement can also be performed successively in the region where the value of G is large until the required accuracy is reached. This type of successive grid refinements, which starts from a coarse grid for a large computational domain to a fine grid for a small but effective computational domain, can capture the shock accurately and efficiently.

The accuracy and efficiency can be improved further if the Prandtl-Glauert operator is used on the ieft hand side of Eq. (4.4). With this modification, the linear part of compressibility will appear in the surface integral rather than in the volume integral. The non-linear part of compressibility will only appear in the volume integral and hence the computational domain will be reduced substantially. The size of the computational volume may also be reduced by extending the volume integration outward from the body only until the magnitude of integrand falls below a pre-selected threshold value.

Figures 16-18 show the distributions of G value and local Mach number, M_ℓ, at different iteration stages. From these figures, we can see that both values are almost converging after two outer loop and two inner loop iterations. Here, G values

are fixed everywhere for each outer loop, while both vorticity and wake shape are fixed for each inner loop. Also by inspection of the results, one finds that both values converge at the third inner loop iteration (five is used in test runs). These tell us how fast the solution converges for the panel method and also provide us with the information on how to arrange the iteration numbers for both inner and outer loops. As a matter of fact, it is unnecessary to perform the grid refinement when the solution has converged. In most of the cases tested, the trend of the distribution of G value is very clear and stable after two to three outer iterations, the computational domain can then be narrowed down and the grid refinement performed.

Figure 20 shows the chordwise variation of pressure coefficients of the upper and lower surfaces at different iteration stages. The shock location can not be determined easily from the pressure coefficient distribution on the upper surface due to the coarse grid size but can be determined easily from the distribution of local Mach number on the upper surface. In general, under the potential flow assumption, for flow with weak shocks, the shock location is on the local sonic line where the value of G changes rapidly, i.e., near the region where the flow leaves the supersonic region into the subsonic region. From this figure, the rapid convergence of pressure coefficient distribution is obvious.

Figure 21 shows the chordwise distributions of pressure coefficient for wing flows at 10 degree angle of attack with different free stream Mach numbers. From the figure, we can see the influence of the free stream Mach number on the pressure coefficient distribution which is significant only in forward upper surface. At 10 degree angle of attack, the shock occurs when the free stream Mach number approaches 0.6. On lower surface, the local Mach number is small and the pressure

coefficient distribution is affected little by the variation of the free stream Mach number for these applications.

Figures 22-26 show the numerical results for the case of $M_\infty = 0.8$ and at an angle of attack of 5 degree. The similarity of these two cases can be easily seen by comparing them. The shock strength of this case is weaker than that of the previous one, this reflects the distribution of G and consequently the selection of the computational domain. Comparing the G-distributions of Figure 22 and Figure 15, we can easily identify the differences of the locations of points A and B. In general, for similar wing flows, the weaker the shock, the closer the locations of points A and B to the shock. Similar conclusions can be drawn in the spanwise direction from the comparison of Figure 24 and Figure 19. The location of point C in Figure 24 is closer to the side edge than that is of Figure 19.

Figure 25 also shows the spanwise variation of local Mach number, M_ℓ, and G, from which, one can see that G approaches zero even inboard of the wing edges. However, this kind of distribution cannot be used as a reference for reducing the computational domain since the vorticity distribution of the region near wing tip is highly varying. Figure 26 shows the chordwise distribution of pressure coefficient for wing flows at 5 degree angle of attack at different free stream Mach numbers. The large change of the pressure coefficient distribution starts when the free stream Mach number reaches 0.85 where the local Mach number in the supersonic pocket reaches 1.3.

Figures 27-29 show the numerical results of the scheme with local grid refinement. The test case is that of a flow over a rectangular wing of aspect ratio 2.0, at 10 degree of angle of attack, and with free stream Mach number of 0.6. The original computational domain and grid size were described previously. After obtaining the

solution from the coarse grid, we define the new computational domain as 25 percent of root chord ahead of the leading edge (point A of Figure 27), and 50 percent of root chord after the leading edge (point B of Figure 27), and 12.5 percent of half span outboard of the side edge (point C of Figure 28). Three different grid sizes are used, namely, medium grid (MG), fine grid (FG), and very fine grid (VFG). The grid sizes for MG, FG and VFG in the x-direction are 1/20, 1/30 and 1/40 of the chord, respectively. The grid sizes in the y- and z-direction are 1/12 of the chord and 1/8 of the half span respectively for all three cases.

Figure 27 shows the comparison of the chordwise distributions of G and local Mach number, M_l. As expected, when the grid size becomes finer the distributions of both values become sharper and stronger, and the shock region also becomes narrower. The newly calculated values of both G and local Mach number drop asymptotically to zero even faster and match the old values at the boundary of the new computational domain. These results show explicitly that this technique is feasible, efficient and capable of capturing sharp shock waves.

For flow with weak shocks, the location at which the G value changes sign coincides with the peak of the local Mach number distribution, since, for a potential flow, G is proportional to the derivative of the square of the local Mach number, Eq.(4.6). The shock location can be determinated from the local Mach number distribution on the upper surface which is close to the negative peak point of G. This is true for flows with weak shocks and is shown in Figure 27.

Figure 28 shows the spanwise distributions of G and local Mach number. The differences of both distribution curves with the old ones are due to the change of grid size, but both the newly calculated values match well with the old values at boundaries. This again ensures the accuracy and the efficiency of this technique.

Figures 27 and 28 also show that the distributions of G and local Mach number in both spanwise and chordwise directions converge asymtotically in the shock region when grid size becomes finer except at shock where the G value still not quite converged yet (Figure 27). But, from the trend of G distribution, it is believed that the G distribution should converge rapidly as the grid refinement continues.

Figure 29 shows the chordwise distributions of surface pressure coefficient and the local Mach number on the upper surface for all cases. As we can see the fine grid refinement improves the sharpness of the pressure coefficient distribution curve in the shock region and change little in the local Mach number distribution. Both distributions, which are more interesting to the aerodynamicists, converge asymtotically in a faster rate comparable to the G distribution as grid size becomes finer.

Chapter 6

CONCLUSIONS AND RECOMMENDATIONS

6.1. Concluding Remarks

An integral equation method for solving the full potential equaton for three dimensional transonic vortex flows has been developed. This method is capable of capturing shock waves and is also capable of predicting force-free wake shapes. The capabilities of this method were demonstrated through applications to three-dimensional transonic vortex flows.

Reading the full potential equation as Poisson's equation, the solution for the velocity field has been expressed in terms of an integral equation using Green's theorem. The solution consists of a surface integral of the vorticity distribution on the wing and its free-vortex sheets and a volume integral of source distribution within a computational region around the flow domain under consideration. The solution was obtained through successive iterations.

The bound- and free-vortex sheets were modeled using a distribution of bilinear vortex panels which are equivalent mathematically to quadratic doublet panels. The distributed vortex panel model has demonstrated its numerical stability and the results are less dependent on panel geometry than for vortex lattice methods.

The source distribution, which depends on the density gradient, varies with the free stream Mach number, M_∞, the angle of attack, α, and the geometrical configuration of the wing flow, and is generally a smooth function if the flow domain is shock free. Mathematically, when a shock wave exists in the flow, the source distribution (and the pressure distribution) must have a discontinuity at the shock. Computationally, the source distribution and the pressure changes rapidly in that region. By tracking the variation of either the source distribution or the pressure distribution during the computational iterations, one can easily capture the shock in the flow.

Since we are dealing with mixed type equations, the density gradient is obtained by the Murman-Cole type of difference scheme to ensure the proper computational modeling of wave propagation. The difference scheme used here is not fully conservative. The drawback of this type of scheme has been discussed in Chapter 2. In finite difference methods, many fully conservative schemes have been developed in order to satisfy the jump conditions across the shock. The grid size must be refined in regions of rapid changes of the flow properties, in order to resolve accurately these regions which include shock waves. Although such a fine grid will increase the computational time per iteration in finite difference schemes, it is extremely expensive for integral equation methods. To remedy this, the technique of successive grid refinement (described and numerically demonstrated in Section 5.4.) and/or the shock-fitting technique are recommended.

The numerical results show that this method is capable of capturing shock waves and converges within a number of iterations that is at least two orders of magnitude less than finite difference schemes. For example, the cases computed in Section 5.4. are flow around a rectangular wing of $AR = 2.0$, at 5 and 10 degree

angles of attack, respectively, and with the free stream Mach number varying from 0.3 to 0.8. Two step sizes were used: a 1/10 root chord length for the coarse grid cases, and a 1/30 root chord length for the fine grid cases. The computational domains are discretized into 23 × 9 × 18 volume cells for all cases.

The solutions for the coarse grid cases converge within 3 outer iterations and 2-3 inner iterations for each of the outer iterations. By examining the distribution of G through the flow domain, one can locate the shock region, and consequently the original computational domain can be reduced. Once the new computational domain is defined , a fine grid is used and the problem is solved through the same iteration technique. The fine grid solutions converge at around 4 to 5 outer iterations and 3 to 5 inner iterations for each of the outer iterations. The shocks can easily be captured in the fine grid solutions. The results of these numerical experiments demonstrate conclusively that this methodology can be extended to complex flow applications.

One of the fundamental characteristics of the integral equation method is its automatic satisfaction of the far field boundary condition. Moreover, the disturbances due to compressibility diminish more rapidly than the inverse square of the distance from the source of the disturbance to the field point. As a result of this mathematical property, a small computational domain can be used. It has been shown that the dimensions of the computational domain for the coarse grid cases are already one order of magnitude less than those of the finite difference method. The dimensions of the reduced computational domain for the fine grid are even smaller.

One of the drawbacks of the finite difference method is its lack of flexibility in dealing with flows with complicated configurations due to the difficulties encountered in grid generation. For complicated configurations, it is believed that the

integral equation method should perform better than the finite difference method due to its geometrical flexibility in discretization of the boundaries.

From the numerical results, the coarse grid solutions, in general, converge faster than the fine grid solutions. But for some weak shock flows, the fine grid solutions converge even faster than those cases of coarse grid. More numerical studies should help to understand the effect of the shock strength and the grid size on the behavior of the solution.

From the results of numerical experiments, we conclude that the integral equation method appears more stable and converges faster than the finite difference method when solving transonic wing flows with weak shocks. Due to its stable behavior which has been demonstrated, we also conclude that the integral equation method can be extended to unsteady flows. Two-dimensional unsteady flow solutions have been already demonstrated by Hu [174].

6.2. Recommendations

In general, the solution may be obtained by repeatedly using the successive local grid refinement until the required accuracy is reached, but this might not be computationally efficient.

Alternatively, the shock-fitting technique should be applied after the shock location is obtained approximately by using a coarse grid for shock capturing. Solutions of this type were obtained by Kandil & Hu [167,168] for two-dimensional flow applications. This will alleviate the possible dissipation problems near the shock and possible shock-jump-condition problems which might be caused by the difference scheme. Shock-fitting also provides a convenient mechanism for accounting for

the shock generated entropy in a natural way. From the above discussions, a best combination of the two techniques is recommended: use the successive local grid refinement technique for two or three times to obtain a good initial guess of shock location and then apply the shock-fitting technique to obtain the final solution. An attempt to combine these two techniques is underway.

The accuracy and computational efficiency can be improved further by using the Prandtl-Glauert operator instead of the Laplace operator for solving the vortical flow problem. With this modification, the linear part of compressibility will appear in the surface integral rather than in the volume integral. The non-linear part of compressibility will only appear in the volume integral and hence the computational domain will be reduced substantially. The size of the computational volume may also be reduced by extending the volume integration outward from the wing surfaces only until the magnitude of integrand falls below a selected threshold value.

As mentioned earlier, the current methodology is applied to solving transonic vortex flows with weak shocks, nevertheless, this technique can be modified to solve flows with strong shocks. This includes taking account of entropy changes on crossing the shock. The boundary conditions must be modified as well.

The combination of segmentation and re-paneling (described in Section 5.2.) is also recommendated in order to obtain an accurate wake shape efficiently which is crucial for many aerodynamic configurations, e.g., the canard wing, wing-tail interaction, and helicopter etc.

In order to simulate the flow field outside the core the spiraling vortex sheet is necessarily cut at some angular extent (usually, at least one full turn). It is

recommended that the cut-off part be modelled by an isolated line-vortex core connected by a feeding sheet to the remainder of the sheet. The feeding sheet transfers vorticity from the spiraling sheet into the vortex core as it travels downstream.

Some efforts were also spent to study the data dependency of DO loops in the computer program in order to improve the vectorization of the program and hence the computational efficiency when running on a vector computer. The study has shed some light on how to perform the vectorization of the computer program of an integral equation method and a numerical attempt is also underway.

REFERENCES

1. Bradley, R. G. and Bhateley, I. C., "Computational Aerodynamic Design of Fighter Aircraft–Progress and Pitfalls," AIAA Paper 83-2063, Aug. 1983.

2. Kandil, O. A. and Yates, E. C., Jr., "Computation of Transonic Vortex Flows Past Delta Wings-Integral Equation Approach," AIAA Paper 85-1582, July 1985. Also in AIAA Journal, Vol. 24, No. 11, November 1986, pp. 1729-1736.

3. Peckham, D. H., "Low-Speed Wind-Tunnel Tests on a Series of Uncambered Slender Pointed Wings with Sharp Edges," British ARC R & M No. 3186, December 1958.

4. Earnshaw, P. B., "An Experimental Investigation of the Structure of a Leading-Edge Vortex," ARC R & M No. 3281, 1962.

5. Wentz, W. H. and McMahon, M. C., "An Experimental Investigation of the Flow Fields about Delta and Double-Delta Wings at Low Speeds," NASA CR 521, 1966.

6. Fink, P. T. and Taylor, J., "Some Early Experiments on Vortex Separation," ARC R & M No. 3489, 1967.

7. Hummel, D., "Study of Flow Around Sharp-Edged Slender Delta Wings with Large Angles of Attack," NASA TT F-15, 107, September 1973.

8. Wentz, W. H., "Effects of Leading-Edge Camber on Low-Speed Characteristics of Slender Delta Wings," NASA CR-2002, 1972.

9. Hummel, D., "On the Vortex Formation over a Slender Wing at Large Incidence," AGARD-CP-247, 1979, Paper 15.

10. Vehaagen, N. G., "An Experimental Investigation of the Vortex Flow over Delta and Double-Delta Wings at Low Speeds," AGARD-CP-342, 1983, Paper 7.

11. Maskell, E. C., "Flow Separation in Three Dimensions," British RAE Report No. Aero 2565, November 1955.

12. Kandil, O. A., "Numerical Prediction of Vortex Cores from the Leading and Trailing Edges of Delta Wings," ICAS paper No. 14.2., Oct. 1980.

13. Lambourne, N. C. and Bryer, D. W., "The Bursting of Leading Edge Vortices; Some Observations and Discussion of the Phenomenon," ARC, R & M 3282, 1962.

14. Lowson, M. V., "Some Experiments with Vortex Breakdown," Journal of the Royal Aeronautical Society, Vol. 68, 1964. pp. 343-346.

15. Peckham, D. H. and Atkinson, S. A., "Preliminary Results of Low Speed Wind Tunnel Tests on a Gothic Wing of Aspect Ratio 1," ARC, CP 508, 1957.

16. Hummel, D. and Srinivasan, P. S., "Vortex Breakdown Effects on the Low-Speed Aerodynamic Characteristics of Slender Delta Wings in Symmetrical Flow," Journal of the Royal Aeronautical Society, Vol. 71, April 1967, pp. 319-322.

17. Maskell, E. C., "Some Recent Developments in the Study of Edge Vortices," Proceedings of 3rd Congress of International Council of Aerospace Science. 1962, Spartan Books, Inc., Washington 1964, pp. 737-749.

18. Stanbrook, A. and Squire, L. C., "Possible Types of Flow at Swept Leading Edges," Aeronautical Quarterly, Vol. XV, February 1964.

19. Szodruch, J. and Ganzer, U., "On the Lee-Side Flow for Slender Delta Wings at High Angle of Attack," AGARD-CP-247, 1979, Paper 21.

20. Vorropoulos, G. and Wendt, J. F., "Laser Velocimetry Study of Compressibility Effects on the Flow Field of a Delta Wing," AGARD-CP-342, 1983, Paper 9.

21. Miller, D. S. and Wood, R. M., "An Investigation of Wing Leading-Edge Vortices at Supersonic Speeds," AIAA Paper 83-1816, 1983.

22. Hoeijmakers, H. W. M., "Methods for Numerical Simulation of Leading Edge Vortex Flow," Proceedings of the Symposium on Vortex Dominated Flow, NASA, LRC, July, 1985.

23. Polhamus, E. C., "A Concept of the Vortex Lift of Sharp-Edged Delta Wings Based on a Leading-Edge Suction Analogy," NASA TN D-3767, 1966.

24. Polhamus, E. C., "Application of the Leading Edge Suction Analogy of Vortex Lift to the Drag Due to Lift of Sharp Edge Delta Wings," NASA-TN-D-4739, August 1968.

25. Polhamus, E. C., "Predictions of Vortex Lift Characteristics by a Leading Edge Suction Analogy," Journal of Aircraft, Vol. 8, No. 4, April 1971, pp. 193-199.

26. Ashley, H. and Landahl, M. T., "Aerodynamics of Wings and Bodies," Adison-Wesley Publ. Co. Inc., 1965.

27. Lamar, J. E., "Analysis and Design of Strake-Wing Configurations," Journal of Aircraft, Vol. 17, No. 1, 1980, pp. 20-27.

28. Legendre, R., "Flow in the Neighborhood of the Apex of a Highly Swept Wing at Moderate Incidences," Aeronautical Research Council, Report No. 16796, 1954.

29. Adams, M. C., "Leading Edge Separation from Delta Wings at Supersonic Speeds," Journal of the Aeronautical Sciences, Vol. 20, No. 6, June 1953, p. 430.

30. Edwards, R. H., "Leading Edge Separation from Delta Wings," Journal of the Aeronautical Sciences, Vol. 21, No. 2, February 1954, pp. 134-135.

31. Brown C. E., Michael, W. H., "Effect of Leading-Edge Separation on the Lift of a Delta Wing," Journal of the Aeronautical Sciences, Vol. 21, 1954, pp. 690-694.

32. Brown, C. E. and Michael, W. H., "On Slender Delta Wings with Leading Edge Separation," NACA-TN-3430, 1955.

33. Mangler, K. W., Smith, J. H. B., "A Theory of the Flow past a Slender Delta Wing with Leading-Edge Separation," Proc. Roy. Soc. A, Vol. 251, 1959, pp. 200-217.

34. Smith, J. H. B., "Improved Calculations of Leading-Edge Separation from Slender, Thin, Delta Wings," Proc. Roy. Soc. London, A 306, 1968,pp. 67-90; also in RAE TR 66070, 1966.

35. Clark, R. W., "Non-Conical Flow past Slender Wings with Leading-Edge Vortex Sheets," RAE TR 76037, 76.

36. Falkner, V. M., "The Solution of Lifting Plane Problems by Vortex-Lattice Theory," Aeronautical Research Council, Reports and Memorandum No. 2591, September 1947.

37. Belotserkovskii, S. M., "Calculation of the Flow Around Wings of Arbitrary Planforms Over a Wide Range of Angles of Attack," NASA TT F-12, 391, 1969.

38. Rehbach, C., "Calculation of Flow Around Zero-Thickness Wings with Evolute Vortex Sheets," NASA TT F-15, 183, 1973.

39. Kandil, O. A., "Prediction of the Steady Aerodynamic Loads on Lifting Surfaces Having Sharp-Edge Separation," Ph.D. Dissertation, Department of Engineering Science and Mechanics, Virginia Polytechnic Institute and State University, December 1974.

40. Rehbach, C., "Numerical Investigation of Vortex Sheets Issuing from Separation Line Near the Leading Edge," NASA TT F-15, 530, 1974.

41. Kandil, O. A., Mook, D. T., and Nayfeh, A.H., "Nonlinear Prediction of the Aerodynamic Loads on Lifting Surfaces," Journal of Aircraft, Vol. 13, No. 1, January 1976, pp. 27-28.

42. Kandil, O. A., Mook, D. T., and Nayfeh, A.H., "A Numerical Technique for Computing Subsonic Flow Past Three Dimensional Separation," AIAA paper No. 77-1, January 1977.

43. Kandil, O. A., Atta, E. H., and Nayfeh, A. H., "Three Dimensional Steady and Unsteady Asymmetric Flow Past Wings of Arbitrary Planforms," AGARD CP-227, February 1978. Also NASA CR 145 235, September 1977.

44. Kandil, O. A., "Asymmetric Flow Past Wings at Large Incidence with Small Amplitude Oscillations," AIAA paper No. 78-1336, August 1978.

45. Kandil, O. A., "A Nonlinear Discrete-Vortex-Perturbation Method for the Unsteady Lifting-Surface Problems with Edge Separations," 11th Congress of ICAS, Lisbon, Portugal, September 1978.

46. Kandil, O. A., "State of the Art of Nonlinear Discrete-Vortex Methods for Steady and Unsteady High Angle of Attack Aerodynamics," AGARD CP-247, January 1979.

47. Belotserkovskii, S. M. and Nisht, M. I.,"Non Stationary Nonlinear Theory of a Thin Wing of Arbitrary Planform," Mekhanika Zhidkosti Gasa, No. 4, 1974, pp. 100-108.

48. Rom, J., Almosnino, D. and Zorea, C., "Calculation of the Nonlinear Aerodynamic Coefficients of Wings of Various Shapes and their Wakes Including Canard Configurations," 11th Congress of ICAS, Lisbon, Portugal, September 1978.

49. Zorea, C. R. and Rom, J., "The Calculation of Non-Linear Aerodynamic Characteristics of Wings with and their Wakes in Subsonic Flow," Isreal Journal of Technology, Vol. 16, 1978, pp. 83-96.

50. Gordon, R. and Rom, J., "Calculations of Aerodynamic Characteristics of Wings with Thickness and Camber by a New Method Based on the Modified Vortex Lattice Method," Technion-Isreal Institute of Technology, Isreal, TAE Rept. 493, July 1982.

51. Kandil, O. A. and Balakrishnan, L., "Recent Improvements in the Prediction of the Leading and Trailing Edge Vortex Cores of Delta Wings," AIAA Paper 81-1263, June 1981.

52. Kandil, O. A., "Steady and Unsteady Incompressible Free-Wake Analysis," Lecture Presented at the International School of Applied Aerodynamics, International Center for Transportation Studies, Amalfi, Italy, May 1982.

53. Kalburgi, V., "A Non-Linear Vortex Panel Method for Wings with Edge Separation," M.S. Thesis, Old Dominion University, Virginia, May 1986.

54. Johnson, F. T. and Rubbert, P. E., "Advanced Panel Type Influence Coefficient Method Applied to Subsonic Flows," AIAA Paper 75-50, January 1975.

55. Weber, J. A., Brune, G. W., Johnson, F. T. Lu, P., and Rubbert, P. E., "Three Dimensional Solution of Flows Over Wings with Leading Edge Vortex Separation," AIAA Journal, Vol. 14, No.4, April 1976, pp. 519-525.

56. Johnson, F. T., Lu, P., Brune, G. W., Weber J. A., and Rubbert, P. E., "An Improved Method for the Prediction of Completely Three Dimensional Aerodynamic Load Distributions on Configuration with Leading Edge Separation," AIAA Paper 76-417, July 1976.

57. Johnson, F. T. and Tinoco, E. N., "Recent Advances in the Solution of Three Dimensional Flows Over Wings with Leading Edge Vortex Separation," AIAA Paper 79-0282, January 1979.

58. Johnson, F. T., Lu, P., Tinoco, E. N. and Epton, M. A.,"An Improved Panel Method for the Solution of Three Dimensional Leading Edge Vortex Flows," NASA-CR-3278, July 1980.

59. Johnson, F. T.; Lu, P.; Tinoco, P.; Epton, M. A., "An Improved Method for the Solution of Three-Dimensional Leading-Edge Vortex Flows," Volume I – Theory Document, NASA CR 3278. Volume II-User's Guide and Programmer's Document, 1980.

60. Kuhlman, J. M., "Analytical Studies of Separated Vortex Flows on Highly Swept Wings," NASA-CR-3022, November 1978.

61. Luckring, J. M., Schoonover, W. E., Jr. and Frink, N. T. "Recent Advances in Applying Free Vortex Sheet Theory for the Estimation of Vortex Flow Aerodynamics," AIAA Paper 82-0095, 1982.

62. Hoeijmakers, H. W. M. and Bennekers, B., "A Computational Model for the Calculation of the Flow About Wings with Leading-Edge Vortices," AGARD CP-247, 1979, Paper 25.

63. Hoeijmakers, H. W. M. and Vaatstra, W., "A Higher-Order Panel Method Applied to Vortex Sheet Roll-Up," AIAA Paper 82-0096, Jan. 1982.

64. Hoeijmakers, H. W. M., Vaatstra, W. and Verhaagen, N. G., "On the Vortex Flow over Delta and Double-Delta Wings," Journal of Aircraft, Vol. 20, No. 9, 1983, pp. 825-832.

65. Summa, J. M.,"A Numerical Method for the Exact Calculation of Airloads Associated with Impulsively Started Wings," AIAA Paper 77-2, 1977.

66. Luckring, J. M., Schoonover, W. E., Jr., and Frank, N. T.,"Recent Advances in Applying Free Vortex Sheet Theory for the Estimation of Vortex Flow Aerodynamics," AIAA Paper 82-0095, January, 1982.

67. Lamar, J. E. and Campbell, J. F.,"Recent Studies at NASA- Langley of Vortical Flows Interacting with Neighboring Surfaces," Aerodynamics of Vortical Type Flows in Three-Dimensions, AGARD CP 342, April 1983, pp. 10.1-10.32.

68. Morino, L.,"A general Theory of Unsteady Compressible Potential Aerodynamics," NASA CR-2464, 1974.

69. Kuo, C. C. and Morino, L.,"Steady Subsonic Flow Around Finite-Thickness Wings," NASA CR-2616, November 1975.

70. Morino, L., Chen, L. T., and Suciu, E. O.,"Steady and Oscillatory Subsonic and Supersonic Aerodynamics Around Complex Configurations," AIAA J., Vol. 13, March 1975, pp. 368-374.

71. Morino, L. and Tseng, K.,"Steady, Oscillatory and Unsteady, Subsonic and Supersonic Aerodynamics (SOUSSA) for Complex Aircraft Configurations," AGARD Symposium on Unsteady Aerodynamics, Ottawa, Canada, September 26-28, 1977.

72. Suciu, E. O. and Morino, L.,"Nonlinear Steady Incompressible Lifting-Surface Analysis with Wake Roll-Up," AIAA J., Vol. 15, January 1977.

73. Kandil, O. A., Chu, L-C. and Yates, E. C., Jr."A Hybrid Method for Lifting Surfaces with Free Vortex Flows," AIAA Paper 80-79, January 1980.

74. Chu, L-C., "Non-Linear Hybrid Vortex Method for Wings Having Side Edge Separation," M.S. Thesis, Old Dominion University, Virginia, December 1980.

75. Kandil, O. A., Chu, L-C. and Tureaud, T., "A Non-Linear Hybrid Vortex Method for Wings at Large Angle of Attack," AIAA Journal, Vol. 22, No. 3, March 1984, pp. 329-336. (Also published as AIAA Paper 82-351, January 1982)

76. Yen, A., Mook, D. T. and Nayfeh, A. H., "Non-Linear Continuous Vorticity Aerodynamic Model," AIAA Paper 80-0311, January 1980.

77. Yen, A., Mook, D. T. and Nayfeh, A. H., "A Continuous Vorticity Panel Method for Lifting Surfaces," AIAA Paper 81-1895, August 1981.

78. Yen, A., "A Continuous Vorticity Panel Method for the Prediction of Steady Loads on Lifting Surfaces," Ph.D. Dissertation, Dept. of Engg. Science and Mechanics, Virginia Polytechnic Institute and State University, January 1982.

79. Newsome, R. W. and Kandil, O. A., "Vortical Flow Aerodynamics - Physical Aspects and Numerical Simulation," AIAA Paper No. 87-0205, January 1987.

80. Salas, M. D., "Recent Developments in Transonic Euler Flow Over a Circular Cylinder," Mathematics and Computers in Simulation, vol. XXV, 1983, pp. 232-236.

81. Marconi, F., "The Spiral Singularity in the Supersonic Inviscid Flow Over a Cone," AIAA Paper No. 83-1665, July 1983.

82. Marconi, F., "Shock Induced Vorticities on Elliptic Cones in Supersonic Flow," AIAA Paper No. 85-0433, Jan. 1985.

83. Eriksson, L. E. and Rizzi, A., "Computation of Vortex Flow Around Wings Using the Euler Equations," Proc. 4th GAMM Conference on Numerical Methods in Fluid Mechanics, ed. Viviand, H., Vieweg Verlag, Paris, 1981, pp. 87-105.

84. Rizzi, A., "Damped Euler Equation Methods to Compute Transonic Flow Around Wing-Body Combinations," AIAA Journal, vol. 20, Oct. 1982, pp. 1321-1328.

85. Rizzi, A., Eriksson, L. E., Schmidt, W., and Hitzel, S. M., "Simulating Vortex Flow Around Wings," Aerodynamics of Vortical Type Flows in Three Dimensions, AGARD CP-342, Paper No. 21, July 1983.

86. Rizzi, A., "Euler Solutions of Transonic Vortex Flow Around the Dillner Wing – Compared and Analyzed," AIAA Paper No. 84-2142, Aug. 1984.

87. Hoeijmakers, H. W. M. and Rizzi, A., "Vortex-fitted Potential Solution Compared with Vortex-Captured Euler Solution for Delta Wing with Leading-Edge Vortex Separation," AIAA Paper No. 84-2144, 1984.

88. Raj, P. and Sikora, J., "Free Vortex Flows: Recent Encounters with an Euler Code," AIAA Paper No. 84-0135, Jan. 1984.

89. Murman, E. M., Powell, K. G., Miller, D. S., and Wood, R. M., "Comparison of Computational and Experimental Data for Leading Edge Vortices-Effects of Yaw and Vortex Flaps," AIAA Paper No. 86-0439, Jan. 1986.

90. Fujii, K. and Obayashi, S., "Evalulation of Euler and Navier-Stokes Solutions for Leading-Edge and Shock-Induced Separations," AIAA Paper No. 85-1563, July 1985.

91. Manie, F. Neron, M., and Schmitt, V., "Experimental and Computational Investigation of the Vortex Flow Over a Swept Wing," 14th International Council of the Aeronautical Sciences, ICAS-14-2.8.1, Sept. 1984.

92. Newsome, R. W., "Euler and Navier-Stokes Solutions for Flow Over a Conical Delta Wing," AIAA Journal, April 1986, pp. 552-561.

93. Hitzel, S. M. and Schmidt, W., "Slender Wings with Leading-Edge Vortex Separation - A Challenge for Panel Methods and Euler Solvers," Journal of Aircraft, vol. 21, Oct. 1984, pp. 751-759.

94. Newsome, R. W., "Euler and Navier-Stokes Solutions for Flow Over a Conical Delta Wing," AIAA Journal, April 1986, pp. 552-561.

95. Kandil, O. A. and Chuang, A., "Influence of Numerical Dissipation in Computing Supersonic Vortex-Dominated Flows," AIAA Paper No. 86-1073, May 1986, Also AIAA Journal, Vol. 25, No. 11, Nov. 1987, pp. 1426-1434.

96. Powell, K. G., Murman, E. M., Perez, E., and Baron, J., "Total Pressure Loss in Vortical Solutions of the Conical Euler Equations," AIAA Paper No. 85-1701, July 1985.

97. Marconi, F., "Flat Plate Delta Wing Separated Flows with Zero Total Pressure Loss," AIAA Paper No. 87-0038, Jan. 1987.

98. Powell, K. G. and Murman, E. M., "Vortical Solutions of the Conical Euler Equations," Vortex Flow Minisymposium SIAM National Meeting, Boston, Mass., July 1986, (oral presentation).

99. Kandil, O. A., Chuang, A. and Shiffette, J. M., "Finite Volume Euler and Navier-Stokes Solvers for Three Dimensional and Conical Vortex Flows Over Delta Wings," AIAA Paper No. 87-0041, Jan. 1987.

100. Cole, J. D., "Twenty Years of Transonic Flow," Boeing Scientific Research Laboratories Report DL-82-0878, July, 1969.

101. Lax, P. D., "Weak Solutions of Nonlinear Hyperbolic Equations and Their Numerical Computation," Comm. Pure Appl. Math. 7, pp. 159-193, 1954.

102. Magnus, R. and Yoshihara, H., "Inviscid Transonic Flow over Airfoils," AIAA paper 70-47, Jan. 1970 .

103. Murman, E. M. and Cole, J. D., "Calculation of Plane Steady Transonic Flows," AIAA J., 9, pp. 114-121, 1971.

104. Bailey, F. R. and Ballhaus, W. F., "Relaxation Methods for Transonic Flow about Wing-Cylinder Combinations and Lifting Swept Wings," Lecture Notes in Physics, vol. 19, pp. 2-9, Springer, New York, 1975.

105. Jameson, A., "Transonic Flow Calculations," Numerical Methods in Fluid Dynamics, Hemisphere Publishing Corp., New York, 1978, pp. 1-87.

106. Ballhaus, W. F., "Some Recent Progress in Transonic Flow Computations," Numerical Methods in Fluid Dynamics, Hemisphere Publishing Corp., New York, 1978, pp. 155-234.

107. Schmidt, W., "Progress in Transonic Flow Computation," Numerical Methods in Fluid Dynamics, Hemisphere Publishing Corp., New York, 1978, pp. 299-338.

108. Jameson, A., "Remark on the Calculation of Transonic Potential Flow by a Finite Volume Method," Numerical Methods in Applied Fluid Dynamics, published by Academic Press, New York, pp. 363-386, 1980.

109. Steger, J. L. and Lomax, H., "Transonic Flow About Two-Dimensional Airfoils by Relaxation Procedures," AIAA J., 10, pp. 49-54, 1972.

110. Garabedian, P. R. and Korn, D., "Analysis of Transonic Airfoils," Comm. Pure Appl. Math., 24, pp. 841-851, 1972.

111. Jameson, A., "Iterative Solution of Transonic Flows over Airfoils and Wings," Comm. Pure Appl. Math., 27, pp. 283-309, 1974.

112. Holst, T. L. and Ballhaus, W. F., "Fast, Conservative Schemes for the Full Potential Equation Applied to Transonic Flows," AIAA J., 17, pp. 145-152, 1979.

113. Steger, J. L. and Caradonna, F. X., "A Conservative Implicit Finite Difference Algorithm for the Unsteady Transonic Full Potential Equation," AIAA Paper 80-1368, 1980.

114. Sankar, J. B., Malone, N. L., and Tassa, Y., "An Implicit Conservative Algorithm for the Calculation of Transonic Flow Over Wing/Body Combinations," AIAA Paper 81-1016, June 1981.

115. Murman, E. M., "Transonic Aerodynamics," AIAA Professional Study Series, AIAA, New York, 1975.

116. MacCormack, R. W. and Paullay, A. J., "The Influence of the Computational Mesh on Accuracy for Initial Value Problems with Discontinuities or Nonunique Solutions," Comput. Fluids, 2, pp. 339-361, 1974.

117. MacCormack, R. W., Rizzi, A. W., and Inouye, M., "Steady Supersonic Flow Fields with Embedded Subsonic Regions," Proc. Conf. Comput. Probl. Methods Aero. Fluid Dyn., University of Manchester, England, 1974.

118. Rizzi, A. W. and Inouye, M., "Time Split Finite Volume Method for Three Dimensional Blunt-Body Flow," AIAA J., 11, pp. 1478-1485, November 1973.

119. Rizzi, A. W., "Transonic Solutions of the Euler Equations by the Finite Volume Method," presented at the Symposium Transsonicum II, September 1975.

120. Caughey, D. A. and Jameson, A., "Recent Progress in Finite Volume Calculations for Wing-Fuselage Combination," AIAA Paper 79-1513, 1979.

121. Murman, E. M. and Stremel, P. M., "A Vortex Wake Capturing Method for Potential Flow Calculations," AIAA Paper 82-0947, June 1982.

122. Liepmann, H. W. and Roshko, A., "Elements of Gasdynamics," Wiley, New York, 1959.

123. Hafez, M., South, J. C., and Murman, E. M., "Artificial Compressibility Methods for Numerical Solutions of Transonic Full Potential Equation," AIAA J., 17, pp. 838-844, 1979.

124. Harten, A., "The Artificial Compression Method for Computation of Shocks and Contact Discontinuities: III. Self-Adjusting Hybrid Schemes," Mathematical Computation, 32, pp. 363-389, 1978.

125. Fuslang, D. F., and Williams, M. H., "Non-Isentropic Unsteady Transonic Small Disturbance Theory," AIAA Paper 85-600, 1985.

126. Bauer, F., Garabedian, P., Korn, D., and Jameson, A., "Supercritical Wing Sections II," Springer, New York, 1975.

127. Bauer, F. and Korn, D., "Computer Simulation of Transonic Flow Past Airfoils with Boundary Correction," Proc. Second AIAA Conf. Comput. Fluid Dyn., pp. 184-204, Hartford, June 1975.

128. Bavitz, P. C., "An Analysis Method for Two-Dimensional Transonic Viscous Flow," NASA TN D-7718, 1975.

129. Jameson,A., Schmidt, W., and Turkel, E., "Numerical Solution of the Euler Equations by Finite Volume Methods Using Runge-Kutta Time-Stepping Schemes," AIAA Paper 81-1259, June 1981.

130. Sankar, N. L., Wake, B. E., and Lekoudis, S. G., "Solution of the Unsteady Euler Equations for Fixed and Rotor Wing Configurations," AIAA Paper 85-0120, Jan. 1985.

131. Steger, J. L. and Warming, R. F., "Flux Vector Splitting of the Inviscid Gasdynamic Equations with Application to Finite Difference Methods," NASA TM D-78605, 1979.

132. Chakravarthy, S. R., "The Split-Coefficient Matrix Method for Hyperbolic Systems of Gasdynamic Equations," Ph.D. dissertation, Dept. of Aerospace Engineering, Iowa State University, Ames, 1979.

133. Chakravarthy, S. R., Anderson, D. A., and Salas, M. D., "The Split-Coefficient Matrix Method for Hyperbolic Systems of Gasdynamic Equations," AIAA Paper 80-0268, Pasadena, California, 1980.

134. Steger, J. L., "Coefficient Matrices for Implicit Finite Difference Solution of the Inviscid Fluid Conservation Law Equations," Comput. Methods Appl. Mech. Eng., 13, pp. 175-188, 1978.

135. Anderson, D. A., Tannchill, J. C., Pletcher, R. H., "Computational Fluid Mechanics and Heat Transfer," Hemisphere Publishing Corp, New York, 1984.

136. Rizzi, A., "Transonic Solutions of the Euler Equations by the Finite Volume Method," Symposium Transsonicum II, pp. 567-574, Göttingen, September 1975.

137. Beam, R. M. and Warming, R. F., "An Implicit Finite Difference Algorithm for Hyberbolic Systems in Conservation Law Form," J. Comput. Phys., 22, pp. 87-110, 1976.

138. Jameson, A., "Transonic Airfoil Calculations Using the Euler Equations," Numerical Methods in Aeronautical Fluid Dynamics, ed. Roe, pp. 289-309, Academic Press, New York, 1982.

139. Rizzi, A., "Three-Dimensional Solutions to Euler Equations with One Million Grid Points," AIAA J., 23, pp. 1986-1987, Dec. 1985.

140. MacCormack, R. W. and Rizzi, A. W., "Steady Supersonic Flowfields with Embedded Subsonic Regions," Computational Methods and Problems in Aeronautical Fluid Dynamics, Academic Press, pp. 424-447, 1976.

141. Spreiter, J. R., "Transonic Aerodynamics - History and Statement of the Problem," Progress in Aeronautics and Astronautics: Transonic Aerodynamics, Vol. 81, ed. Nixon, D., pp. 3-79, AIAA, New York, 1982.

142. Spreiter, J. R. and Alksne, A., "Theoretical Prediction of Pressure Distributions on Nonlifting Airfoils at High Subsonic Speeds," NACN TN 3096, 1954.

143. Oswatitsch, K., "Die Geschwindigkeitsverteilung an symmetrischen Profilen beim Auftreten lokaler Überschallgebiete," Acta Physica Austriaca, 4, pp. 230-271, 1950.

144. Guderley, K. G., "On the Transition from a Transonic Potential Flow to a Flow with Shocks," Report F-TR-2160 ND, Headquarters, Air Material Command, Wright Field, OH, 1947.

145. Crown, J. C., "Calculation of Transonic Flow over Thick Airfoils by Integral Methods," AIAA J., 6, pp. 413-423, March 1968.

146. Spreiter, J. R. and Stahara, S. S., "Aerodynamics of Slender Bodies and Wing-Body Combinations at $M_\infty = 1$," AIAA J., 9, pp. 1784-1791, Sept. 1971.

147. Nixon, D., "Transonic Flow around Symmetric Aerofoils at Zero Incidence," J. of Aircraft, 11, pp. 122-124, Feb. 1974.

148. Nixon, D., "An Extended Integral Equation Method for the Steady Transonic Flow Past a Two - Dimensional Aerofoil," Computational Methods and Problems in Aeronautical Fluid Dynamics, Academic Press, New York, 1976.

149. Morino, L. and Tseng, K., "Time - Domain Green's Function Method for Three - Dimensional Nonlinear Subsonic Flows," AIAA Paper 78-1204, July 1978.

150. Tseng, K. and Morino, L., "Nonlinear Green's Function Method for Unsteady Transonic Flows," Progress in Aeronautics and Astronautics: Transonic Aerodynamics, Vol. 81, ed. Nixon, D., pp. 565-603, AIAA, New York, 1982.

151. Tseng, K., "Nonlinear Green's Function Method for Transonic Potential Flow," Ph.D. Dissertation, Boston University, 1983.

152. Piers, W. J. and Slooff, J. W., "Calculation of Transonic Flow by Means of a Shock-Capturing Field Panel Method," AIAA Paper 79-1459, 1979.

153. Johnson, F. T., James, R. M., Bussoletti, J. E., Woo, A. C. and Young, D. P., "A Transonic Rectangular Grid Embedded Panel Method," AIAA Paper 82-0953, 1982.

154. Bristeau, M. O., Glowinski, R., Periaux, J., Perrier, P., Pironneau, O., and Poirier, G., "On the Numerical Solution of Nonlinear Problems in Fluid Dynamics by Least Squares and Finite Element Methods (II) - Application to Transonic Flow," Computer Methods in Applied Mechanics and Engineering, Vol. 51, pp. 363-394, 1985.

155. Erickson, L. L. and Strande, S. M., "A Theoretical Basis for Extending Surface-Paneling Methods to Transonic Flow," AIAA J., Vol. 23, pp. 1860-1867, 1985.

156. Kandil, O. A., "Computational Technique for Compressible Vortex Flows Past Wings at Large Incidence," J. of Aircraft, Vol. 22, pp. 750-755, 1985.

157. Kandil, O. A. and Hu, H., "Integral Equation Solution for Transonic and Subsonic Aerodynamics," 3rd GAMM-Seminar Kiel (FRG), Panel Methods in Mechanics, 1987.

158. Sinclair, P. M., "An Exact Integral (Field Panel) Method for the Calculation of Two-Dimensional Transonic Potential Flow Around Complex Configurations," Aeron. J., pp. 227-236, 1986.

159. Samant, S., Bussoletti, J., Johnson, F., Burkhart, R., Everson, B., Melvin, R., Young, D., Erickson, L., Madson, M., Woo, A., "TRANAIR: A Computer Code for Transonic Analyses of Arbitrary Configurations," AIAA Paper 87-0034, 1987.

160. Bateman, H., "Irrotational Motion of a Compressible Inviscid Fluid," Proceedings of the National Academy of Sciences, Vol. 16, pp. 816-825, 1930.

161. James, R. A., "The Solution of Poisson's Equation for Isolated Source Distributions," J. of Computational Physics, Vol. 25, pp. 71-93, 1977.

162. Wigton, L. B., Yu, N. J. and Young, D. P., "GMRES Acceleration of Computational Fluid Dynamics Codes," AIAA Paper 85-1494, 1985.

163. Strang, G. and Fix, G, "Analysis of Finite Element Method," Prentice-Hall, Englewood Cliffs, N.J., 1973.

164. Pelz, R. and Jameson, A., "Transonic Flow Calculations Using Triangular Finite Elements," AIAA Paper 83-1922, 1983.

165. Chen, A. W., Dickson, L. J., and Rubbert, P.E., "A Far Field Matching Method for Transonic Computations," AIAA J., Vol. 15, pp. 1491-1497, 1977.

166. Lee, K. D., Dickson, L. J., Chen, A. W., and Rubbert, P. E., "An Improved Matching Method for Transonic Computations," AIAA Paper 78-1116, Seattle, Wash., 1978.

167. Kandil, O. A. and Hu, H., "Full-Potential Integral Solution for Transonic Flows with and without Embedded Euler Domains," AIAA Paper 87-1461, Honolulu, Hawaii, 1987.

168. Kandil, O. A. and Hu, H., "Transonic Airfoil Computation Using the Integral Equation with and without Embedded Euler Domains," 9th International Conference, Boundary Element Methods in Engineering, Stuttgart, Springer Verlag, Vol. 3, Sept., 1987.

169. Karamcheti, K., "Principles of Ideal-Fluid Aerodynamics," Wiley-Interscience, New York, 1966.

170. Landau, L. D. and Lifshitz, E. M., "Fluid Mechanics," Pergamon Press, New York, 1959.

171. Anderson, J. D., "Modern Compressible Flow with Historical Perspective," McGraw-Hill Book Company, 1982.

172. Cole, J. D. and Cook, L. P., "Transonic Aerodynamics," North-Holland, 1986.

173. Lessing, H. C., Troutman, J. L. and Menees, G. P., "Experimental Determination of the Pressure Distribution on a Rectangular Wing Oscillating in the

First Bending Mode for Mach Numbers from 0.24 to 1.30," NASA TND-344, December 1960.

174. Hu, H., "Full-Potential Integral Solution for Steady and Unsteady Transonic Airfoil Computations with and without Embedded Euler Domains," Ph.D. Dissertation, Dept. of Mechanical Engineering & Mechanics, Old Dominion University, May 1988.

175. Kelly, S. G., "A Systematic Investigation of the Parameters Affecting the Accuracy of the Vortex Lattice Method," M.S. Thesis, Dept. of Engineering Sciences & Mechanics, Virginia Polytechnic Institute and State University, Virginia, May 1977.

APPENDIX A

Relationship Between the Wing Vorticity Components and the Wake Vorticity Components

Consider a strip of free vortex sheet shed from side (i,ncp1), (i+1,ncp1) of the bounded vortex panel (JMR), Fig. 6. The boundary conditions need to be satisfied on the free vortex panel $(ms1)$ are stated as follows:

1. The vorticity vector $\vec{\omega}$ at node $(1, ms1)$ is along side $\overline{13}$ which is the ς-axis. Using this condition, two equations can be derived.

$$\omega_{\xi 1} = 0 \tag{A.1}$$

and

$$\begin{aligned} \omega_{\varsigma 1} &= \vec{\omega}(2, ms0) \cdot \vec{e}_{\varsigma}(ms1) \\ &= \left[\omega_{\varsigma}(2, ms0)\vec{e}_{\varsigma}(ms0) + \omega_{\xi}(2, ms0)\vec{e}_{\xi}(ms0)\right] \cdot \vec{e}_{\varsigma}(ms1) \\ &= \omega_{\varsigma}(2, ms0)E_{\varsigma\varsigma}(0,1) + \omega_{\xi}(2, ms0)E_{\xi\varsigma}(0,1) \end{aligned} \tag{A.2}$$

or in matrix form altogether

$$\begin{pmatrix} \omega_{\xi 1} \\ \omega_{\varsigma 1} \end{pmatrix}_{ms1} = \begin{pmatrix} 0 & 0 \\ E_{\xi\varsigma}(0,1) & E_{\varsigma\varsigma}(0,1) \end{pmatrix} \begin{pmatrix} \omega_{\xi 2} \\ \omega_{\varsigma 2} \end{pmatrix}_{ms0} \tag{A.3}$$

where

$$E_{\varsigma\varsigma}(0,1) = \vec{e}_{\varsigma}(ms0) \cdot \vec{e}_{\varsigma}(ms1)$$

$$E_{\xi\varsigma}(0,1) = \vec{e}_{\xi}(ms0) \cdot \vec{e}_{\varsigma}(ms1)$$

2. The vorticity vector $\vec{\omega}$ at node $(2, ms1)$ is along side $\overline{13}$ of panel $(ms2)$, i.e., $|\vec{\omega}(3, ms0)| = |\vec{\omega}(2, ms1)| = \vec{\omega}(2, ms1) \cdot \vec{e}_{\varsigma}(ms2)$. Therefore, we can obtain two equations

$$\begin{aligned} &\omega_{\xi}(2, ms1)E_{\xi\varsigma}(1,2) + \omega_{\varsigma}(2, ms1)E_{\varsigma\varsigma}(1,2) \\ &= \omega_x i(3, ms0)E_{\xi\varsigma}(0,2) + \omega_{\varsigma}(3, ms0)E_{\varsigma\varsigma}(0,2) \end{aligned} \tag{A.4}$$

and

$$\omega_{\xi}(2, ms1)E_{\xi\xi}(1,2) + \omega_{\varsigma}(2, ms1)E_{\varsigma\xi}(1,2) = 0 \tag{A.5}$$

or in matrix form

$$\begin{pmatrix} E_{\xi\xi}(1,2) & E_{\varsigma\xi}(1,2) \\ E_{\xi\varsigma}(1,2) & E_{\varsigma\varsigma}(1,2) \end{pmatrix} \begin{pmatrix} \omega_{\xi 2} \\ \omega_{\varsigma 2} \end{pmatrix}_{ms1} = \begin{pmatrix} 0 & 0 \\ E_{\xi\varsigma}(0,2) & E_{\varsigma\varsigma}(0,2) \end{pmatrix} \begin{pmatrix} \omega_{\xi 3} \\ \omega_{\varsigma 3} \end{pmatrix}_{ms0}$$

thus,

$$\begin{pmatrix} \omega_{\xi 2} \\ \omega_{\varsigma 2} \end{pmatrix}_{ms1} = \begin{pmatrix} F_{11} & F_{12} \\ F_{21} & F_{22} \end{pmatrix} \begin{pmatrix} \omega_{\xi 3} \\ \omega_{\varsigma 3} \end{pmatrix}_{ms0} \tag{A.6}$$

where

$$F_{11} = -E_{\varsigma\xi}(1,2)E_{\xi\varsigma}(0,2)/D_{12}$$

$$F_{12} = -E_{\varsigma\xi}(1,2)E_{\varsigma\varsigma}(0,2)/D_{12}$$

$$F_{21} = E_{\xi\xi}(1,2)E_{\xi\varsigma}(0,2)/D_{12}$$

$$F_{22} = E_{\xi\xi}(1,2)E_{\varsigma\varsigma}(0,2)/D_{12}$$

$$D_{12} = E_{\xi\xi}(1,2)E_{\varsigma\varsigma}(1,2) - E_{\xi\varsigma}(1,2)E_{\varsigma\xi}(1,2)$$

3. At node $(3, ms1)$, the vorticity vector $\vec{\omega}$ is along side $\overline{13}$ of panel $(ms3)$, and therefore, we can obtain the following equation

$$\vec{\omega}(3, ms1) \cdot \vec{e}_\xi(ms3) = 0$$

i.e.,

$$\begin{pmatrix} E_{\xi\xi}(1,3) & E_{\varsigma\xi}(1,3) \end{pmatrix} \begin{pmatrix} \omega_{\xi 3} \\ \omega_{\varsigma 3} \end{pmatrix}_{ms1} = \begin{pmatrix} 0 & 0 \end{pmatrix} \tag{A.7}$$

4. According to Holmholtz theory, $\Gamma_{23}|_{ms0} = \Gamma_{23}|_{ms1}$, which is written as

$$\int_2^3 \vec{\omega} \cdot \vec{n} d\ell|_{ms0} = \int_2^3 \vec{\omega} \cdot \vec{n} d\ell|_{ms1}$$

Since $\vec{\omega}$ is linear, and $\vec{n} = \vec{e}_{32} \times \vec{e}_\eta$, one can obtain the following equation through some manipulations

$$\begin{aligned} &\begin{pmatrix} \varsigma_{32} & \xi_2 \end{pmatrix}_{ms1} \begin{pmatrix} \omega_{\xi 2} \\ \omega_{\varsigma 2} \end{pmatrix}_{ms1} + \begin{pmatrix} \varsigma_{32} & \xi_2 \end{pmatrix}_{ms1} \begin{pmatrix} \omega_{\xi 3} \\ \omega_{\varsigma 3} \end{pmatrix}_{ms1} \\ &= \begin{pmatrix} \varsigma_{32} & \xi_2 \end{pmatrix}_{ms0} \begin{pmatrix} \omega_{\xi 2} \\ \omega_{\varsigma 2} \end{pmatrix}_{ms0} + \begin{pmatrix} \varsigma_{32} & \xi_2 \end{pmatrix}_{ms0} \begin{pmatrix} \omega_{\xi 3} \\ \omega_{\varsigma 3} \end{pmatrix}_{ms0} \end{aligned} \tag{A.8}$$

where $\varsigma_{32} = \varsigma_3 - \varsigma_2$ and ξ_2, ς_2 are the local coordinates of node 2. Substituting Eq. (A.6) into Eq. (A.8) and combining Eq. (A.7), the resulting equation can be simplified as

$$\begin{aligned} \begin{pmatrix} \omega_{\xi 3} \\ \omega_{\varsigma 3} \end{pmatrix}_{ms1} &= \begin{pmatrix} H_1 \varsigma_{32} & H_1 \xi_2 \\ H_2 \varsigma_{32} & H_2 \xi_2 \end{pmatrix}_{ms0} \begin{pmatrix} \omega_{\xi 2} \\ \omega_{\varsigma 2} \end{pmatrix}_{ms0} \\ &+ \begin{pmatrix} H_1 \left[\varsigma_{32} - GE_{\xi\varsigma}(0,2)\right] & H_1 \left[\xi_2 - GE_{\varsigma\varsigma}(0,2)\right] \\ H_2 \left[\varsigma_{32} - GE_{\xi\varsigma}(0,2)\right] & H_2 \left[\xi_2 - GE_{\varsigma\varsigma}(0,2)\right] \end{pmatrix}_{ms0} \begin{pmatrix} \omega_{\xi 3} \\ \omega_{\varsigma 3} \end{pmatrix}_{ms0} \end{aligned}$$

or

$$\begin{pmatrix} \omega_{\xi 3} \\ \omega_{\varsigma 3} \end{pmatrix}_{ms1} = \begin{pmatrix} K_{11} & K_{22} \\ K_{21} & K_{22} \end{pmatrix} \begin{pmatrix} \omega_{\xi 2} \\ \omega_{\varsigma 2} \end{pmatrix}_{ms0} + \begin{pmatrix} K_{11} - L_{11} & K_{12} - L_{12} \\ K_{21} - L_{21} & K_{22} - L_{22} \end{pmatrix} \begin{pmatrix} \omega_{\xi 3} \\ \omega_{\varsigma 3} \end{pmatrix}_{ms0} \tag{A.9}$$

where

$$K_{11} = H_1 \varsigma_{32}(ms0)$$

$$K_{12} = H_1 \xi_2(ms0)$$

$$K_{21} = H_2 \varsigma_{32}(ms0)$$

$$K_{22} = H_2 \xi_2(ms0)$$

$$L_{11} = H_1 G E_{\xi\varsigma}(0,2)$$

$$L_{12} = H_1 G E_{\varsigma\varsigma}(0,2)$$

$$L_{21} = H_2 G E_{\xi\xi}(0,2)$$

$$L_{22} = H_2 G E_{\varsigma\xi}(0,2)$$

$$H_1 = -E_{\varsigma\xi}(1,3)/D_{13}$$

$$H_2 = E_{\xi\xi}(1,3)/D_{13}$$

$$G = \left[\xi_2(ms1)E_{\xi\xi}(1,2) - \varsigma_{32}(ms1)E_{\varsigma\xi}(1,2)\right]/D_{12}$$

$$D_{13} = \xi_2(ms1)E_{\xi\xi}(1,3) - \varsigma_{32}(ms1)E_{\varsigma\xi}(1,3)$$

Adding Equations (A.3), (A.6), and (A.9) altogether, one obtain the following matrix expression:

$$\begin{pmatrix} \omega_{\xi 1} \\ \omega_{\varsigma 1} \\ \omega_{\xi 2} \\ \omega_{\varsigma 2} \\ \omega_{\xi 3} \\ \omega_{\varsigma 3} \end{pmatrix}_{ms1} = \begin{pmatrix} 0 & 0 & 0 & 0 \\ E_{\xi\xi}(0,1) & E_{\varsigma\xi}(0,1) & 0 & 0 \\ 0 & 0 & F_{11} & F_{12} \\ 0 & 0 & F_{21} & F_{22} \\ K_{11} & K_{12} & K_{11} - L_{11} & K_{12} - L_{12} \\ K_{21} & K_{22} & K_{21} - L_{21} & K_{22} - L_{22} \end{pmatrix} \begin{pmatrix} \omega_{\xi 2} \\ \omega_{\varsigma 2} \\ \omega_{\xi 3} \\ \omega_{\varsigma 3} \end{pmatrix}_{ms0} \tag{A.10}$$

In general, the five unknown nodal vorticities (since ω_ξ, is always 0) of a free vortex panel can be expressed in terms of nodal vorticities of the preceding one. Therefore, through a series of matrix multiplications as follows

$$
\begin{aligned}
(\omega_i)_{msn} &= (CS(i,j))_n\,(\omega_j)_{msn-1} \\
&= (CS(i,j))_n\,(CS(i-1,j))_{n-1}\cdots(CSG(i-1,j))_1\,(\omega_j)_{JMR}
\end{aligned}
\tag{A.11}
$$

the nodal vorticities of any free vortex panel can always be expressed in terms of the global nodal vorticities of bound-vortex panels. In Eq. (A.11), the matrix $CS(i-1,j)_{n-1}$ is equal to the matrix $CS(i,j)_{n-1}$ without the first row, where $CSG(i-1,j)$ is relating the nodal vorticities of the first free vortex panel to those of bound-vortex panel (JMR). In $CSG(i-1,j)$, the Kutta condition is also implied by aligning the vortex lines with the streamlines.

APPENDIX B

Study of Vectorization of the Computer Code for the Integral Equation Methods

Pipeline (parallel) computers with data vectorization processors have been used widely for scientific applications (e.g., CFD, FEM, etc.) in recent years due to their fast speed and large memory. The main factor for its success is the reduction of the data dependency through vectorization of DO loop. The degree of success of the vectorization depends on the degree of the level to which DO loop can be "cracked down."

Parallel processing is an efficient form of information processing which emphasizes the exploitation of concurrent events in the computing process. These concurrent events are attainable in a computer system at various processing levels. The highest level of parallel processing is conducted among multiple jobs or programs through multiprogramming, time sharing, and multiprocessing. The next highest level of parallel processing is conducted among procedures or tasks (program segments) within the same program. The third level is to exploit concurrency among multiple instructions. In the third level, data dependency analysis is often performed to reveal parallelism among instructions and vectorization may be desired among scalar operations within DO loops.

Parallel computers are those systems that emphasize parallel processing. The basic architectural features of parallel computers are pipeline computers, array processors, and multiprocessors. A pipeline computer (e.g., Cray-1, Cyber 205, etc.) performs overlapped computations to exploit temporal parallelism. An array processor (e.g., Illiac-IV, Brroughs BSP, etc.,) uses multiple synchronized arithmetic logic units to achieve spatial parallelism. A multiprocessor system (e.g., Cray-2, Cray X-MP, ETA-10, etc.,) achieves asynchronous parallelism through a set of interactive processors with shared resources (memories, database, etc.).

Due to the overlapped instruction and arithmetic execution, it is obvious that pipeline machines are better tuned to perform the same operations repeatedly through the pipeline. Therefore, pipeline computers are more attractive for vector processing where component operations may be repeated many times. Because of the characteristics of repeated operations in scientific programming, most of computers for scientific applications today are pipeline computers with data vectorization processor.

The cases tested here are incompressible flow around a rectangular wing with aspect ratio of 3 at an angle of attack of 5 degree and 10 degree. The computers used for tests are a Cyber 185 and a Cyber 205. Each case was tested in both scalar code and vector code. All cases but the 10 by 10 were tested in both full precision (64 bit word) and half precision (32 bit half word) calculations. The tested results are listed in Table 4.

For scalar mode, the Cyber 205 is about 15 to 20 times faster than Cyber 185. In this program, the vector processing seems no better than the scalar processing for the following reasons: First, as mentioned before, the vector computers are designed for applications where repeated operations are performed on data. Hence,

the larger the DO loop the better the computational efficiency can be achieved. Unlike the finite difference methods, the integral-equation methods require a lot of calculation steps in an induced-velocity-calculation DO loop, and hence the data dependency in the loop is very difficult to reduce. Therefore, the time saved can not compensate the overhead time spent due to vectorization. In general, for the machine used the time saved will break even with the overhead time spent when vector length is around 30 to 50. From numerical results, it was found that the induced-velocity calculations occupy 85 percent of the total computational time and matrix inversion takes less than a half percent of the computational time in 10 by 10 case. This really causes difficulties to vectorize the program in conventional programming. The following suggestions may provide a solution to the vectorization of the integral-equation methods computer program under the current vectorization algorithm of Cyber 205. The conventional programming for a DO loop is,

```
      DO 100 I=1,1000
      15 calculation steps
100   CONTINUE
```

the suggested way is

```
      DO 100 I=1,15
      1000 repeated calculations
100   CONTINUE
```

Alternatively, we break the DO-loop into several small loops depending on the data dependency analysis.

4 outer loops for 4 calculation steps

inner loop for 1000 repeated calculations

store results from 4 outer loops

6 outer loops for 6 calculation steps

inner loop for 1000 repeated calculations

store results from 6 outer loops

5 outer loops for 5 calculation steps

inner loop for 1000 repeated calculations

store results from 5 outer loops

In integral equation methods, full precision (64 bit) may not be necessary in the calculations, one can convert the Fortran program to half precision (32 bit) in order to achieve high computational efficiency and larger memory. In most cases (unless very large numbers of panels are used, where matrix inversion might need higher precision), the maximum difference in solutions is less than a half percent.

TABLE 1

Comparison of Calculations of Induced Velocity between Each of the Two Approximation Methods with the Closed-form Solution – 1

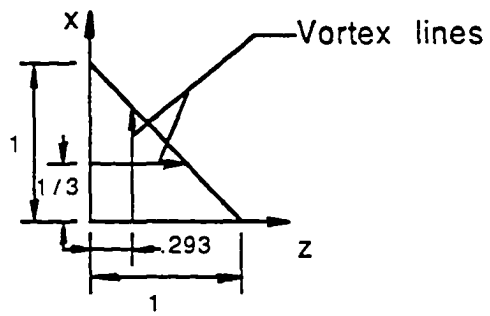

	Field Point			F/N			G/N		
dist	x	y	z	u	v	w	u	v	w
1.000	0.333	1.061	1.333	1.000	1.032	1.000	1.000	0.902	1.000
1.750	0.333	0.000	2.083	1.000	1.000	1.000	1.000	0.937	1.000
2.000	-0.891	-1.414	1.040	0.974	1.033	0.974	0.968	1.041	0.947
2.250	0.333	0.000	2.583	1.000	0.999	1.000	1.000	0.953	1.000
2.500	0.333	-1.768	2.101	0.993	1.036	0.993	1.006	1.014	0.950
2.750	0.333	1.945	2.278	0.994	1.03	0.994	1.005	1.011	0.956
3.000	0.333	0.000	3.333	1.000	1.000	1.000	1.000	0.967	1.000
3.250	0.333	2.298	2.631	0.996	1.021	0.996	1.003	1.006	0.964
4.000	-2.116	2.828	-1.081	1.003	1.017	1.003	1.001	1.047	1.007

F : far-field approximation with averaging panel vorticity

G : far-field approximation with two concentrated vortex lines

N : closed-form solution

TABLE 2

Comparison of Calculations of Induced-Velocity between Each of the Two Approximation Methods with the Closed-Form Solution - 2

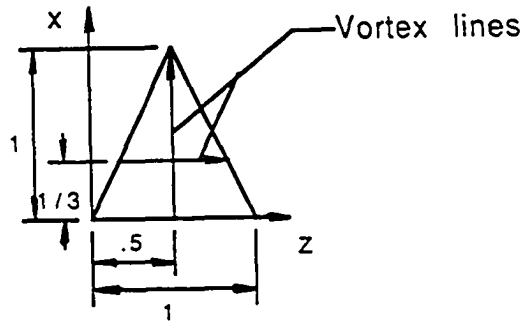

	Field Point			F/N			G/N		
dist	x	y	z	u	v	w	u	v	w
1.500	-0.197	-1.061	-0.419	0.983	1.021	0.983	1.003	0.689	0.859
1.750	-0.285	1.237	-0.572	0.987	1.015	0.987	1.003	0.734	0.881
2.000	2.065	0.000	1.500	1.000	1.017	1.000	1.000	0.514	1.000
2.500	-0.551	1.768	-1.031	0.994	1.007	0.994	1.002	0.816	0.919
2.750	2.715	0.000	1.875	1.000	1.005	1.000	1.000	0.692	1.000
3.000	2.931	0.000	2.000	1.000	1.004	1.000	1.000	0.726	1.000
3.250	-0.816	2.298	-1.490	0.997	1.004	0.997	1.001	0.860	0.939
3.500	-0.904	2.475	-1.643	0.997	1.004	0.997	1.001	0.870	0.944
3.750	3.581	0.000	2.375	1.000	1.002	1.000	1.000	0.795	1.000
4.000	3.797	0.000	2.500	1.000	1.001	1.000	1.000	0.811	1.000

F : far-field approximation with averaging panel vorticity

G : far-field approximation with two concentrated vortex lines

N : closed-form solution

TABLE 3

Comparison of Near-field Calculation and Far-field Approximation of Velocity Components Induced by Field Compressibility

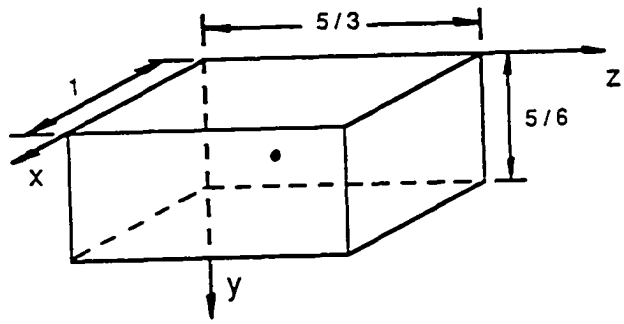

	Field Point			N-F		F-F	
dist	x	y	z	u	v	u	v
1.00	-0.500	0.417	0.833	1.12998	0.00000	1.38889	0.00000
1.302	-0.500	-0.417	0.833	0.54512	0.47123	0.62969	0.52474
1.944	-0.500	-1.250	0.833	0.17362	0.29579	0.18915	0.31526
2.167	-1.500	-0.417	0.833	0.26088	0.11010	0.27310	0.11379
2.560	-0.500	-1.250	-0.833	0.08511	0.14381	0.08275	0.13791
2.734	-1.500	-0.417	-0.833	0.13990	0.05887	0.13600	0.05667
3.091	-1.500	-1.250	-0.833	0.09485	0.07969	0.09404	0.07837
3.432	-2.500	-1.250	0.833	0.10110	0.05651	0.10309	0.05727

Note : comparison is done on u- & v-component only

dist : distance between field point and centroid of field volume

N-F : near-field calculation

F-F : far-field approximation

TABLE 4

Comparison of Computational Time for Vector and Scalar Codes

Case	Code/Bit	Machine	CPU sec
6 x 8. 5 deg.	Scalar/60	Cyber 185	880.0 (OPT=LOW)
6 x 8. 5 deg.	Scalar/60	Cyber 185	640.0 (OPT=HIGH)
6 x 8. 5 deg.	Scalar/32	Cyber 205	36.34
6 x 8. 5 deg.	Vector/32	Cyber 205	36.20(w/ KAP)
6 x 8,10 deg.	Scalar/32	Cyber 205	47.63
6 x 8,10 deg.	Vector/32	Cyber 205	47.45(w/ KAP)
6 x 8. 5 deg.	Scalar/64	Cyber 205	39.97
6 x 8. 5 deg.	Vector/64	Cyber 205	40.97(w/ KAP)
6 x 8,10 deg.	Scalar/64	Cyber 205	52.37
6 x 8,10 deg.	Vector/64	Cyber 205	53.56(w/ KAP)
10 x 10,5 deg.	Scalar/64	Cyber 205	155.23
10 x 10,5 deg.	Vector/64	Cyber 205	260.87(TRP,KAP)

HIGH : high optimization in FORTRAN compilation

KAP : software for optimizing DO loops

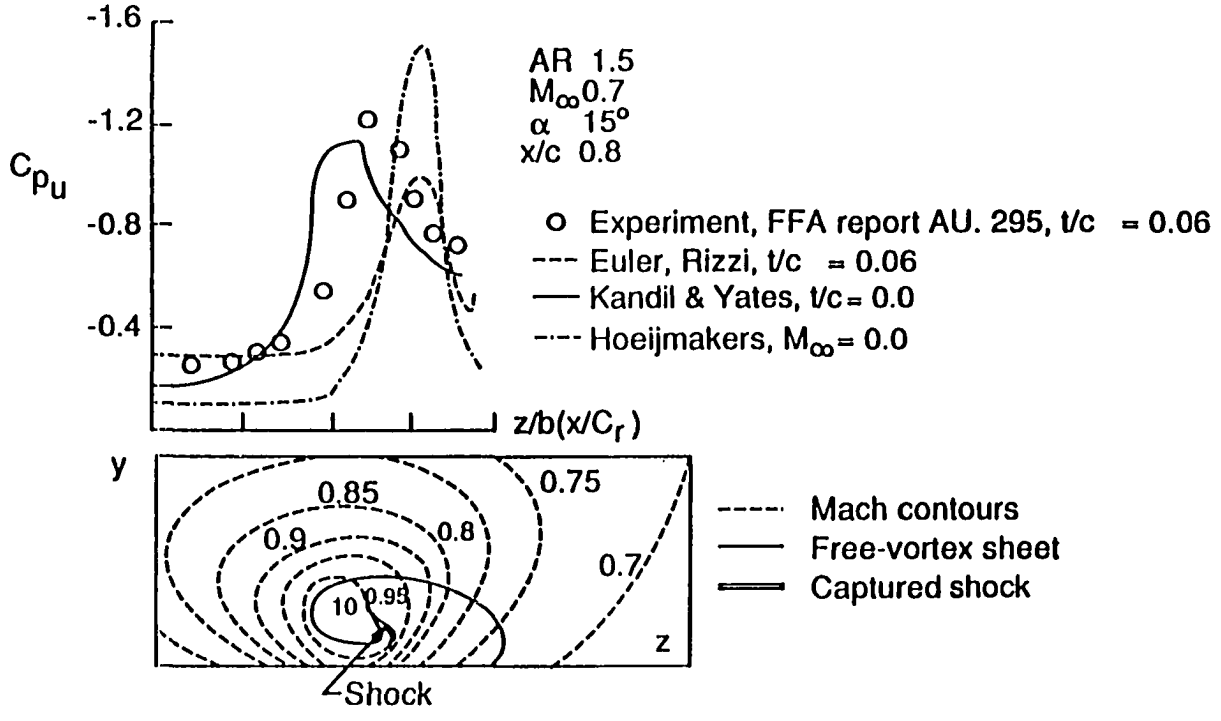

Fig. 1 Spanwise pressure variation and details of the flow over a delta wing in a cross-flow plane at x/c = 0.86

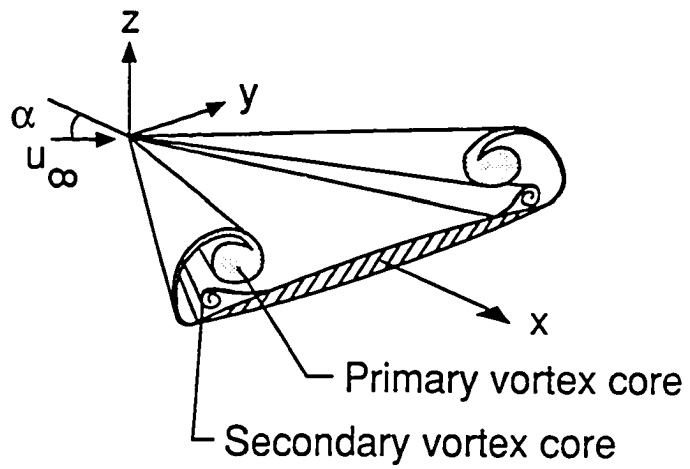

Fig. 2a Vortex flow about a delta wing

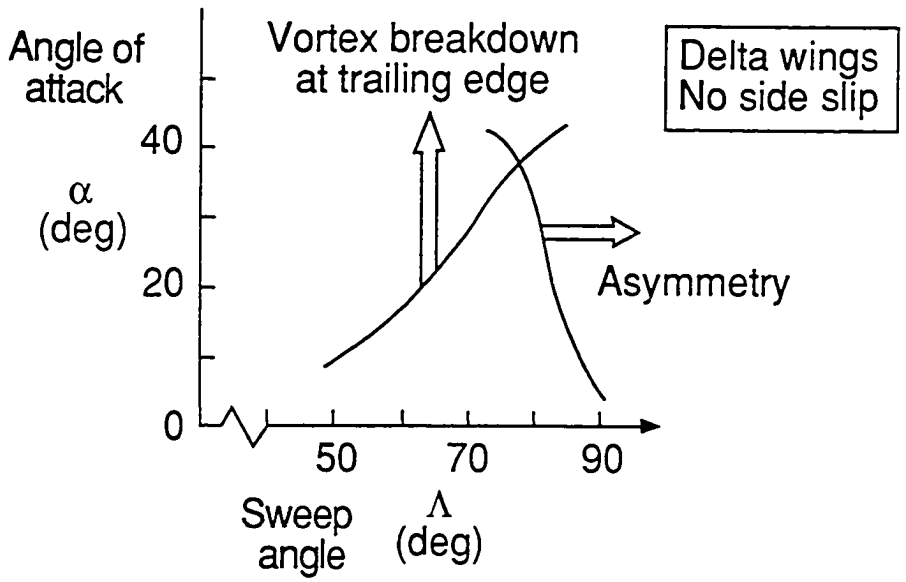

Fig. 2b Boundaries for onset of vortex breakdown and asymmetry (low speed)

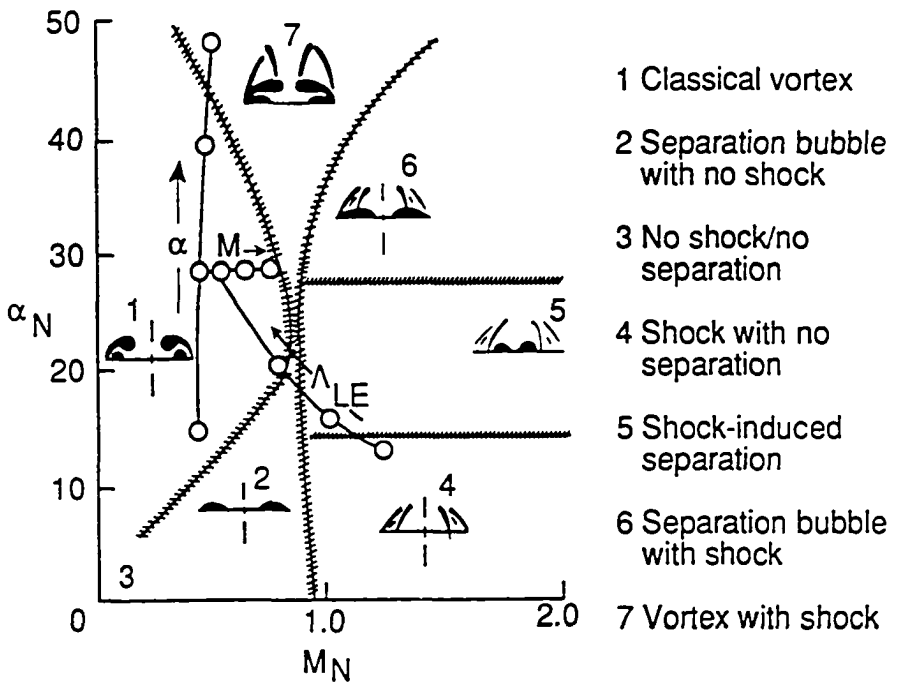

Fig. 2c Flow classification for sharp leading-edge delta wings according to angle of attack and Mach number normal to leading edge (Ref. 21)

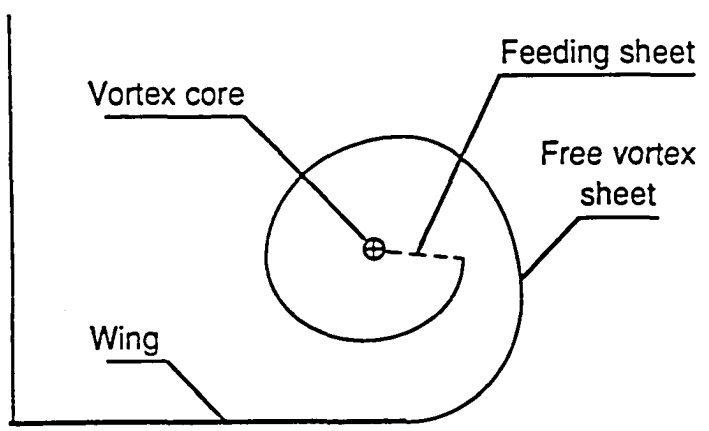

Fig. 3 Vortex core and the feeding sheet

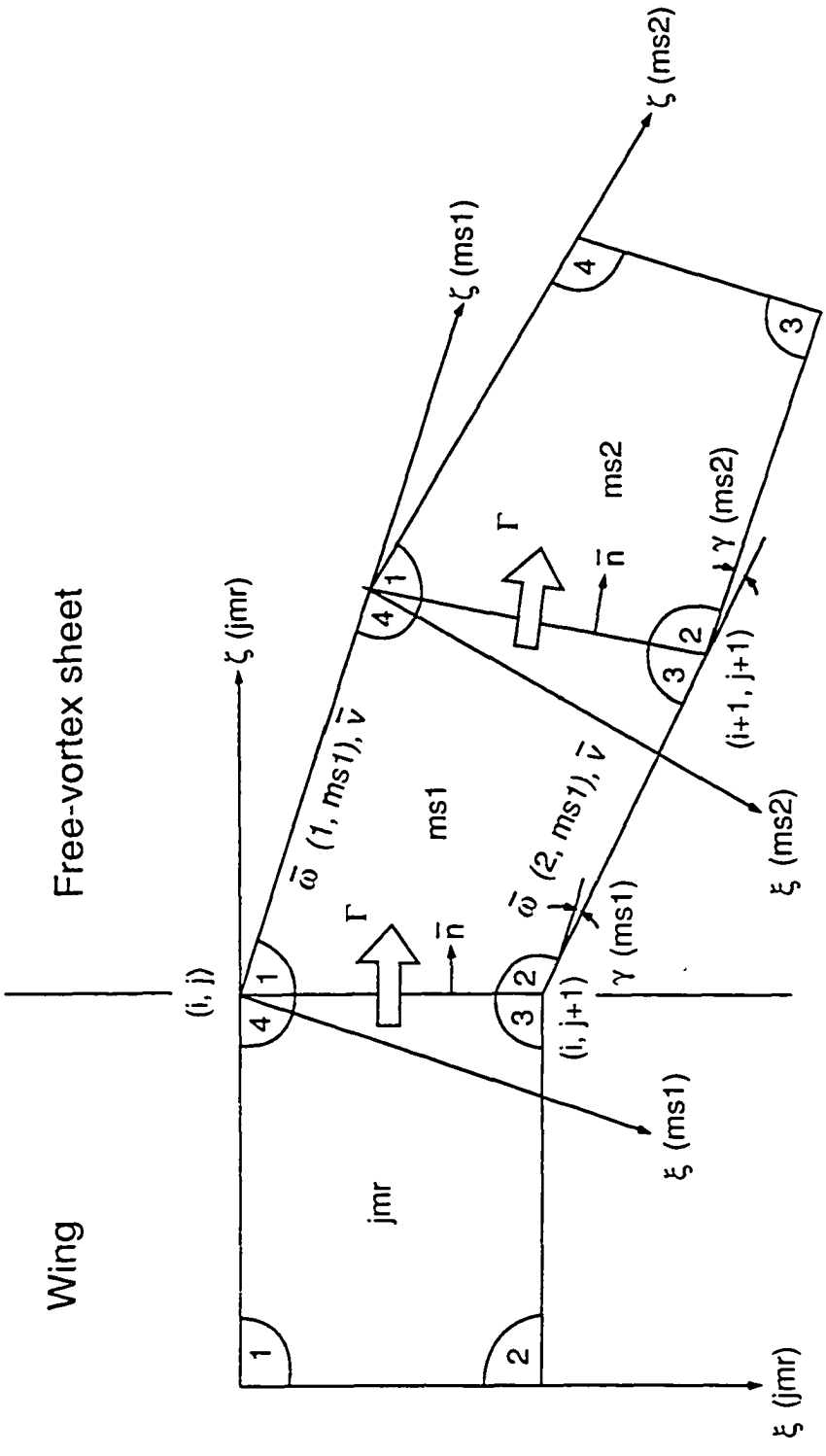

Fig. 4 Relationship between the coefficients of free and bound vortex panels (ref. 73)

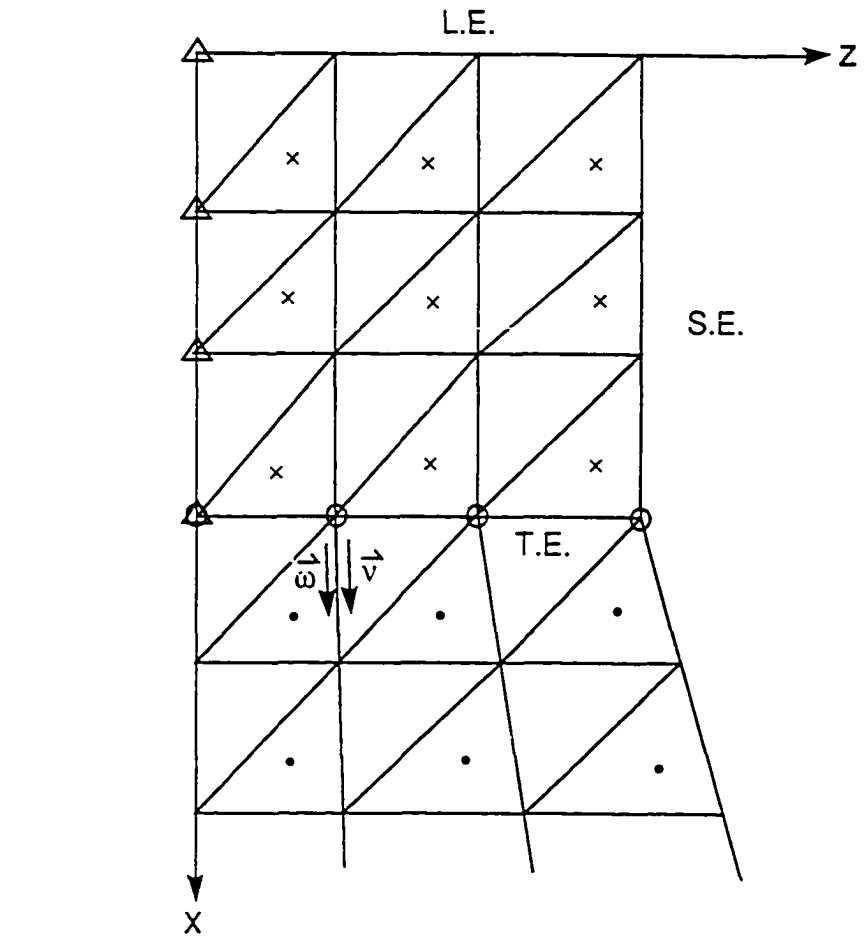

○ Kutta condition

△ Symmetry condition

× Flow tangency condition (centroid)

• Control point of free vortex panel (centroid)

Fig. 5 Discretization of bounded-and free-vortex sheets

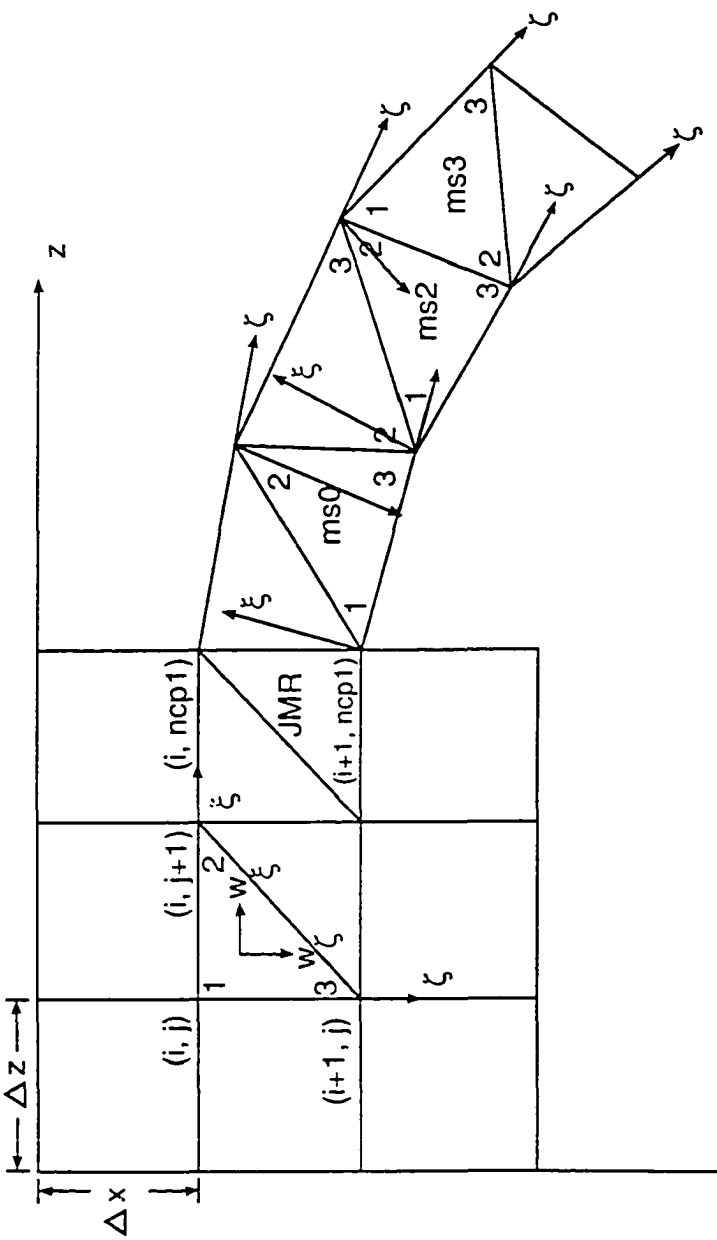

Fig. 6 Global & local coordinate systems
Boundary conditions of free vortex panels

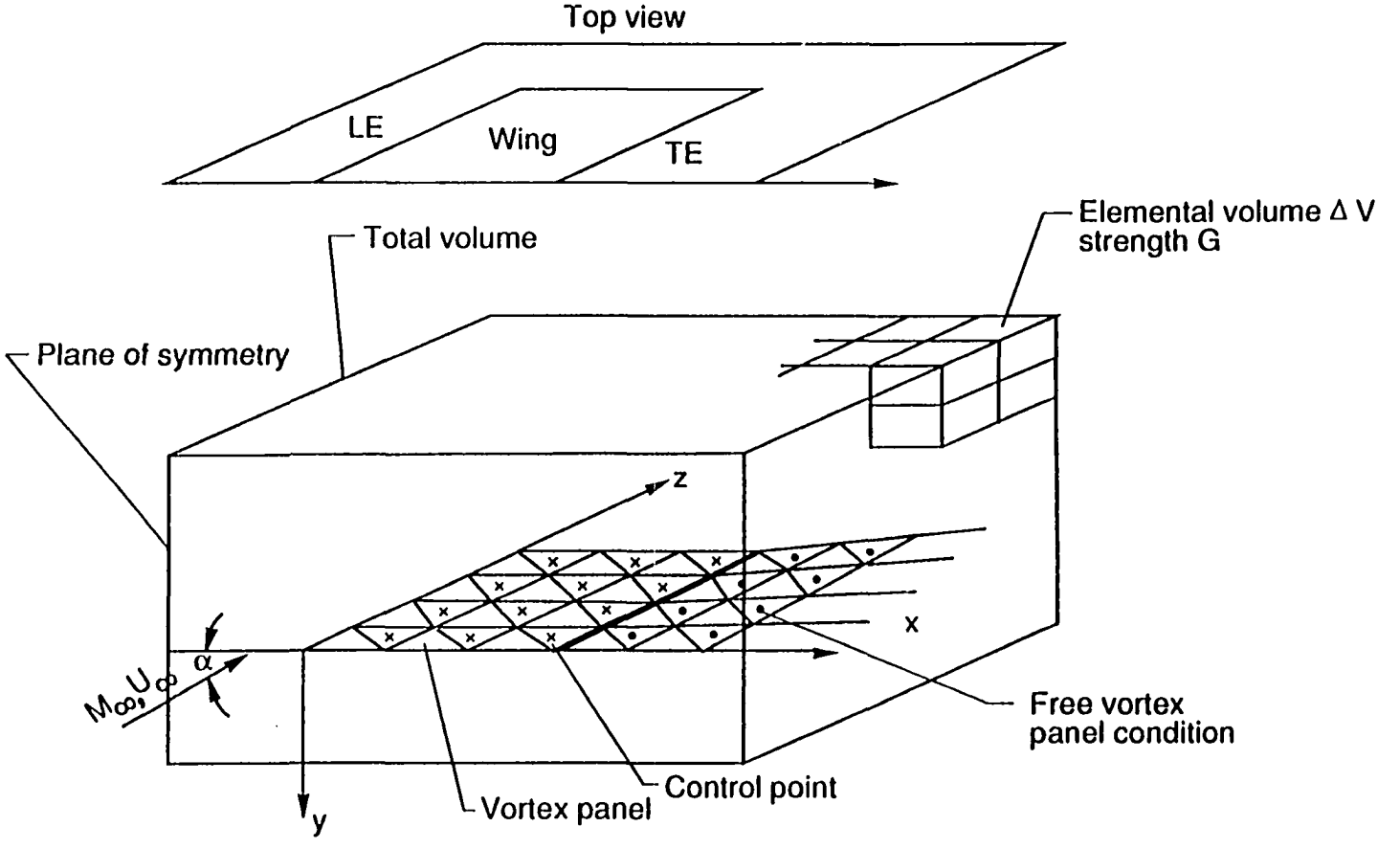

Fig. 7 Computational model for transonic- vortex flows using the integral equation method

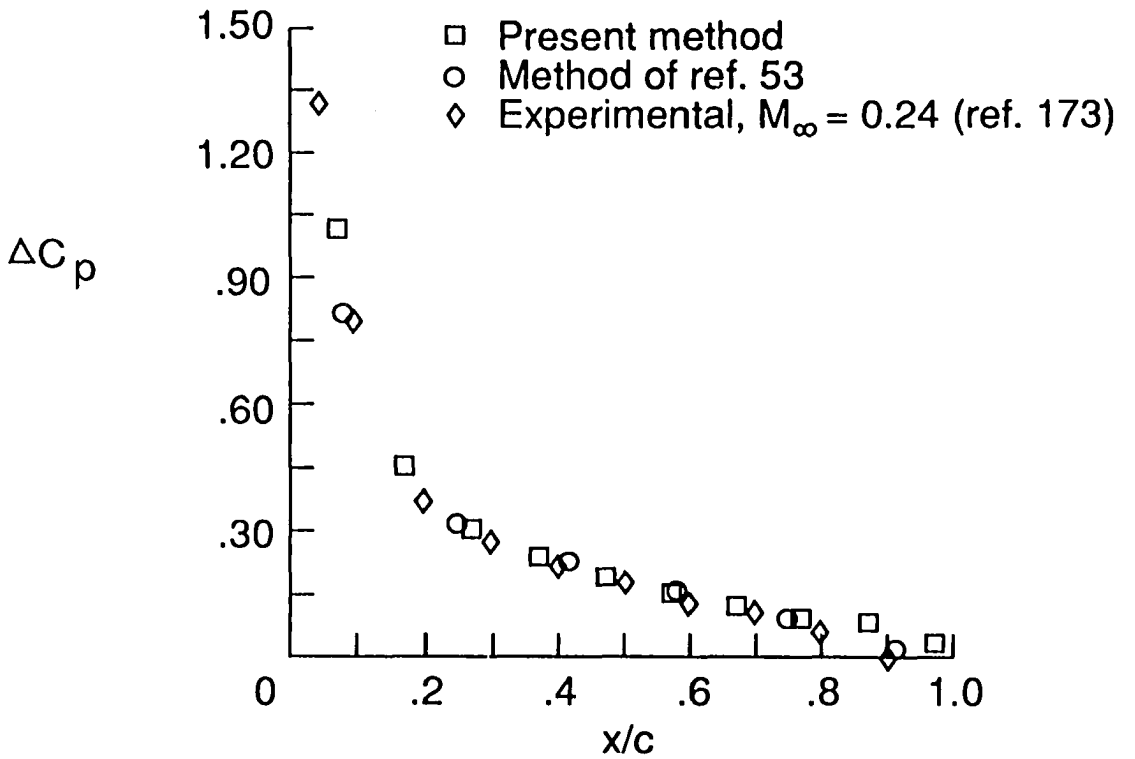

Fig. 8 Chordwise variation of lifting pressures for a rectangular wing of AR = 3.0, $\alpha = 5^{\circ}$, 50% span station

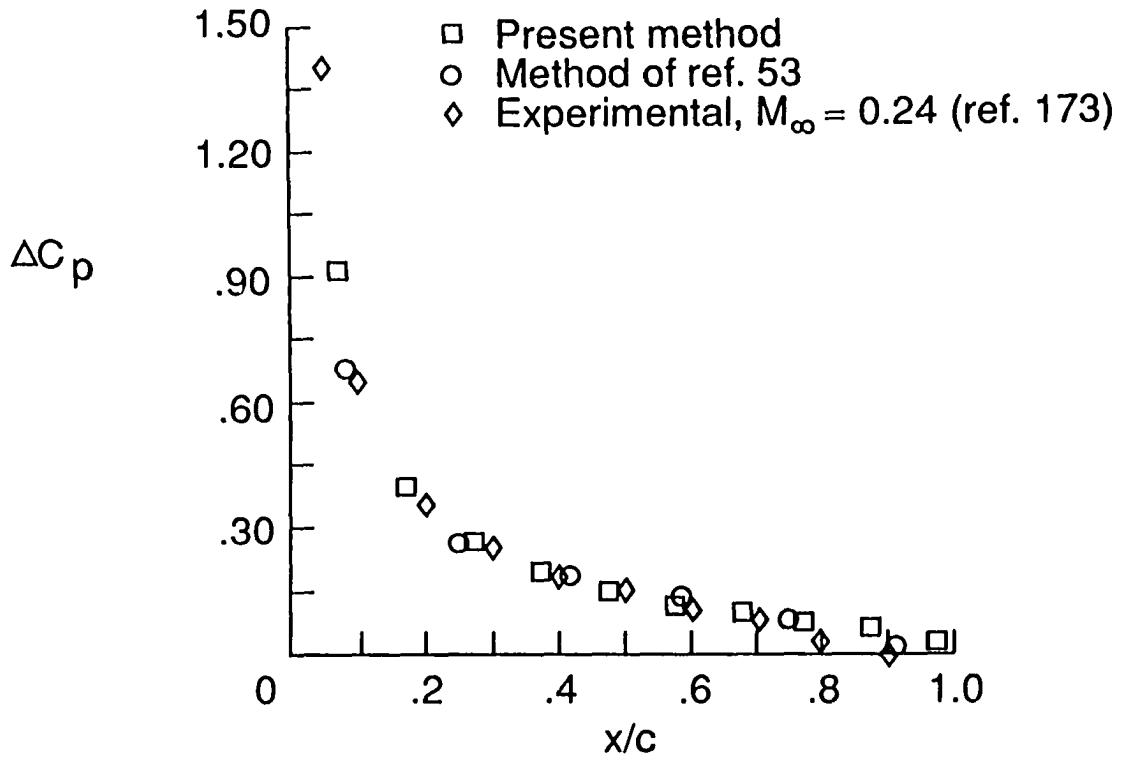

Fig. 9 Chordwise variation of lifting pressures for a rectangular wing of AR = 3, $\alpha = 5°$, 70% span station

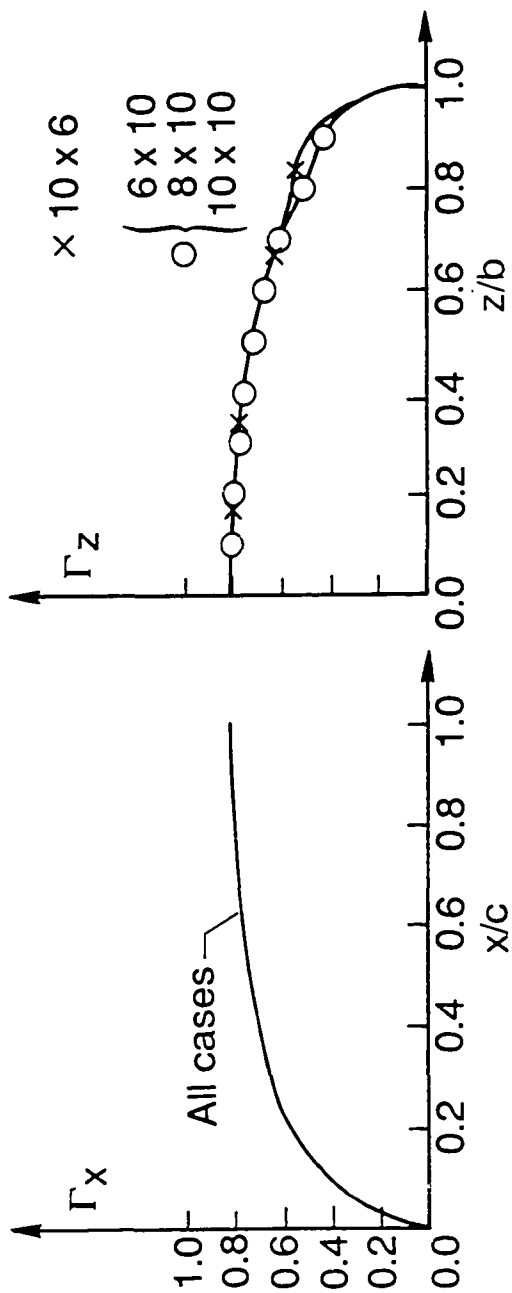

Fig. 10 Chordwise and spanwise distribution of circulation for various paneling for a rectangular wing of AR =1.0, c = 10, α= 5°

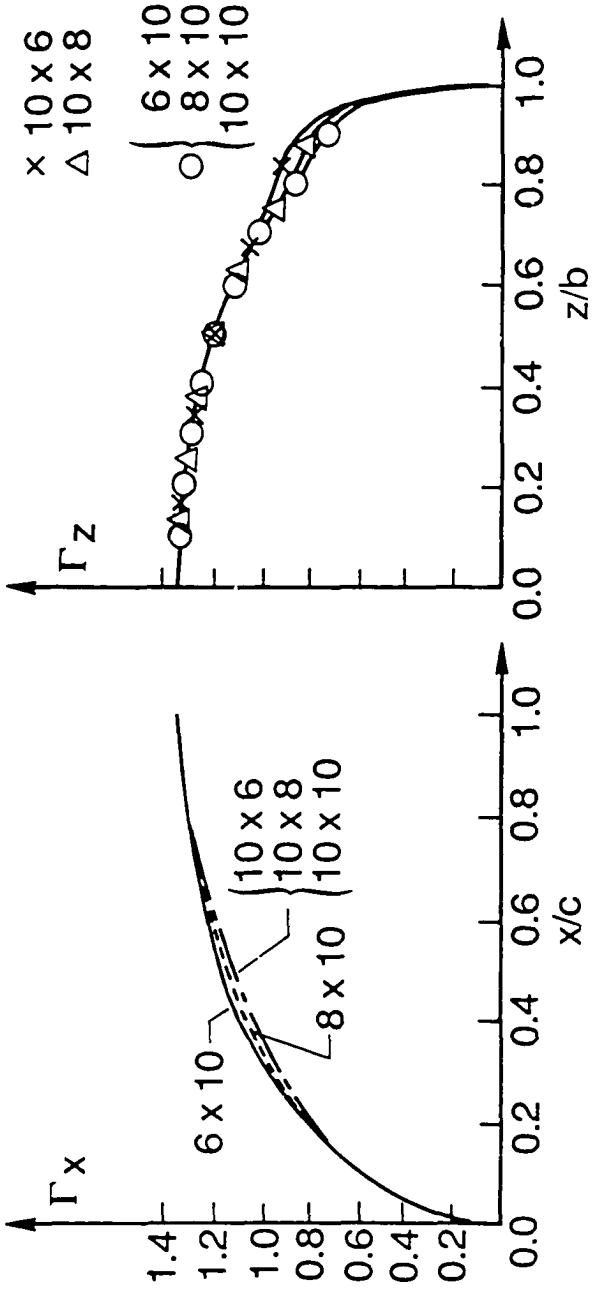

Fig. 11 Chordwise and spanwise distribution of circulation for various paneling for a rectangular wing of AR = 2.0, c = 10, α= 5°

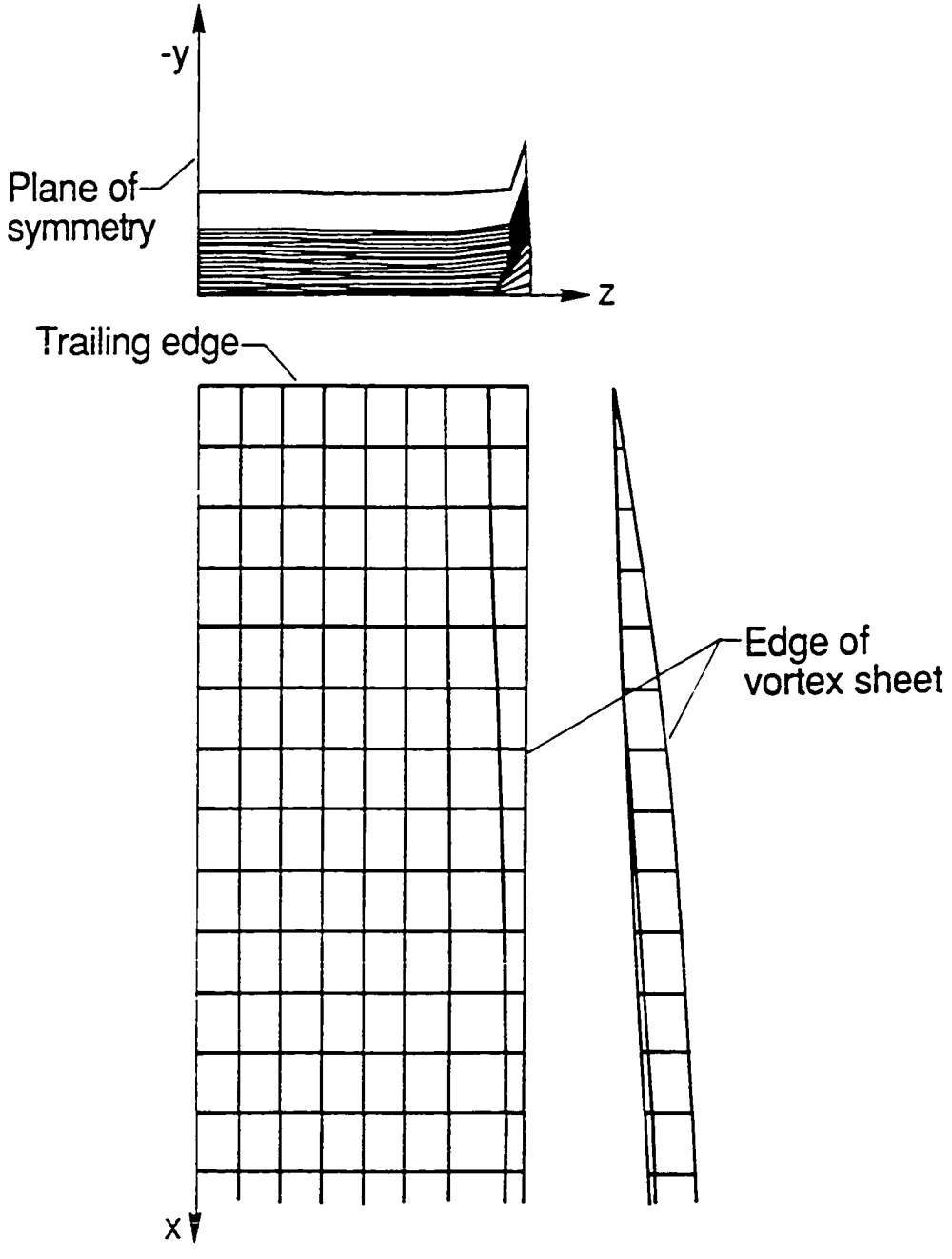

Fig. 12 Deformation of trailing-edge wake after 2 outer- and 5 inner-loop iterations.

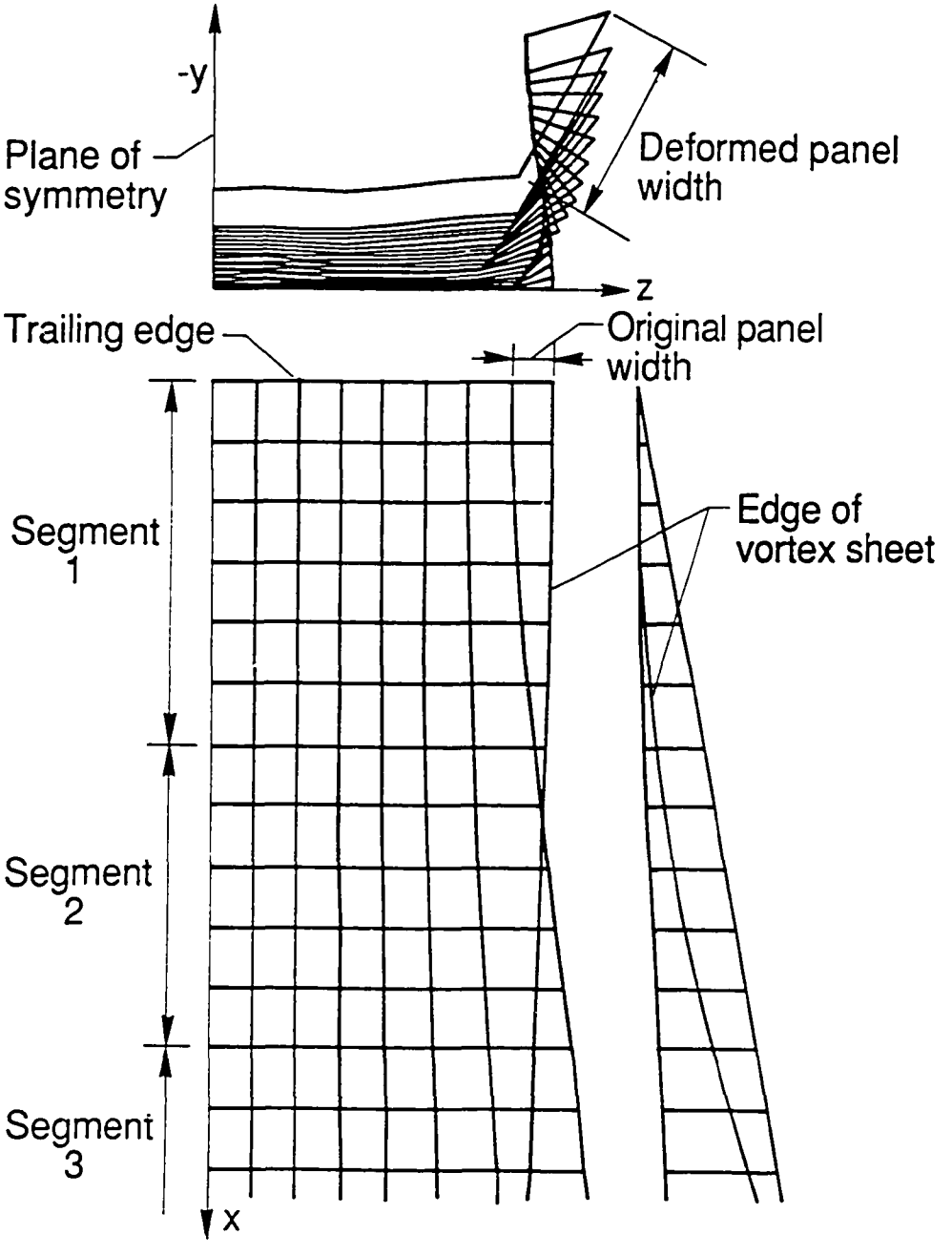

Fig. 13 Converged trailing-edge wake shape after 4 outer- and 5 inner-loop iterations.

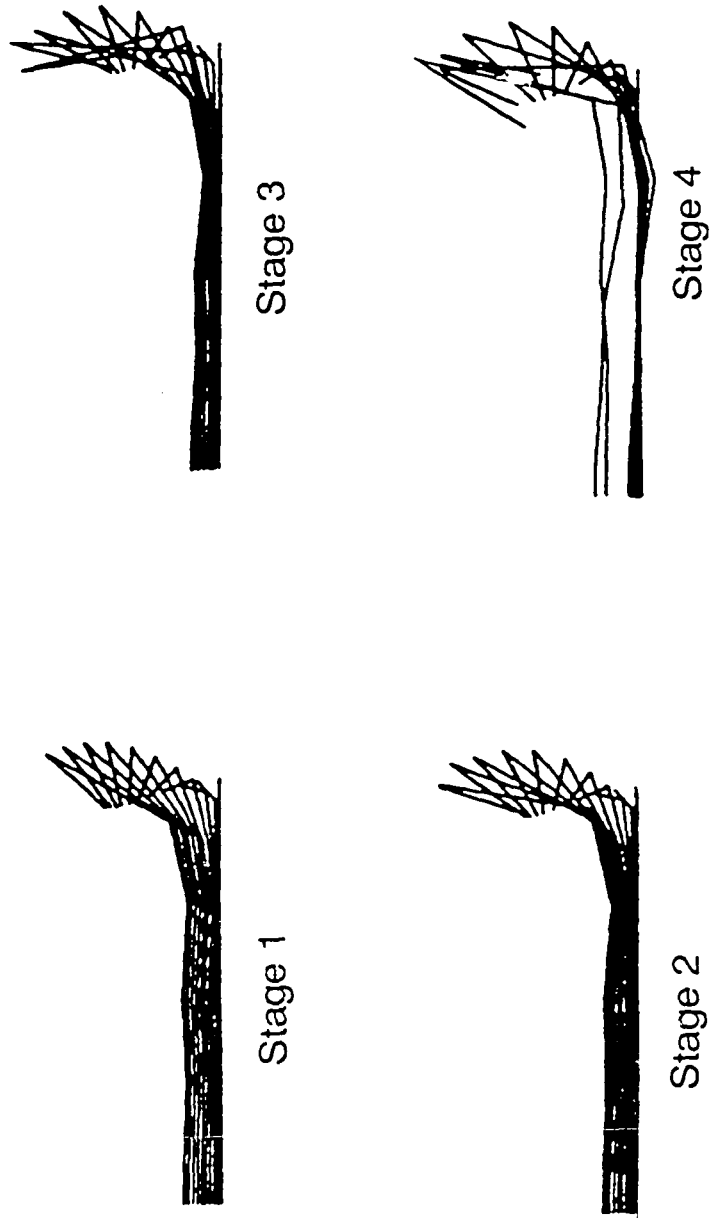

Fig. 14 The instability of wake adjustment near the vortex core region caused by over-stretched panel width.

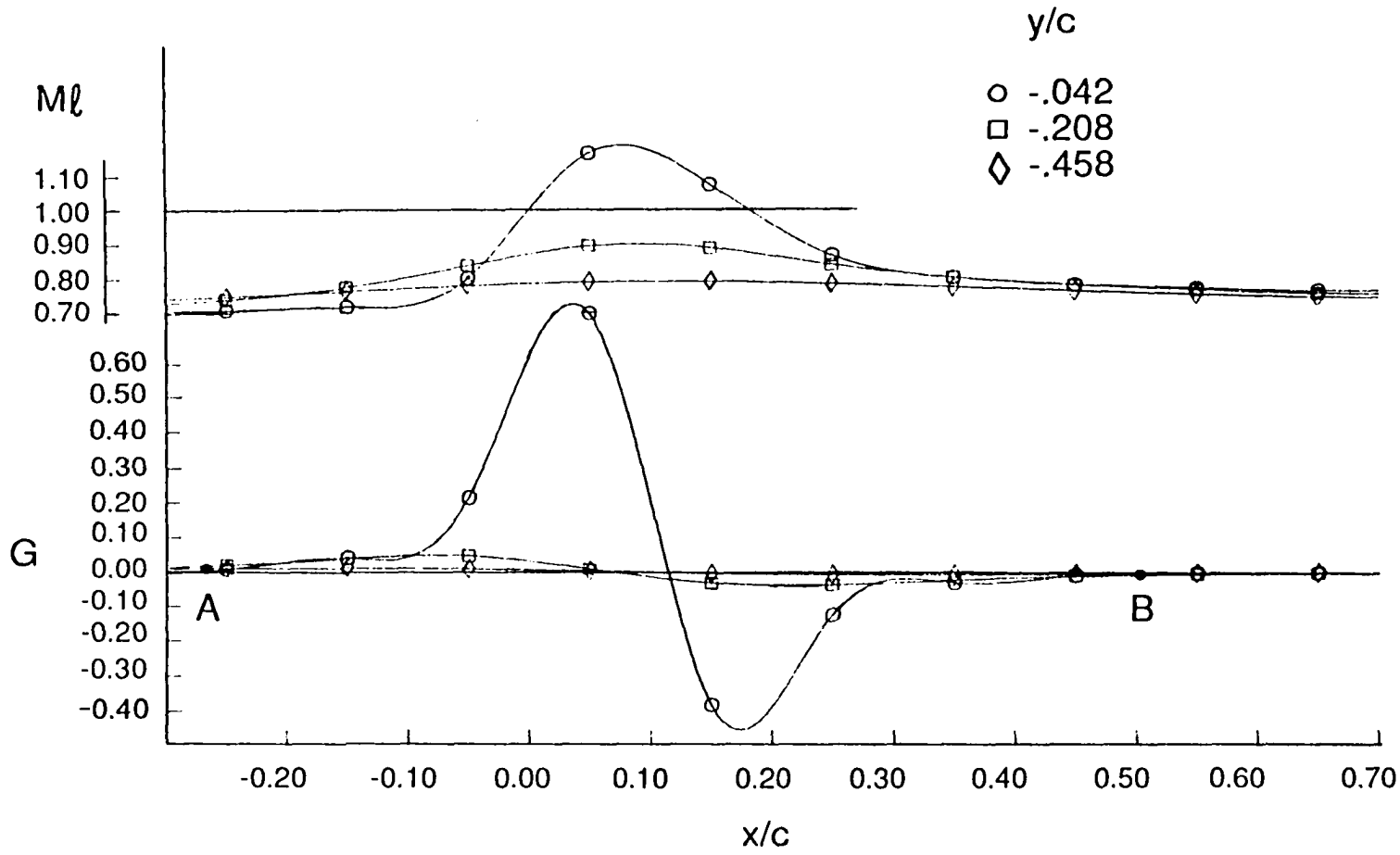

Fig. 15 Chordwise variation of G & local Mach no. for a rectangular wing of AR = 2.0, $M_\infty = 0.7$, $\alpha = 10°$, z/b = 0.083, converged solution at various y/c

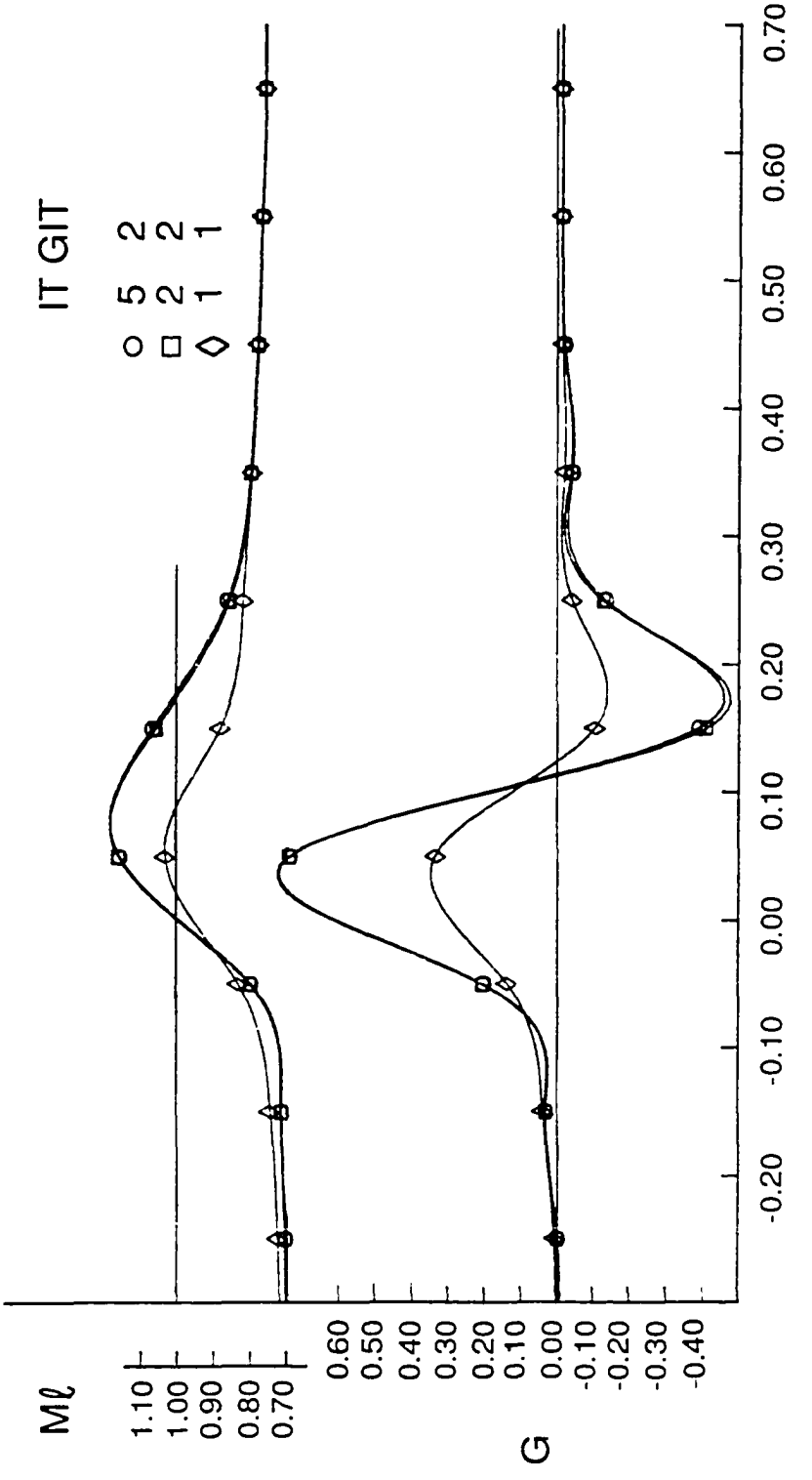

Fig. 16 Chordwise variation of G & local Mach no. for a rectangular wing of AR = 2.0, $M_\infty = 0.7$, $\alpha = 10°$, z/b = 0.083, at different iteration with y/c = -.042

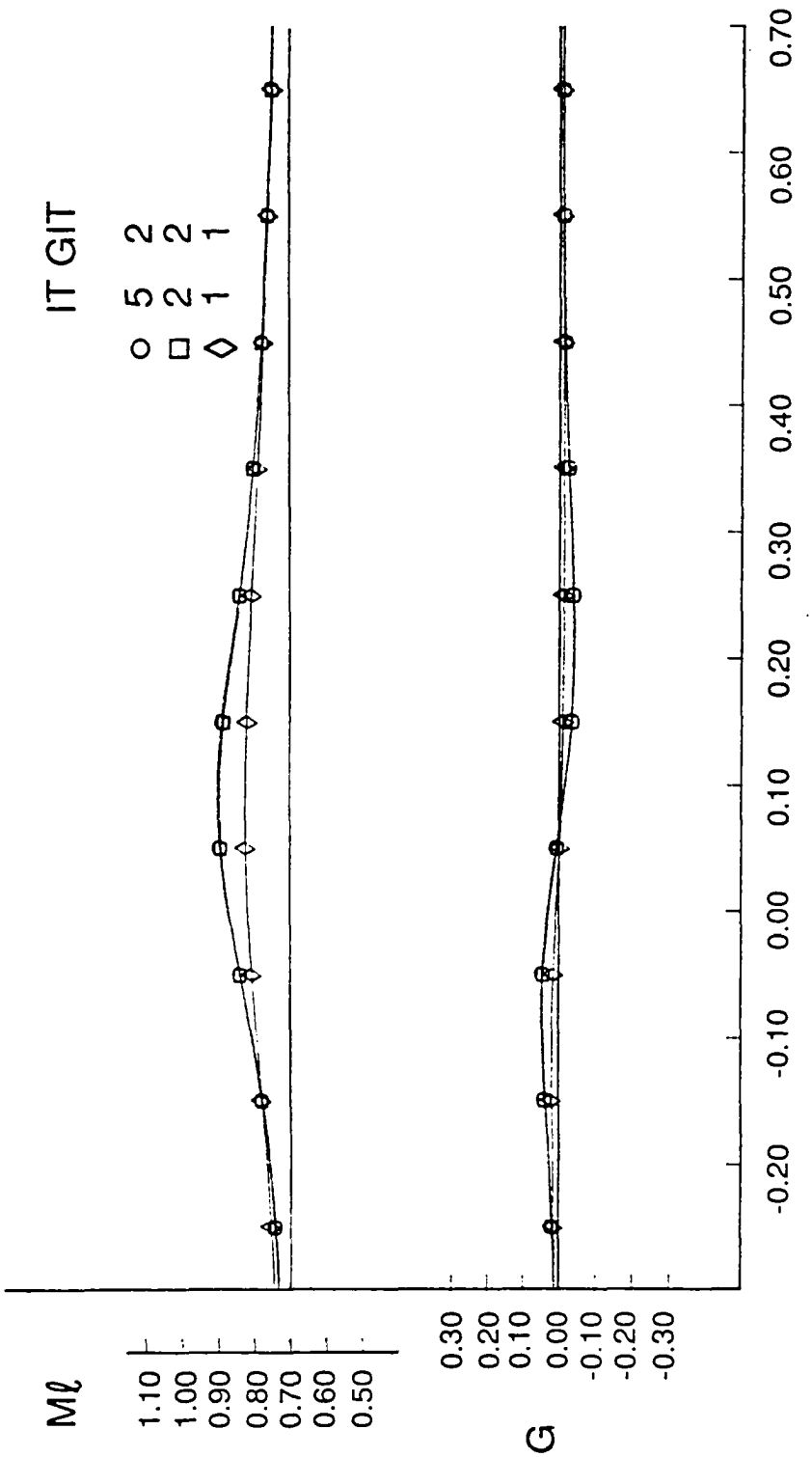

Fig. 17 Chordwise variation of G & local Mach no. for a rectangular wing of AR = 2.0, $M_\infty = 0.7$, $\alpha = 10°$, z/b = 0.083, at different iteration with y/c = -.208

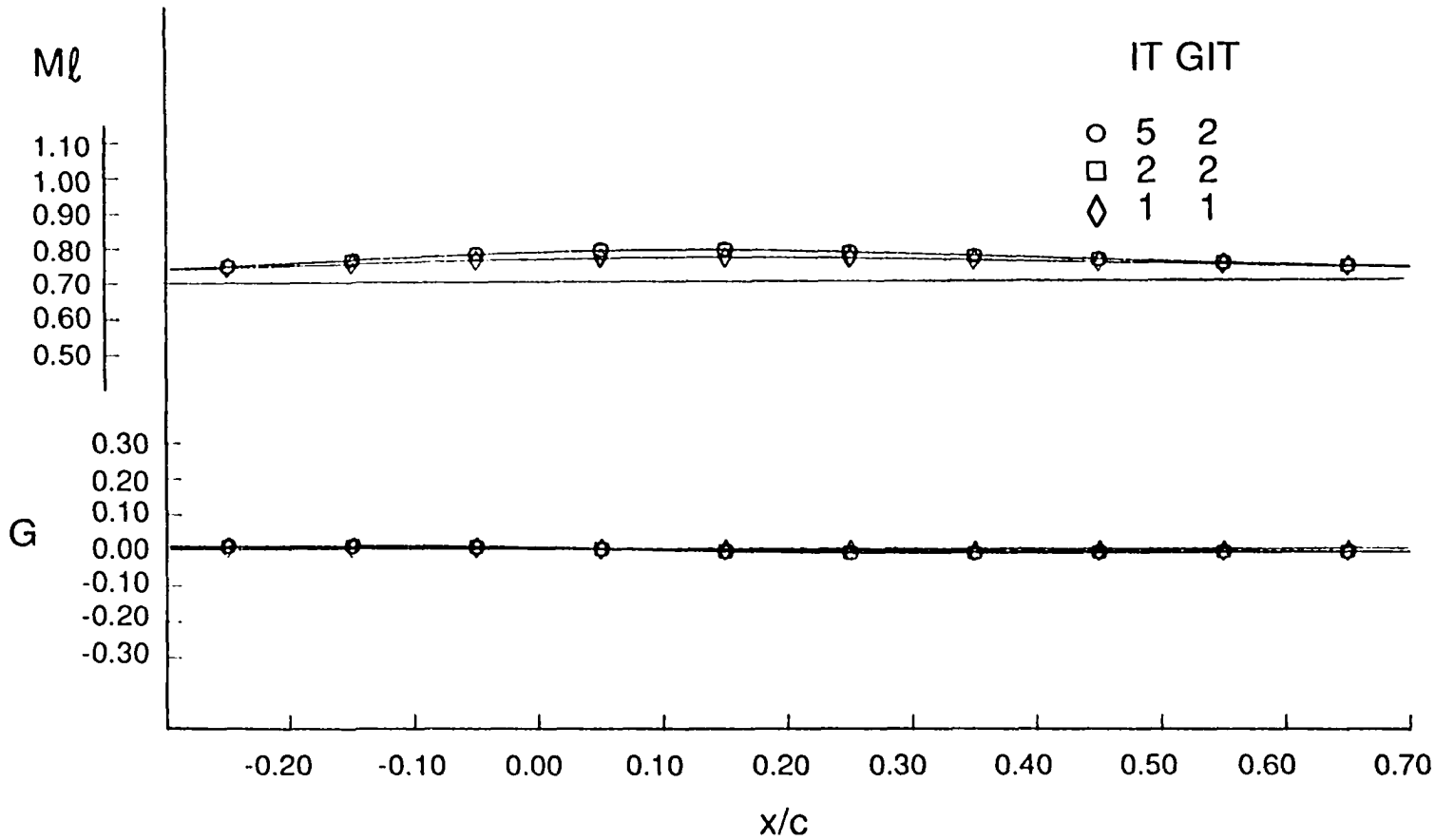

Fig. 18 Chordwise variation of G & local Mach no. for a rectangular wing of AR = 2.0, M_∞ = 0.7, α = 10°, z/b = 0.083, at different iteration with y/c = -.458

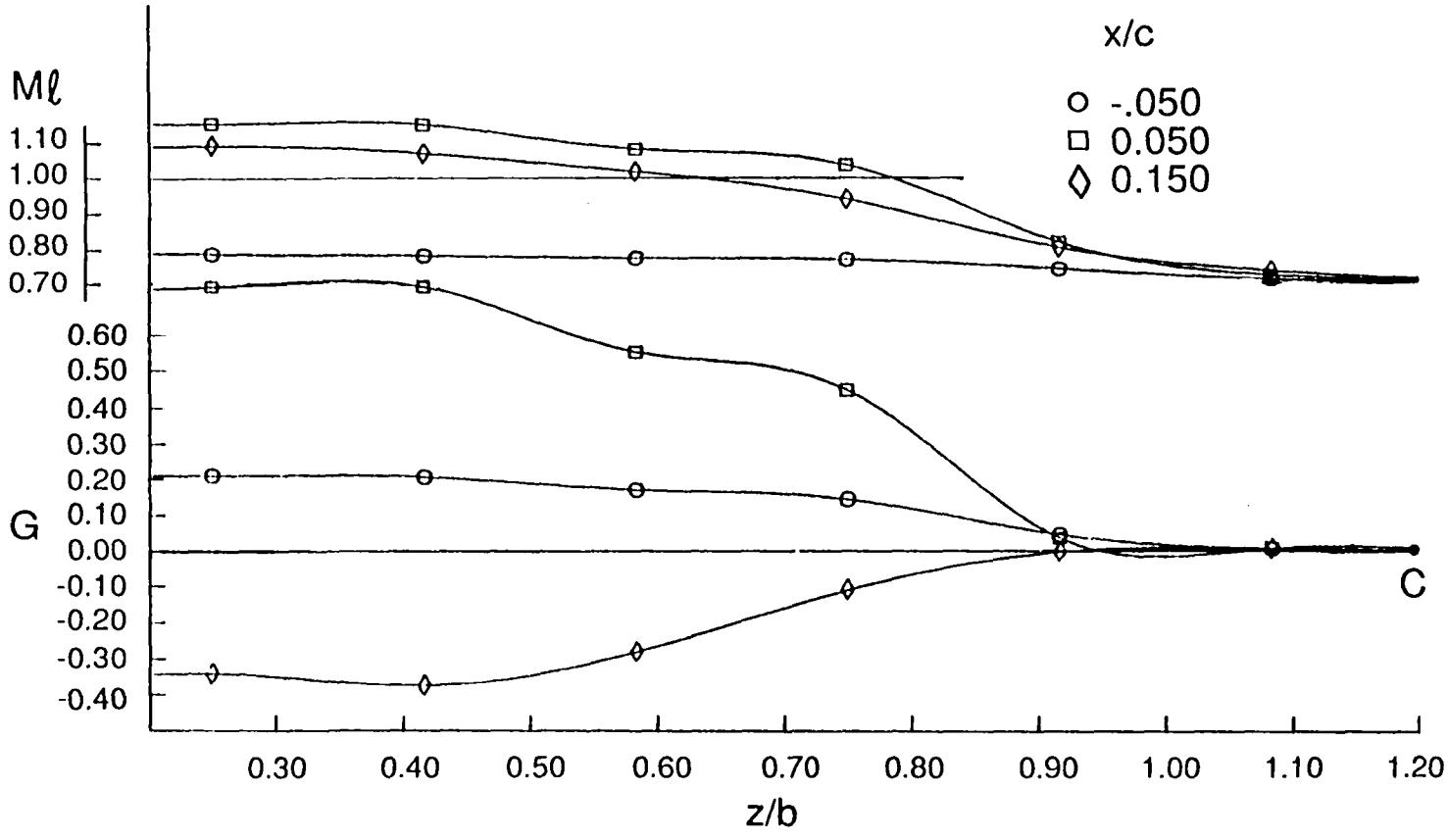

Fig. 19 Spanwise variation og G & local Mach no. for a rectangular wing of AR = 2.0, $M_\infty = 0.7$, $\alpha = 10°$, z/b = 0.083 converged solution at various x/c

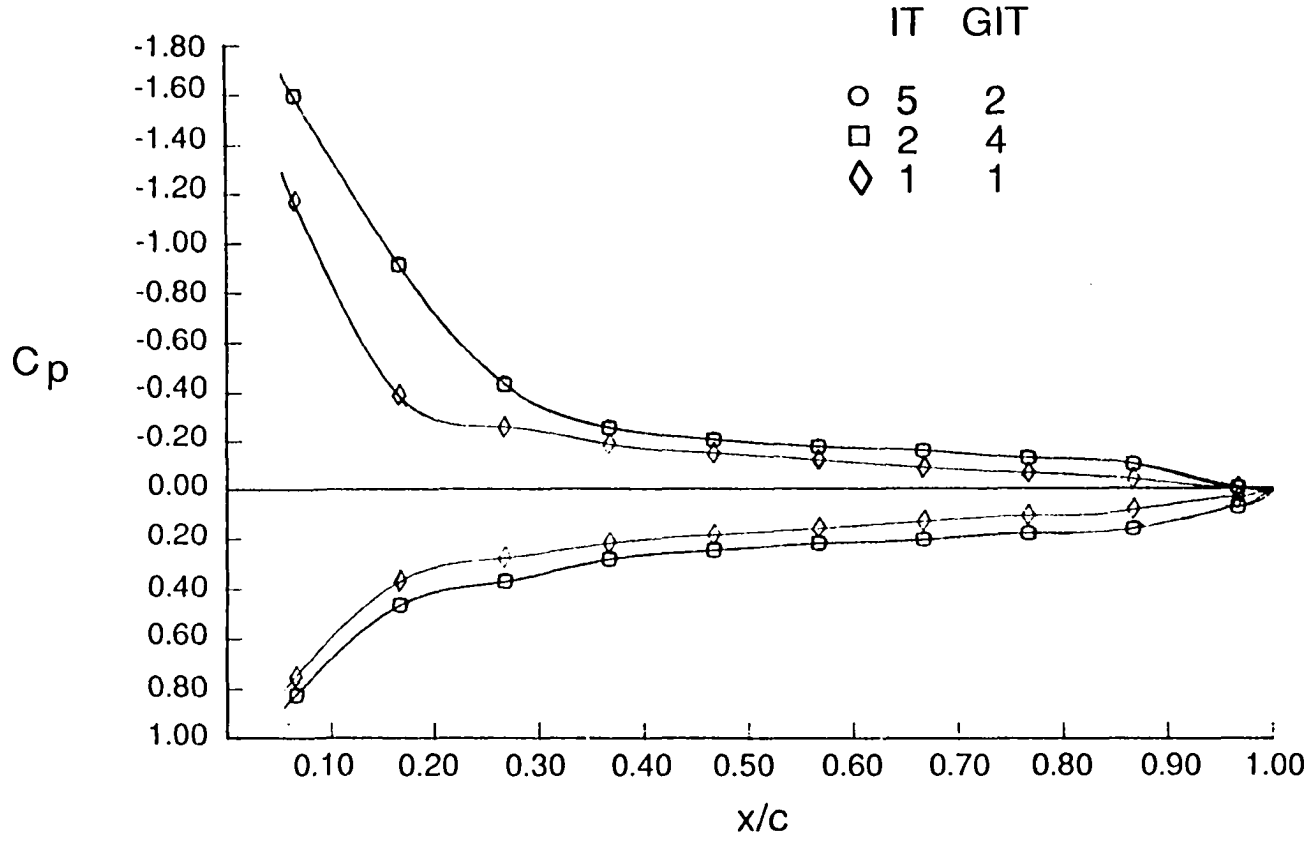

Fig. 20 Chordwise variation of surface pressure coefficient at different iteration for rectangular wing of AR = 2.0, $M_\infty = 0.7$, $\alpha = 10°$, z/b = 0.111

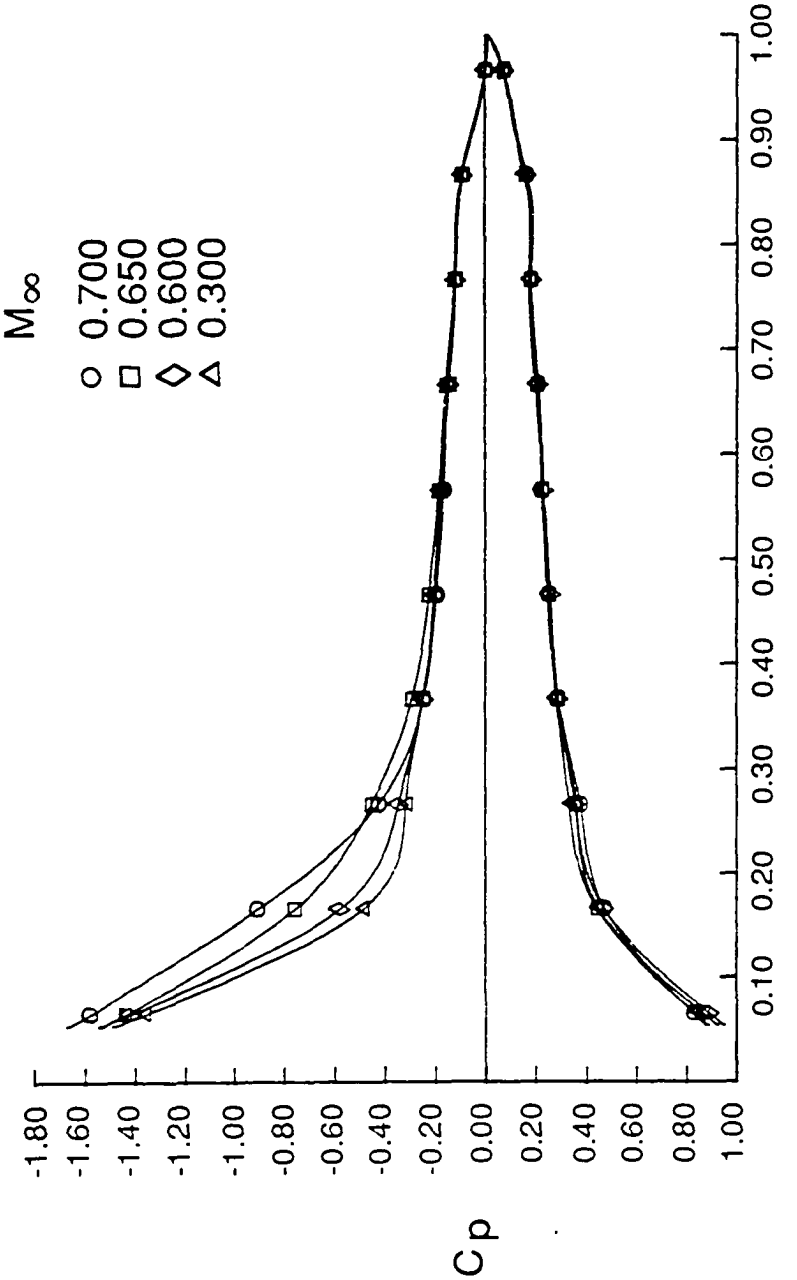

Fig. 21 Chordwise variation of surface pressure coefficient for a rectangular wing of AR = 2.0, $\alpha = 10°$, z/b = 0.111 with various M_∞

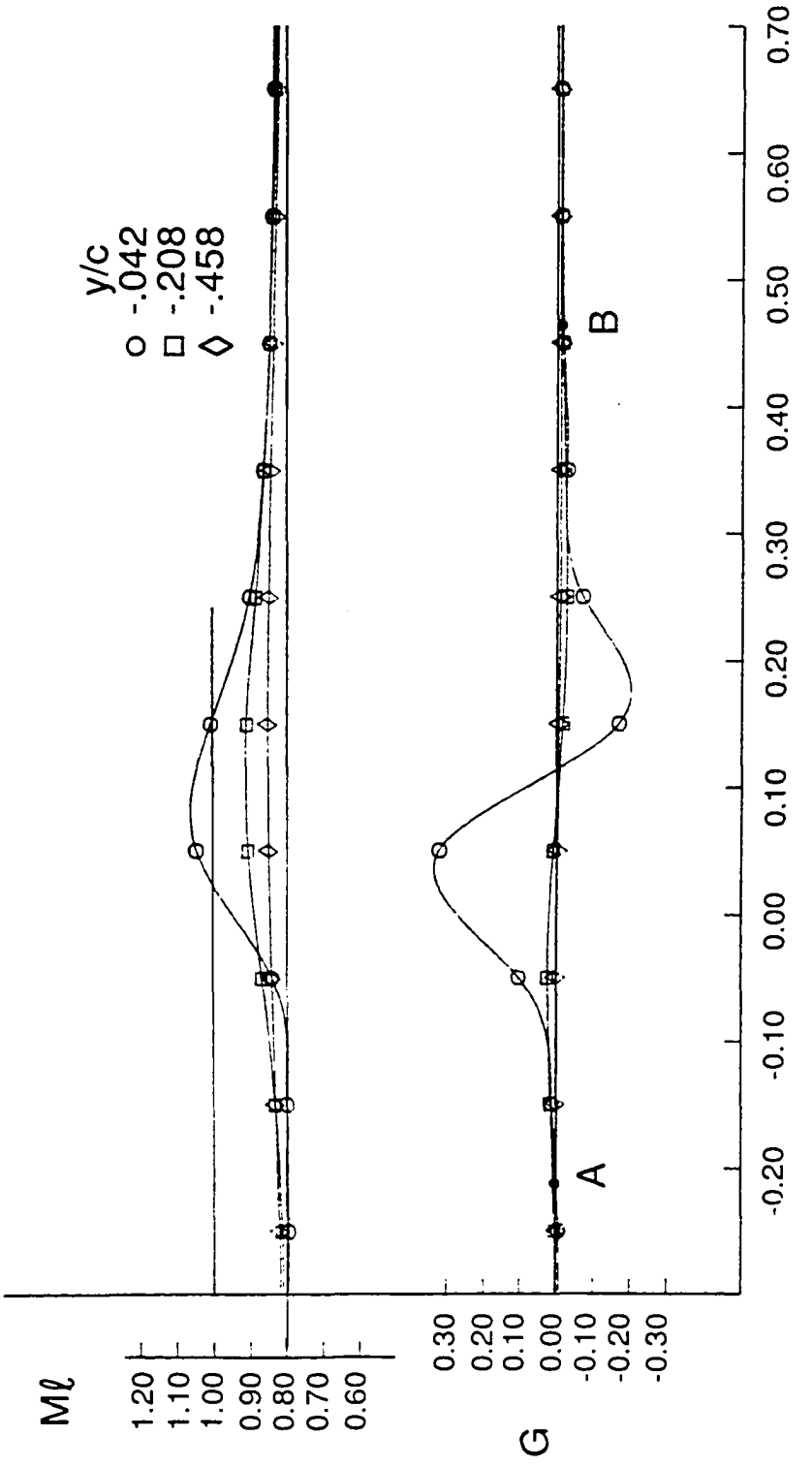

Fig. 22 Chordwise variation of G & local Mach no. for a rectangular wing of AR = 2.0, $M_\infty = 0.8$, $\alpha = 5°$, z/b = 0.083, converged solution at various y/c

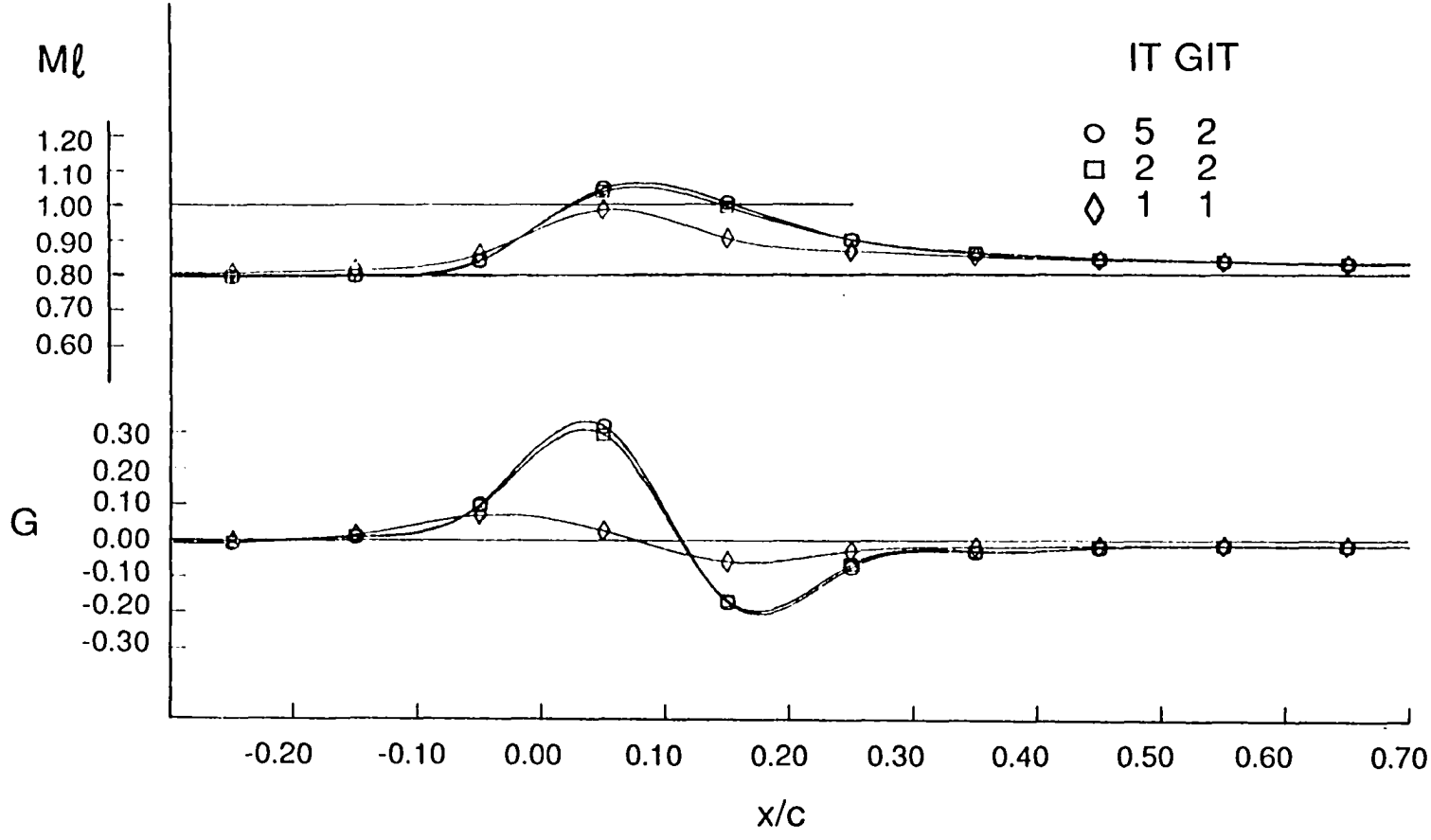

Fig. 23 Chordwise variation of G & local Mach no. for a rectangular wing of AR = 2.0, $M_\infty = 0.8$, $\alpha = 5°$, z/b = 0.083, at different iteration with y/c = -.042

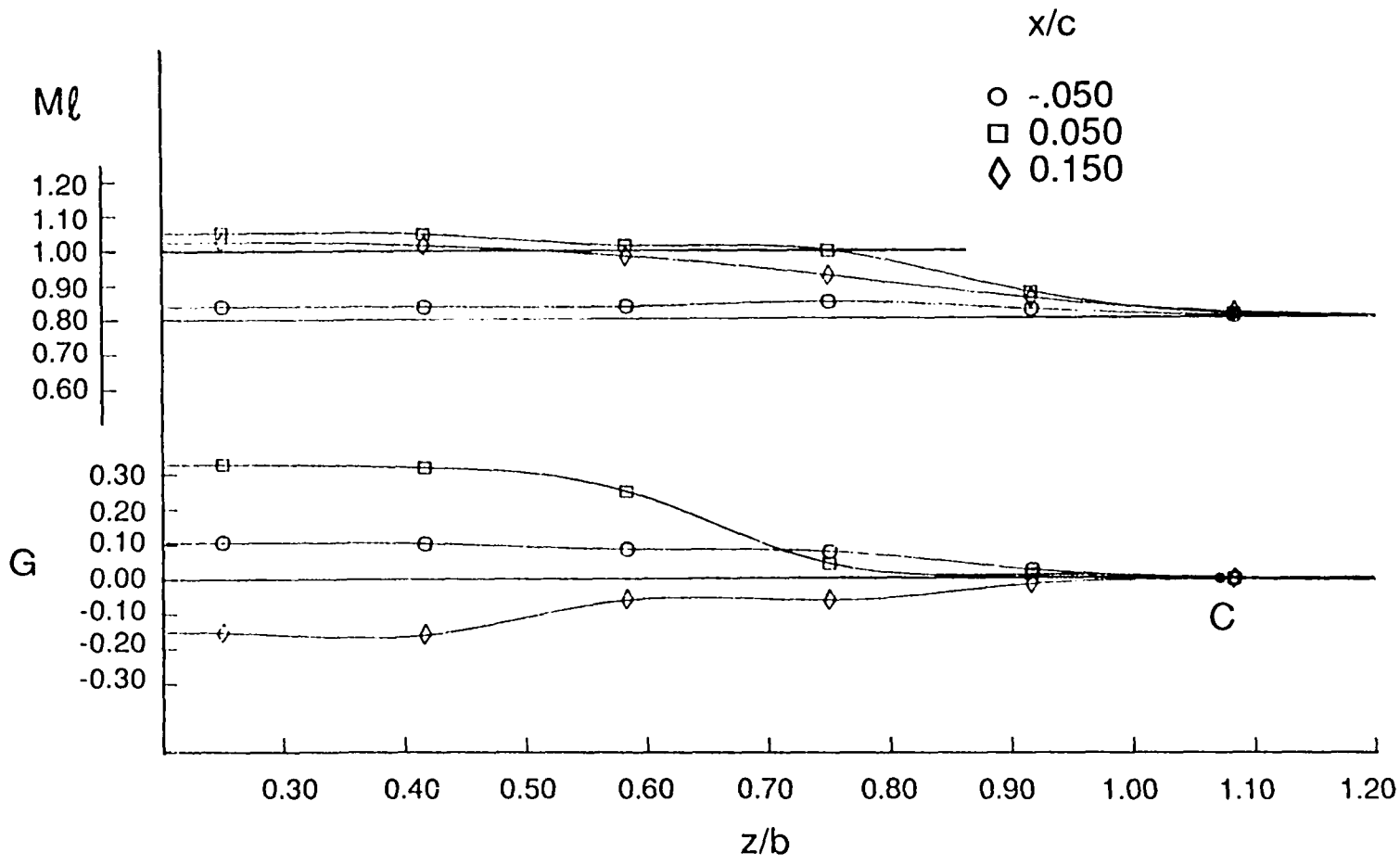

Fig. 24 Spanwise variation of G & local Mach no. for a rectangular wing of AR = 2.0, $M_\infty = 0.8$, $\alpha = 5°$, y/c = -.0.042, converged solution at various x/c

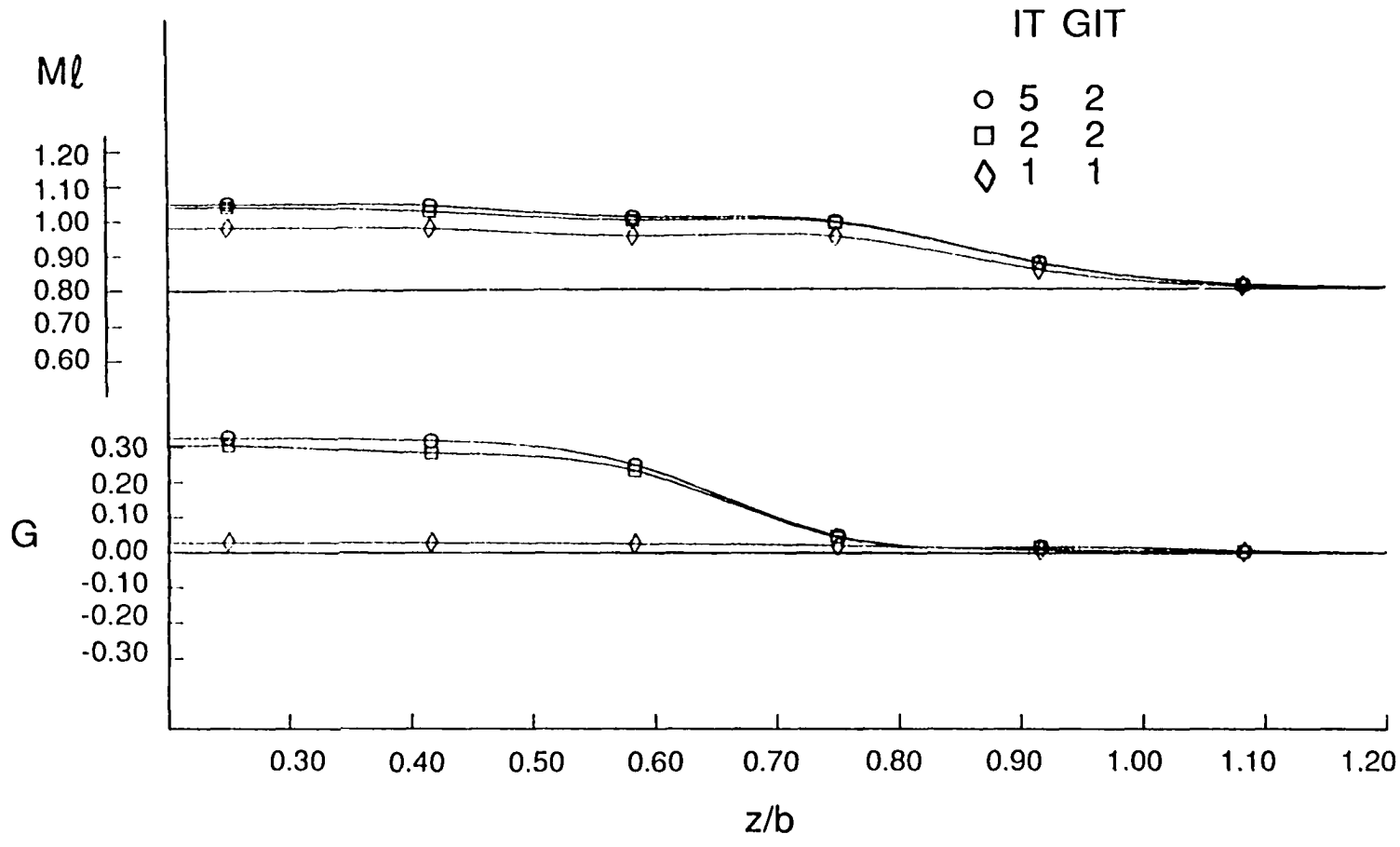

Fig. 25 Spanwise variation of G & local Mach no. for a rectangular wing of AR = 2.0, $M_\infty = 0.8$, $\alpha = 5°$, y/c = -.042, at different iteration with x/c = 0.05

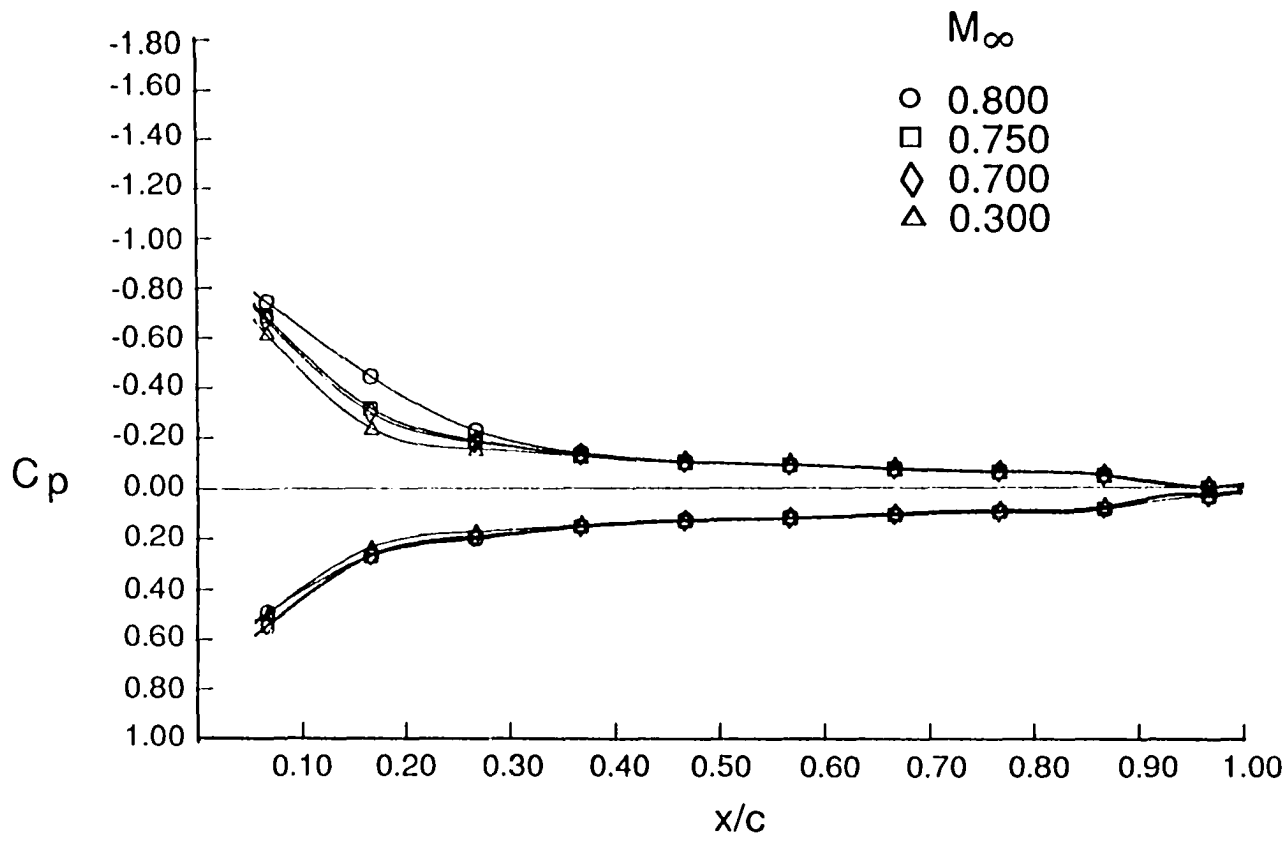

Fig. 26 Chordwise variation of surface pressure coefficient for a rectangular wing of AR = 2.0, $\alpha = 5°$, z/b = 0.111 with various M_∞

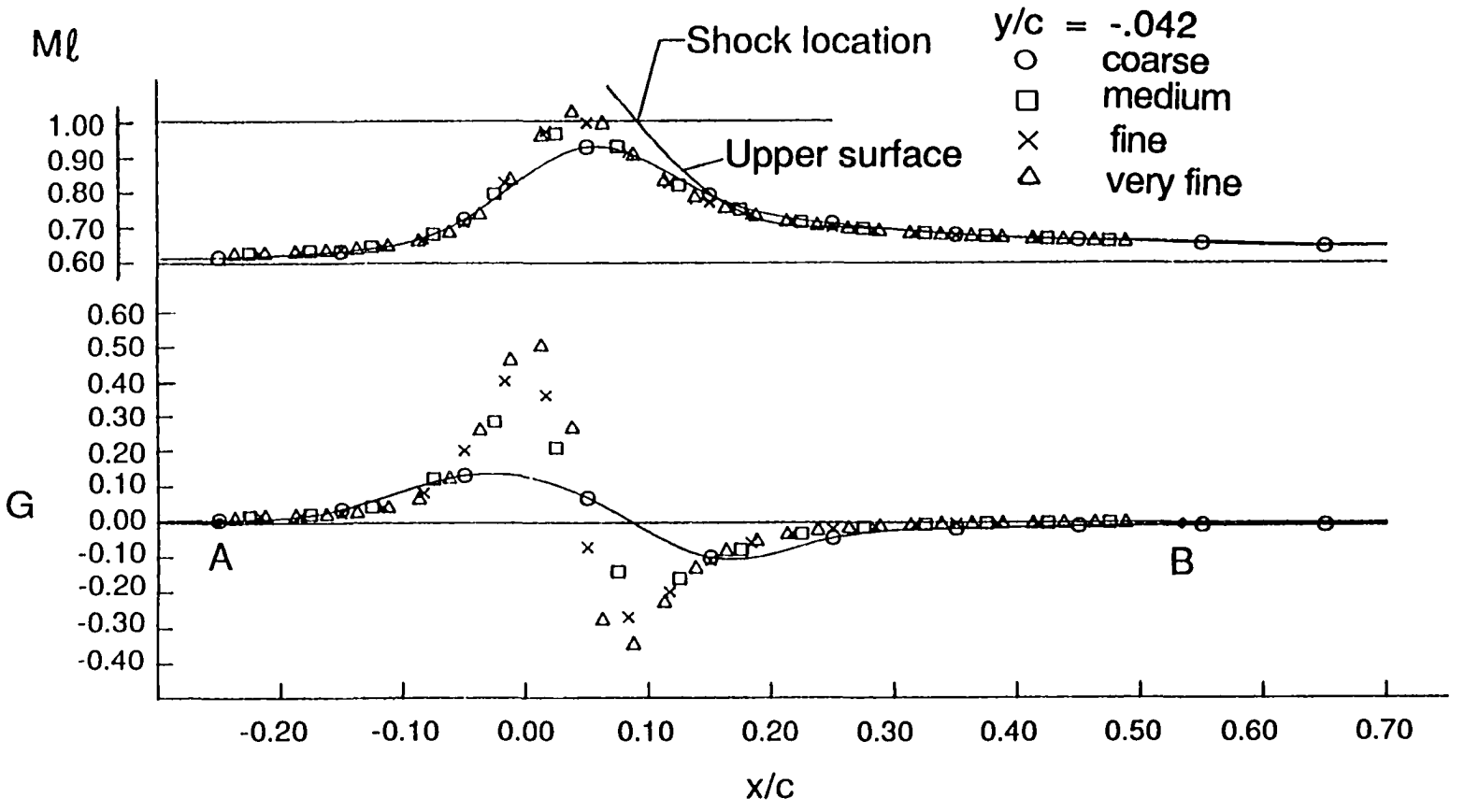

Fig. 27 Comparison among the solutions of various grid sizes in chordwise variation of G & local Mach no. for a rectangular wing of AR = 2.0, M_∞= 0.6 α = 10°, z/b = 0.083

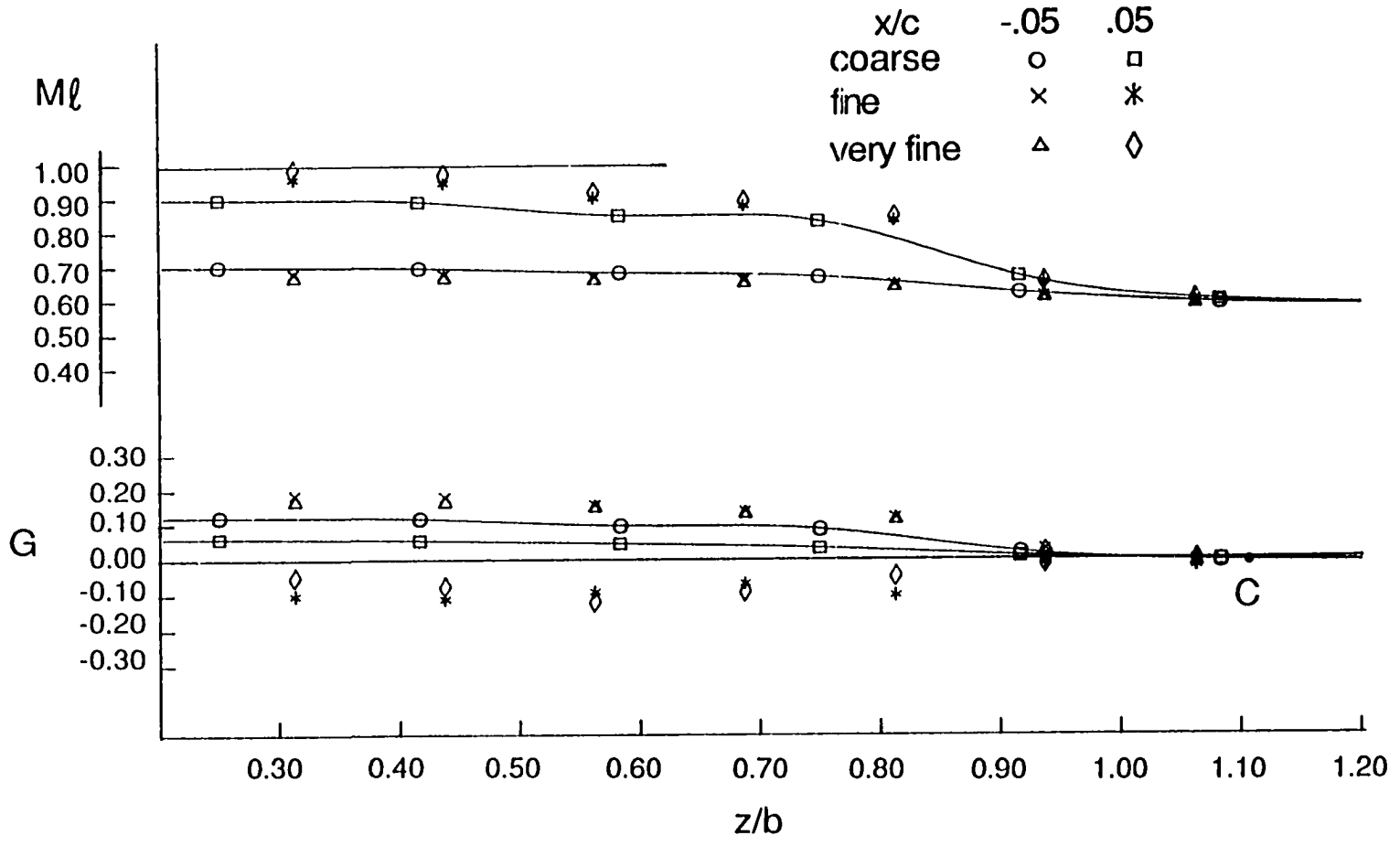

Fig. 28 Comparison among the solutions of various grid sizes in spanwise variation of G & local Mach no. for a rectangular wing of AR = 2.0, M_∞= 0.8, α =5°, y/c = -.042, at different iteration with x/c = 0.05

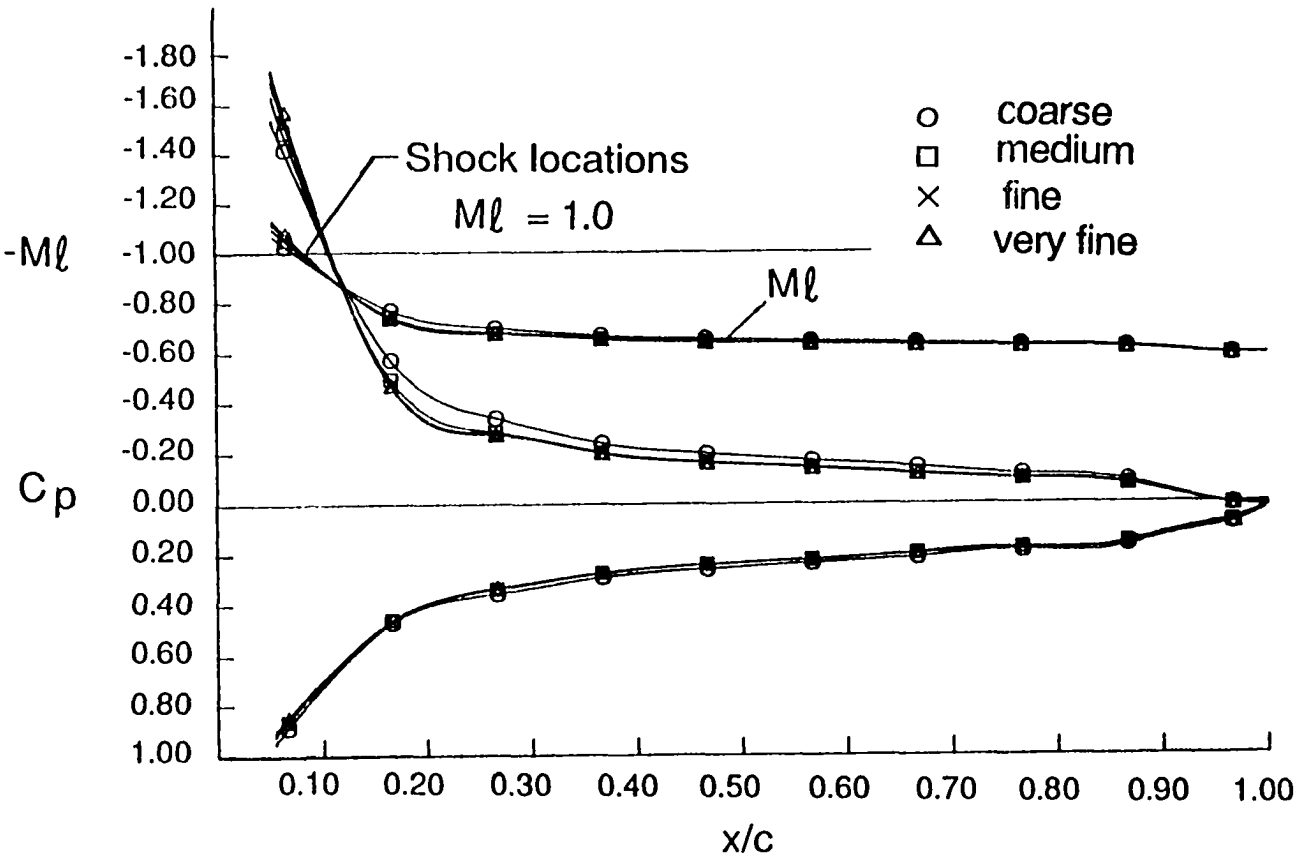

Fig. 29 Comparison among the solutions of various grid sizes in chordwise variation of surface pressure coefficient for a rectangular wing of AR = 2.0, $M_\infty = 0.6$, $\alpha = 10°$